Titre: Title:	Selectively Absorbing Plasmonic Metal-Island Films
Auteur: Author:	Antonin Riera
Date:	2019
Type:	Mémoire ou thèse / Dissertation or Thesis
Référence: Citation:	Riera, A. (2019). Selectively Absorbing Plasmonic Metal-Island Films [Master's thesis, Polytechnique Montréal]. PolyPublie. https://publications.polymtl.ca/4119/

POLYTECHNIQUE MONTRÉAL
affiliée à l'Université de Montréal

Selectively absorbing plasmonic metal-island films

ANTONIN RIERA
Département de génie physique

Mémoire présenté en vue de l'obtention du diplôme de *Maîtrise ès sciences appliquées*
Génie physique

Décembre 2019

POLYTECHNIQUE MONTRÉAL
affiliée à l'Université de Montréal

Ce mémoire intitulé :

Selectively absorbing plasmonic metal-island films

présenté par **Antonin RIERA**
en vue de l'obtention du diplôme de *Maîtrise ès sciences appliquées*
a été dûment accepté par le jury d'examen constitué de :

Michel MEUNIER, président
Ludvik MARTINU, membre et directeur de recherche
Jolanta-Ewa SAPIEHA, membre et codirectrice de recherche
Denis SELETSKIY, membre

DEDICATION

To my parents

ACKNOWLEDGMENTS

I would like to thank my research director, Ludvik Martinu, and co-director, Jolanta Sapieha, who provided me a place at the Functional Coating and Surface Engineering Laboratory (FCSEL) as undergraduate and graduate student. The years I had the privilege to spend at the FCSEL granted me the opportunity to further my knowledge in thin film and solid state physics under your supervision.

To Bill Baloukas and Oleg Zabeida who have provided an invaluable help, supporting me throughout my work at the lab and sharing their experience.

A big thanks to the technicians: Mikaël Leduc and Francis Turcot who greatly helped me to realize my experiments, thanks to their knowledge and craftsmanship.

Lastly, everyone at the lab; Francis, Erika, Jacques, Josefina, Louis, Phillip, Rodrigue, Sasha, and all of those with whom I've shared ideas, discussions and moments. Thank you, as you've made this experience truly positive and inspiring.

RÉSUMÉ

La perception de la couleur est un attribut fondamental de la vision humaine. Au quotidien, cela nous permet de rapidement reconnaître de la nature de nombreux matériaux et même d'attirer l'attention. La couleur d'un objet peut être modifiée en utilisant un revêtement contenant des pigments ou des colorants de la couleur souhaitée, qui préservent la morphologie et la composition de l'objet. La modification de la composition pour induire une coloration est très courante pour les plastiques et les verres. Cependant, le triage et la réutilisation des différents pigments est difficile voire impossible. Une alternative à l'utilisation de pigments ou de colorants, consiste à utiliser une coloration structurelle obtenue en modifiant la structure de la surface d'un matériau. Contrairement à la nature absorbante des colorants et des pigments, les couleurs structurelles sont généralement générées par diffraction et interférence. Cependant, la sensibilité angulaire peut être indésirable pour certaines applications.

La couleur structurelle à base de matériaux plasmoniques suscite beaucoup d'intérêt pour remplacer le contrôle de la couleur d'un objet grâce à leur forte absorption due à l'excitation de plasmon de surface localisé (LSP). Ce phénomène est attribué à la présence d'électrons libres qui, lorsque exposé à un champ électromagnétique (EM), *i.e.* la lumière, peuvent osciller de manière cohérente. Jusqu'à présent, l'or et l'argent ont été au centre de la plupart des études sur le sujet, car ils présentent un fort pic d'absorption dans le visible. De plus, ils ont l'avantage de former des îlots isolés lors de leur croissance, supportant ainsi une résonance localisée du plasmon de surface (LSPR) aux premières étapes de la croissance avec des techniques de dépôt de type PVD. Malgré des travaux approfondis sur le sujet des nanoparticules (NPs) plasmoniques, leur incorporation à des applications commerciales s'est limité principalement, par exemple, à des capteurs exploitant le champ électromagnétique local renforcé en raison de l'excitation du LSP pour augmenter la sensibilité de la spectroscopie Raman. Cependant, leur utilisation en tant que filtre absorbant pour induire une couleur à des fins esthétiques n'a pas encore été exploitée significativement. Certaines vitres architecturales ont une couleur induite par la présence de NPs de métaux nobles. L'utilisation de ces NPs métalliques pourrait aussi servir à remplacer des revêtements pour lunettes ophtalmiques. Le contrôle de la taille et de la forme des NPs a une incidence sur la fréquence de résonance et le contrôle de la morphologie est difficile avec les méthodes de dépôt industrielles classiques telles que la pulvérisation magnétron et l'évaporation. La réduction chimique de l'or en solution permet la fabrication de différentes formes de NPs avec un contrôle de leur taille, mais le transfert de ces particules sur de grandes surfaces est difficile. Dans le cas présent, l'objectif est de contrôler le pic d'absorption mais aussi de disposer d'une bande d'absorption

étroite dans le visible en utilisant la pulvérisation cathodique par magnétron en tant que technique de dépôt qui permet le revêtement de grandes surfaces et est largement utilisée pour la croissance de couches minces dans l'industrie.

En raison des nombreux paramètres affectant la croissance des îlots sur une surface, l'or a été sélectionné en raison de son inertie chimique, ce qui simplifie sa caractérisation *ex-situ*. Un système optique fait maison a été fabriqué pour étudier l'évolution des propriétés optiques du film pendant le dépôt afin d'obtenir des informations sur l'évolution de la morphologie des îlots. En effet, ce système a permis de suivre différentes phases de croissance tout au long du dépôt, corroborées par une imagerie fait par microscopie électronique. Le comportement optique est alors analysé et expliqué à l'aide de travaux antérieurs trouvés dans la littérature.

De plus, la mobilité de surface des adatomes est grandement limitée à température ambiante et ces travaux mettent en évidence la limite de la technique de dépôt pour les applications visées. En effet, pour générer une absorption plus forte, il faut déposer davantage de matériau, mais une limite est atteinte lorsque les îles commencent à s'allonger, ce qui entraîne un élargissement de la distribution de taille et, du même coup, l'élargissement du pic d'absorption. L'augmentation de la température de surface permet aux l'îlots de se remodeler et de rester sphéroïdiques, ce qui leur permet de s'élargir sans se toucher, entraînant leur changement de forme. Cependant, l'augmentation de la température de surface n'est pas compatible avec tous les substrats. Certains, comme le plastique, ne résistent pas à des températures beaucoup plus élevées que 100°C. C'est pourquoi l'application d'une tension sur le porte échantillon lors du dépôt a été étudiée avec l'objectif de favoriser la mobilité de l'or à la surface.

ABSTRACT

The perception of color is a fundamental attribute to human vision. During our daily-life it serves us to better understand our environment as we can recognize many different materials and textures due to their color and appearance. An object's color can be altered by utilizing coatings containing pigments or dyes of the desired color which preserve the object's morphology and composition. This modification of the composition to induce a coloration is very common for plastics and glasses but the removal of the different pigments is difficult at the product's end of life. An alternative to the use of pigments or dyes, which can have poor resistance to photobleaching and pose problems for recycling, is the use of structural coloring which is achieved by modifying the surface structure of a material. Contrary to the absorption nature of dyes and pigments, structural colors are generally generated through diffraction and interference. However, their inherent angular color variation (iridescence) can be unwanted in some applications.

Plasmonic-based structural color is emerging as a substitute to control an object's color through absorption due to the excitation of localized surface plasmons (LSPs) when confined free electrons are exposed to an electromagnetic (EM) field, *i.e.*, light. So far, gold and silver have been the center of much of the studies on the subject as they display a strong absorption peak in the visible and generally naturally form isolated islands in their early growth stages, supporting a localized surface plasmon resonance (LSPR).

Despite extensive work on the subject of plasmonic nanoparticles (NPs), their incorporation into commercial applications are mostly limited to sensors exploiting the EM field enhancement procured by LSP excitation to increase Raman spectroscopy sensitivity for example. This study aims at evaluating their use as absorbing filters to induce color for aesthetic purposes.

The size and shape controls of the NPs affect the resonance frequency and the morphology control is difficult with conventional industrial deposition methods such as magnetron sputtering and evaporation. The chemical reduction of gold in solution allows the manufacturing of various NPs shapes with control on their size but the transfer of these particles onto large surfaces is challenging. In the present case, the aim is to control the absorption peak but also to have a narrow absorption band in the visible using magnetron sputtering as a deposition technique as it allows the coating of large surfaces and is widely employed in the thin-film industry.

Due to the many parameters affecting the growth of islands on a surface, gold was selected

due to its chemical inertness which simplifies its *ex-situ* characterization. An in-house optical system was made to investigate the evolution of the optical properties of the film during deposition to obtain information about the evolution of the morphology of the film. This system allowed the tracking of different growth stages throughout deposition, corroborated with electron microscopy imaging. The optical behavior is explained with the help of previous work found in the literature.

Furthermore, this work has highlighted the limitations of the deposition technique at room temperature, at which the surface mobility of the adatoms is limited. To generate a stronger absorption, more material is needed but there's a limit attained when the islands start to become elongated causing the absorption peak to broaden. Increasing the surface temperature allows the island to reshape and remain spheroidal, allowing the deposition of more material. However, increasing the surface temperature is not compatible with every substrate. For instance, plastic substrates typically do not resist at temperatures much higher than $100°C$. It's thus why the application of a bias during deposition has been explored in order to promote the surface mobility of the gold atoms.

TABLE OF CONTENTS

DEDICATION iii

ACKNOWLEDGMENTS iv

RÉSUMÉ v

ABSTRACT vii

TABLE OF CONTENTS ix

LIST OF TABLES xii

LIST OF FIGURES xiii

LIST OF SYMBOLS AND ABBREVIATIONS xx

LIST OF APPENDICES xxv

CHAPTER 1 INTRODUCTION 1
1.1 Plasmonic color 1
1.2 Applications 2
1.3 Research context 3
1.4 Scientific contribution 5
1.5 Thesis outline 6

CHAPTER 2 LITERATURE REVIEW AND THEORY 7
2.1 Foreword 7
2.2 Physical vapor deposition 7
2.2.1 Thin gold film deposition by evaporation 8
2.2.2 DC diode sputtering 8
2.2.3 RF diode sputtering 9
2.2.4 Magnetron sputtering 10
2.2.5 Reactive sputtering 10
2.2.6 Sputtering over evaporation 11
2.3 Growth of island films 12
2.3.1 Growth modes of thin films 12

2.3.2 Growth kinetics . . . 13
2.3.3 Surface diffusion . . . 15
2.3.4 Coalescence process . . . 17
2.3.5 Thermal anneal and substrate's surface temperature . . . 20
2.3.6 Growth regimes . . . 21
2.3.7 Ion bombardment on metal-island films . . . 23
2.4 Plasmonic . . . 25
2.4.1 Lorentz model . . . 26
2.4.2 Drude-Lorentz model . . . 28
2.4.3 Effective medium approximation . . . 29
2.4.4 Localized Surface Plasmon . . . 31
2.4.5 Spherical nanoparticles . . . 32
2.4.6 Plasmonic materials . . . 34
2.4.7 Evolution of the optical properties of metal-island films . . . 35

CHAPTER 3 EXPERIMENTAL METHODOLOGY . . . 38
3.1 Experimental apparatus . . . 38
3.1.1 Deposition chamber . . . 38
3.1.2 Deposition conditions . . . 39
3.2 Optical characterization . . . 40
3.2.1 Ellipsometry . . . 40
3.2.2 Spectrophotometry . . . 41
3.2.3 Colorimetry . . . 41
3.2.4 Differential spectrometry . . . 44
3.2.5 Reflection and transmission coefficients . . . 47
3.3 Surface imaging . . . 48
3.3.1 Electron microscopy . . . 48
3.3.2 Image analysis . . . 49

CHAPTER 4 RESULTS AND DISCUSSION . . . 52
4.1 Effect of the seed layer and encapsulating material . . . 52
4.2 Durability . . . 54
4.3 Gold film optical monitoring and effect of ion bombardment during growth . . . 57
4.3.1 Color evolution during gold film growth . . . 57
4.3.2 Gold-island film morphology and color evolution . . . 61
4.3.3 Post-deposition ion bombardment . . . 65
4.3.4 Ion bombardment and deposition on Orma . . . 66

CHAPTER 5 REFLECTIVITY MONITORING OF GOLD FILMS 68
5.1 Motivations 68
5.2 Evolution of the reflectivity 69
5.2.1 Impact of the temperature 70
5.2.2 Reflectivity evolution trends 71
5.3 TEM observations 72
5.3.1 Room temperature 73
5.3.2 High temperatures 76
5.4 Time derivative surface reflectance 79
5.4.1 Room temperature 79
5.4.2 High temperatures 83
5.5 Modeling 85
5.6 General considerations 86

CHAPTER 6 GENERAL DISCUSSION, CONCLUSIONS AND PERSPECTIVE . 88
6.1 Foreword 88
6.2 General discussion and conclusions 88
6.3 Perspectives and outlook 89

REFERENCES 90

ANNEXES 103

LIST OF TABLES

Table 1.1 OIC proceeding paper reference. 5

LIST OF FIGURES

Figure 1.1 The famous Lycurgus cup illuminated from behind. Light absorption by the gold nanoparticles generates a red (transmitted) color whereas the scattered light yields a green (reflected) color. Adapted with permission from Novotny *et al.* [9]. 2

Figure 1.2 Structure of a modern ophthalmic lens showing the thin film stack architecture to provide high transmissivity and good mechanical durability. Adapted with permission from D. Meslin [21]. 3

Figure 2.1 Evolution of the island density for sputtered (S) and evaporated (E) Ag/mica films at 25°C and 250°C [40]. 11

Figure 2.2 The three main growth modes are schematically represented here: (a) layer-by-layer (Frank-van der Merve), (b) layer plus island growth (Stranski-Krastanov) and (c) island growth (Vollmer-Weber) with θ the coverage in monolayer (ML). Taken with permission from Venables *et al.* [46]. 13

Figure 2.3 The atomistic processes and energies associated with nucleation and growth on surfaces. Taken with permission from Venables and Spiller [47]. 14

Figure 2.4 (a) Calculated adatom concentration n_1 and (b) stable cluster concentration n_x for an atom flux rate $R = 1.4 \cdot 10^{15}\ cm^{-2}s^{-1}$ of gold on NaCl at various surface temperatures. Taken with permission from Reichelt *et al.* [49] 15

Figure 2.5 Side view of ZnO surface with a Cu island with a simplified energetic diagram highlighting the energy difference of diffusion barriers a Cu atom will encounter while diffusing. From Campbell *et al.* [50]. 16

Figure 2.6 Gold deposition on TiO_2 shows a transition from 2D to 3D growth at a critical coverage θ_{cr}. The surface defects were induced by a thermal anneal at 900 K in O^2 atmosphere with the sputter-induced defects sample having an additional surface treatment of 1 keV Ar^+ plasma etch. Taken with permission from Parker *et al.* [51]. 17

Figure 2.7 Calculated surface energy of two metal islands coalescing with a grain boundary separating them as a function of the radius of the bigger island (right). Taken with permission from Duxbury *et al.* [56] 18

Figure 2.8 5 nm gold island film absorption maxima (a) position and (b) FWHM depending on the annealing temperature for 180 s treatment. Insert: optical images of the color associated with the spectra. Adapted with permission from Sun *et al.* [66]. 20

Figure 2.9 Illustration of the four growth regimes: nucleation and growth of isolated spherical islands (I), partial coalescence of hemispherical clusters (II), coarsening of branched domains of flat spheroids (III), and continuous layer growth after percolation (IV). The image taken with permission from Schwartzkopf *et al.* [72]. 22

Figure 2.10 Ellipsometric angles Δ and Ψ during (a) deposition of gold film and (b) subsequent etching of the gold layer with 100 eV Ar^+ ion beam. Taken with permission from Netterfield *et al.* [83]. 25

Figure 2.11 The magnitude of displacement and phase were obtained with the numerical application of the following values: $N_e = 10^{28}$ cm^{-3}, $\omega_p = 1.3 \times 10^{16}$ rad/s, $\omega_0 = 6.077 \times 10^{15}$ rad/s and $\zeta = 1.519 \times 10^{15}$ rad/s. Taken with permission from Almog *et al.* [85]. 28

Figure 2.12 Two effective medium approximation models : (a) Bruggeman model which calculates the effective dielectric function of a random mixture of two materials, and (b) the Maxwell-Garnett model valid for small inclusions in a matrix. Taken with permission from Mandal *et al.* [95]. 31

Figure 2.13 The schematic depicts (a) the case of a SPP propagating along a dielectric/metal interface with the decaying electric field in the metal away from the interface and (b) oscillations of the electronic cloud inside metal nanoparticles excited by an electric field. Taken with permission from F. Todescato [10]. 32

Figure 2.14 Wavelength where the absorption is maximum for the three coinage metals (Ag, Au and Cu) depending on the matrix dielectric constant n_m which redshifts for increasing n_m. Adapted with permission from J.M. Lamarre [102]. 33

Figure 2.15 Tabulated values of the various quality factors associated with different plasmonic candidate materials. The $Q_{LSPR} = -\varepsilon'(\omega)/\varepsilon''(\omega)$ differs from the $Q_{SPP} = \varepsilon_m'^2(\omega)/\varepsilon_m''(\omega)$ due to the possibility to tune the resonance of the LSPR peak with the geometry of the nanoparticle with ε_m the permittivity of the bulk metal. Adapted with permission from West *et al.* [107]. 35

Figure 2.16 Experimental characterization of NPCs. Taken with permission from Barrow *et al.* [112]. 36
Figure 2.17 Polarized transmission spectra (along the long axis of the NPs) of a 800×400 nm periodic lattice array of nanoparticle pairs. Taken with permission from Atay *et al.* [113]. 37
Figure 3.1 Schematic of the sputtering deposition system used for the deposition of all the samples. 39
Figure 3.2 Schematic of the optical set-up configured for transmission monitoring to obtain color parameters of the gold film *in situ*. 44
Figure 3.3 Schematic of a differential reflectance spectrometry system installed on the deposition system allows one to follow the evolution of reflectance during deposition. 45
Figure 3.4 a) Reflectivity of a dielectric substrate (solid) and the same substrate with about one monolayer of an absorbing film (dashed) and b) the differential reflectivity $\Delta R/R$ caused by the absorbing monolayer film as a function of the angle of incidence of light and its polarization (thickness of the thin film d is very small compared to the wavelength $d/\lambda = 10^{-3}$). Taken from McIntyre and Aspnes [126]. 45
Figure 3.5 Scanning electron micrographs showing the profile of the interaction volume of electrons regarding the working voltage used for (a) 14.86 kV and (b) 29.5 kV beam voltages. Taken from Herzog *et al.* [130]. . 49
Figure 3.6 a) 6 nm effective thickness of gold deposited at 100° C on B270 substrate. b) Intermediate step to improve c) the adaptive threshold accuracy algorithm. Parameters used for the local threshold: kernel size for local mean was 143 (12 × 12) and the offset was 0. 50
Figure 4.1 *Ex situ* absorption measurements of gold films deposited at room temperature with a) different seed layers and b) encapsulating material. Two effective thicknesses of 1.25 nm (red) and 2.5 nm (blue) were deposited on a B270 substrate and the thickness of each dielectric layer was 16 nm. 52
Figure 4.2 Corresponding transmitted colors in sRGB (CIE 1931 2° observers, D65 illuminant) of gold films with different configurations and effective thicknesses. Depositions were done on B270 substrates and the TiO_2 and SiO_2 layer thicknesses was 16 nm. The last two rows of gold films were annealed after deposition. Note: the missing sample detached from the sample holder during deposition and was lost. 53

Figure 4.3 Gold films deposited at room temperature on B270 as-deposited (dashed) and after annealing at 400°C for 1 hr (solid). 54
Figure 4.4 Gold films deposited at room temperature on 20 nm SiO_2 seed layer and capped with another 20 nm silica layer on a borosilicate glass substrate. 55
Figure 4.5 Photography after delamination of the gold films deposited at room temperature on curved Orma substrates with 20 nm SiO_2 seed and capping layer. A fluoro-carbon top coat $\sim$ 5 nm was deposited by thermal evaporation usually used on ophthalmic lenses for its anti-smudge propriety and low coefficient of friction to simulate a typical lens. The film thicknesses are identified in the figures. Note: the 2x2 nm film consists of two 2 nm gold films separated by a 20 nm silica layer in-between. 56
Figure 4.6 *In situ* transmission of a gold island film deposited on a 20 nm Al_2O_3 seed layer with varied bias values from 0 to -300 V. Diamond markers is the color of theoretical continuous gold films of thicknesses from 1 to 20 nm. Inset shows a zoomed region corresponding to the beginning of the gold deposition. The color arrows indicate toward what color hue the numerical value leans to. Each plotted markers on the figure exhibit the corresponding RGB value of the $L^*a^*b^*$ coordinates plotted. The red circled markers are attributed to the maximal a^* value on the graphic for each condition. 58
Figure 4.7 Saturation s_{ab} of the gold films in function of the deposition time for each condition. 59
Figure 4.8 Transmission spectrum at the end of the -200 V gold film deposition experiment compared with the theoretical spectra of continuous gold layers at different thicknesses. 59
Figure 4.9 The $L^*a^*b^*$ parameters of the three spectra of the left figure are: [95 0.32 0.22], [95 0.40 0.22] and [93 0.81 -0.11] for 0, -100 and -200 V respectively. The corresponding deposition time are: 22, 28 and 56 s (as identified on Fig. 4.6). 60
Figure 4.10 TEM images of the reference gold films deposited with no bias applied for a) 25, b) 50, c) 75 and d) 100 s corresponding to an effective thickness of about 1.1, 2.2, 3.3, and 4.4 nm respectively. Note: the deposition rate was 0.44 nm/s. 61
Figure 4.11 TEM images of gold films deposited with a bias value of -100 V for a) 25, b) 50, and c) 75 s. 63

Figure 4.12 TEM image of a gold film deposited with a bias value of -200 V for 75 s. 64

Figure 4.13 Statistical representation of the size and shape distribution of the islands for different deposition time & bias value. The circularity is defined as $Circularity = 4\pi \times Area/Perimeter^2$. The standard deviation of the island distribution for 0 V at 75 s was greater than the average island area due to a distribution no longer normal and was left out. 64

Figure 4.14 *In situ* color in reflection measurements in *p* polarization of a gold-island film on 20 nm Al_2O_3 seed layer during i) 40 s deposition, ii) interruption of the deposition and beginning of plasma etching at a -100 V self-bias value for 8 minutes and iii) end of etching. 65

Figure 4.15 *In situ* transmission monitoring of gold deposition on a 20 nm alumina seed-layer with -200 V bias for 1) 41 s until plasma on the target shut down and the film was 2) etched for 69 s and deposition resumed for 3) 63 s thereafter. 4) A capping alumina layer of 20 nm was deposited before a second gold-island layer growth for 5) 120 s. 67

Figure 5.1 *In situ* reflectivity (solid blue lines) and theoretical reflectivity curves (black dashed lines) of gold deposited at room temperature on B270 glass with a 20 nm SiO_2 seed layer for *s*- and *p*-polarization. 69

Figure 5.2 *In situ* reflectivity (solid blue lines) and theoretical reflectivity curves (dashed black lines) of gold deposited at different temperatures on B270 glass with 20 nm SiO_2 seed layer for *s*-polarization. 71

Figure 5.3 Evolution of *s*-polarization reflected intensity at $\lambda = 600$ nm for each temperature condition as identified from the *in situ* reflectivity measurements. The dashed circles highlight kinks in the curves. 71

Figure 5.4 Reflectivity spectra of thin gold-film on B270 substrates with a 10 nm SiO_2 seed layer at room temperature. Each spectrum of the thin film deposited (dashed black lines) are fitted with spectra from the *in situ* monitoring of the think film characterized by ellipsometry measurements (solid blue lines). The corresponding effective thicknesses of the thin-films are: a) 0.5, b) 1.0, c) 1.4, d) 2.0, e) 2.9, f) 3.9, g) 4.9, and h) 5.9 nm. 72

Figure 5.5 *Ex situ* a) extinction at 6° and b) reflectivity at 65° measurements of gold films deposited with SiO_2 seed layer and B270 substrates at room temperature. The equivalent thicknesses are: a) 0.5, b) 1.0, c) 1.4, d) 2.0, e) 2.9, f) 3.9, g) 4.9, and h) 5.9 nm. 73

Figure 5.6 TEM imaging of thin gold-film on SiN membranes deposited at room temperature for a) 0.5, b) 1.0, c) 1.4, d) 2.0, e) 2.9, f) 3.9, g) 4.9, and h) 5.9 nm. 74
Figure 5.7 Left: circularity (red) and mean area size (blue) of the island-films for δ from 0.5 to 3 nm (6 nm for the coverage). The 3 nm film size distribution was no longer normal and the larger standard deviation than the mean was left out. Right: coverage of the gold on the surface and density of the islands. The data was extracted from the analysis of the films presented in Fig. 5.6. 75
Figure 5.8 *Ex situ* a) extinction at 6° and b) reflectivity at 65° measurements of gold films deposited with SiO_2 seed layer and B270 substrates at 100°C. The equivalent thicknesses are: a) 2.8, b) 4.3, c) 6.4, and d) 11.4 nm. 76
Figure 5.9 TEM imaging of thin gold-film on SiN membranes with SiO_2 seed-layer deposited at 100°C for a) 2.8, b) 4.3, c) 6.4, & d) 11.4 nm. 77
Figure 5.10 *Ex situ* a) extinction at 6° and b) reflectivity at 65° measurements of gold films deposited with SiO_2 seed layer and B270 substrates at 200°C. The equivalent thicknesses are: a) 3.0, b) 4.0, and c) 10.0 nm. 78
Figure 5.11 TEM imaging of thin gold-film on SiN membranes with SiO_2 seed-layer deposited at 200°C for: a) 2.9, b) 4.0, & c) 9.9 nm. 78
Figure 5.12 Circularity (red) and mean island area size (blue) of the island-films for all a) 100° (except the 11.4 nm) and b) 200°C films. The 6.4 nm at 100°C and 10 nm at 200°C films size distribution were no longer normal and the larger standard deviation than the mean was left out. The data were extracted from the analysis of the films presented in Fig. 5.9 and 5.11. 79
Figure 5.13 Time derivative surface reflectance of the *s*-polarization reflectivity data of gold film deposited at room temperature. TEM images of films corresponding to each deposition time is shown to accommodate the viewer. 80
Figure 5.14 Time derivative reflectance of the *p*-polarization reflectivity data of gold film deposited at room temperature. 81
Figure 5.15 Extraction of the time derivative reflectance peak characteristics: (a) amplitude and (b) corresponding effective thicknesses when it occurs. 82
Figure 5.16 *s*-polarization TDSR for gold deposited at high temperature on B270 glass substrate with 10 nm SiO_2 seed layer. 83

Figure 5.17 Extraction of the time derivative *s*-polarization reflectance peak characteristics for the 100°C film: (a) amplitude and (b) corresponding effective thicknesses when it occurs. 84

Figure 5.18 Extraction of the time derivative *s*-polarization reflectance peak characteristics for the 200°C film: (a) amplitude and (b) corresponding effective thicknesses when it occurs. 84

Figure 5.19 The experimental data (solid) fit for gold films with the MG (dashed-dot) and BM (dashed) models with filling factor provided from TEM imaging. BM fitting thicknesses/depolarization factor for the a) room temperature 3.31 nm / 0.627 and 6.37 nm / 0.698 for 1 and 3.94 nm respectively and the b) 100° films (2.8 and 11.4 nm in order) 7.57 nm / 0.737 and 14.07 nm / 0.865. 86

Figure A.1 Schematic showing the experimental arrangement of the different samples used for the experiments: a) B7K glass with a sand blasted back zone on the back to prevent reflection from that side, b) small piece of silicon, and c) TEM membrane. Two arms are used to hold the components and a small piece of teflon tape vacuum compatible is used on one side of the silicon piece so that it sits flush on the small metal piece used to maintain the membrane in place. The membrane is held by a metal piece with a flange and the silicon piece is taped on that piece. 103

LIST OF SYMBOLS AND ABBREVIATIONS

Abbreviations

2D	Two dimensional
3D	Three dimensional
AC	Alternating Current
AFM	Atomic Force Microscopy
ATR	Attenuated Total Reflection
CIELAB	CIE 1976 $L^*a^*b^*$ color space
DC	Direct Current
EDS	Electron Diffraction Spectroscopy
EM	Electromagnetic
EMA	Effective Medium Approach
FDTD	Finite-Difference Time-Domain
FCSEL	Functional Coatings and Surface Engineering Laboratory
FMM	Family and Meakin's model
FWHM	Full Width at Half Maximum
IAD	Ion Assisted Deposition
IB	Ion bombardment
ICM	Interrupted Coalescence Model
LSPR	Localized Surface Plasmon Resonance
NB	Nanobar
NP	Nanoparticle
NPC	Nanoparticle Chain
PVD	Physical Vapor Deposition
RF	Radiofrequency
RRC	Reflectivity Rate of Change
SEM	Scanning Electron Microscopy
SERS	Surface Enhanced Raman Spectroscopy
SPP	Surface Plasmon Polariton
SPR	Surface Plasmon Resonance
LSP	Localized Surface Plasmon
LSPR	Localized Surface Plasmon Resonance
TEM	Transmission Electron Microscopy
XPS	X-ray Photoelectron Spectroscopy

XRR	X-ray Reflectometry

Materials

Ag	Silver
Ar	Argon
Au	Gold
Al_2O_3	Alumina
SiO_2	Silica
TiO_2	Titania
MgO	Magnesium oxyde

Symbols

α	Angle aperture
γ	Surface energy
Γ	Damping factor
δ	Effective thickness
Δ	Ellipsometric parameter associated with the phase difference
ε	Dielectric
ε_{eff}^{BM}	Bruggeman effective dielectric constant
ε_{eff}^{MG}	Maxwell-Garnett effective dielectric constant
ε_h	Dielectric function of the host matrix
ε_m	Dielectric function of the metallic inclusion
ζ	Damping ratio
θ	Angle of incidence
θ_{cr}	Critical coverage
λ	Light wavelength
ν	Transformation vector
ρ	Polarization amplitude ratio
σ_1	capture number of adatoms
σ_x	capture number of stable clusters
τ_a	Characteristic evaporation time
τ_c	Characteristic capture time
ϕ	Phase shift

χ	Electric susceptibility
	Ellipsometric parameter related to the polarization amplitude ratio
ω	Angular frequency
ω_p	Plasma frequency
ω_{SPR}	Surface plasmon resonance frequency
ω_0	Resonant frequency
Ω	Surface area of a spherical cap
a	Spherical nanoparticle radius
a^*	Green-red axis in CIELAB color space
A	Absorption
b^*	Yellow-blue axis in CIELAB color space
C_{abs}	Absorption cross-section
C_{scat}	Scattering cross-section
d	Thickness
D	Surface diffusion coefficient
D	Dimension
D65	Standard illuminant CIE D65
$\vec{E}$	Electric field
E_a	Activation energy
E_d	Diffusion energy
E_e	Evaporation energy
E_i	Ion energy
Ext	Extinction
f	Filling factor
F	Atom flux
g	Depolarization factor
I	Spectrum intensity
I	Reference illuminant
I_s	s-polarization intensity
I_p	p-polarization intensity
$\mathtt{k}$	Spring constant
L^*	Luminance axis in CIELAB color space
M	Transfer matrix
n	Refractive index
n_1	Adatom density
n_x	Stable cluster density

N	Complex refractive index
N_{inc}	Incident light medium refractive index
N_{ext}	Exit medium refractive index
N	Amount of passes before delamination
N_e	Electron density
N_i	Island density
$\vec{p}$	Dipole moment
p	Momentum
P	Probability
$\vec{P}$	Polarization vector
Q	Quality factor
r	Reflection coefficient
r	Nanoparticle radius
r	Optical microscope resolution
$\vec{r}$	Displacement vector
r_p	Fresnel reflection coefficient for p polarized light
r_s	Fresnel reflection coefficient for s polarized light
R	Island radius
R	Reflectivity
R_c	Rate of adatoms condensation
s_{ab}	Color saturation in the CIELAB color space
S	Scattering
S	Spectral reflectance or transmittance distribution
t	Transmission coefficient
t	time
T	Transmission
V	Volume
$\mathsf{x_r y_r z_r}$	CIE normalized reference white
$\mathsf{x}_\lambda \mathsf{y}_\lambda \mathsf{z}_\lambda$	Standard photometric observer color-matching function
XYZ	CIE 1931 tristimulus values
Z	Film coverage

Physical constants

ε_0	Free space permittivity
μ_0	Free space permeability
k_b	Boltzmann's constant

h	Planck's constant
e	Elementary charge
m_e	Electron mass

LIST OF APPENDICES

Annexe A A 103

CHAPTER 1 INTRODUCTION

Optical coating alters the way an object reflects and transmits light. Anti-reflection coatings (ARCs) are widely used to attenuate unwanted reflection and increase the transmission of an optical component. Modern ARCs rely on the destructive interference of reflected light from multiple interfaces so that the reflected intensity is effectively suppressed for the visible range ($380-700$ nm). Additionally, constructive interference can instead promote reflectivity of specific frequency to generate vivid colors. However, the performance of such coating is dependent on light's angle of incidence resulting in an alteration of the coated surface appearance when looked upon from different points of view. This effect generally results in the emergence or shift of coloration which is often undesirable.

Due to the aforementioned angle-dependent performance of interference-based optical coatings, color generation is more often realized through the incorporation of pigments which relies on the absorption of a portion of the visible spectrum to alter the reflected and transmitted intensity, a process angle-insensitive [1]. Absorption of light is caused by electronic transitions and subsequent non-radiative decay of the excited state. A radiative decay can also follow non-radiative relaxation, which is fluorescence or phosphorescence.

Despite wide industrial use, an alternative to pigment coloration is sought due to the recycling difficulty arising from the wealth of possible chemical compounds rendering the sorting and subsequent reuse of the material challenging. Moreover, waste generation is a serious environmental concern and a single tuneable coloring agent would greatly facilitate the recycling process [2]. The foregoing environmental threat can be solved with the nanoengineering of nanocomposite, *i.e.* a multiple-phase material with one phase having at least a feature in the nanometric scale ($< 100\ nm$) [3], to meet our needs for sustainable color generation. The present chapter introduces the proposed solution, the research context and the targeted application for this study.

1.1 Plasmonic color

Archaeological discoveries of potteries dating from the end of the 10th BC-century were found with atypical colors (yellow-greenish and green-golden); and composition analysis revealed minute silver and copper inclusions at the origin of the atypical coloration [4]. It was not until Gustav Mie solved the Maxwell's equations for a sphere of arbitrary size and optical constants in 1908 [5] that this behavior could be attributed to the presence of metallic NPs

in the ceramic. Indeed, the unusual coloration of the artworks can be associated with collective electron oscillations of the free electrons confined inside of the metallic nanoparticles (NPs) [6]. The coupling of light with the free electrons of metals can generate surface plasmon (SP) [7] and scientific study of this light/free electrons interaction is named plasmonic. A famous example of this phenomenon is the Lycurgus cup, an antique Roman 4th-century dichroic glass, shown in Fig. 1.1 that exhibits distinctive color in reflection and transmission. The composition, size, shape and surrounding media of the NPs determine a resonant frequency for which light couples strongly with the electron cloud. Henceforth, electromagnetic (EM) waves can be converted into electron oscillations leading to either light absorption or scattering. Variation of the NPs' size and concentration is at the origin of the broad variety of observed plasmonic colors [8]. Thus, the modification of a composite's nanostructure provides a way to tailor the optical properties to selectively affect light propagation, without the need to resort to a compounds palette to generate varied colors.

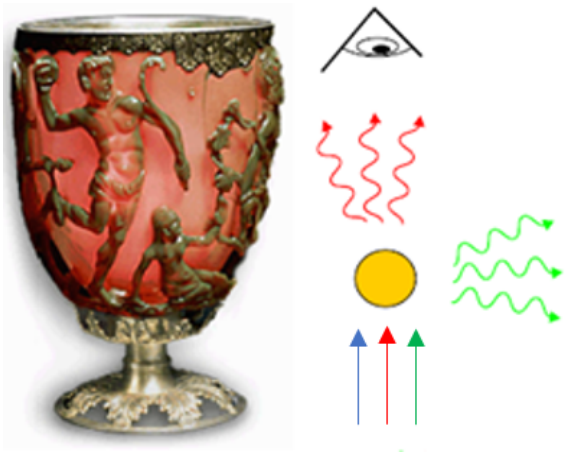

Figure 1.1 The famous Lycurgus cup illuminated from behind. Light absorption by the gold nanoparticles generates a red (transmitted) color whereas the scattered light yields a green (reflected) color. Adapted with permission from Novotny *et al.* [9].

1.2 Applications

The free-electron cloud confined within a metallic NP exhibits a resonant frequency for which light coupling is intense, inducing localized surface plasmon resonance (LSPR) that is charge density oscillations at the particle surface [10]. Coherently oscillating electrons are akin to a nanoantenna, radiating an electromagnetic (EM) field [11] that is locally much more intense than the external field that generated the LSPR. This attribute allows great sensitivity enhancement for Raman spectroscopy [12] to the point that the detection of a unique molecule

is now possible [13]. Moreover, the resonant condition is affected by the NP's surrounding media enabling refractive index sensing and detection of any changes attributed to concentration variation of compounds [14] or even the determination of contaminant content in water such as mercury [15] and lead [16] with gold NPs. Notwithstanding their popularity for sensing applications, metal NPs can improve the efficiency of solar cells due to the lengthening of the optical path inside of the device caused by scattering [17]. Additionally, gold NPs were found to have catalytic activity combined with TiO_2 [18], CeO_2, ZnO and Fe_3O_4 [19].

Aside from color generation, light filtration can also block harmful radiation. Lack of blink reflex for the near-infrared (NIR) radiation necessitates protection to prevent permanent eye damage from laser expositions for example. Contact lenses with incorporated gold nanoparticles were found to shield close to 50% of the incident intensity from dangerous NIR expositions [20]. Furthermore, one should find that new and unique optical constant generation through plasmonic-based materials can rapidly lead to the design of novel optical filters.

1.3 Research context

In recent years, composite ophthalmic glass/plastic has been developed due to plastic's low cost, low weight, good optical properties and ease of manufacture. Corrective eyeglasses for improved vision have gained in complexity to offer a better performance including high transmission, good mechanical durability and other features such as hydrophobicity or oleophobicity [21]. Such a lens is depicted in Fig. 1.2 and a plasmonic layer could be added to the thin-film stack or to replace an existing layer.

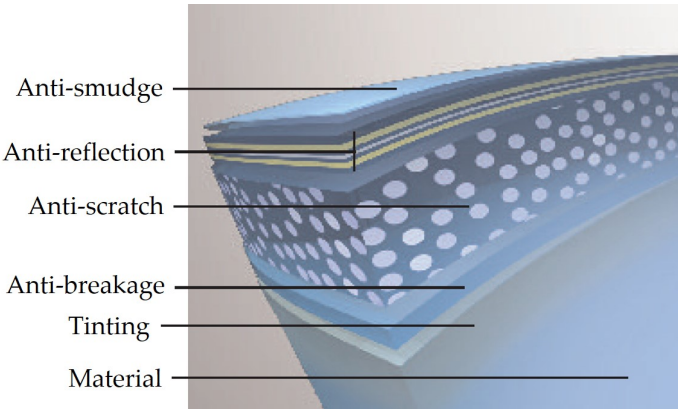

Figure 1.2 Structure of a modern ophthalmic lens showing the thin film stack architecture to provide high transmissivity and good mechanical durability. Adapted with permission from D. Meslin [21].

The most popular base material used for marketed plastic lenses is known as the polymer

CR 39 which stands for *Columbia Resin* # 39 originally developed by the American company Pittsburg Plate Glass (PPG). This thermosetting resin has excellent optical properties, *i.e.* low refractive index (1.5) and dispersion [22]. Essilor, the leading world manufacturer of ophthalmic lenses, is using this polymer under the brand name Orma. However, this type of polymer has a low melting point [23] which renders the use of high temperature in the fabrication process impossible for plastic-based ophthalmic lenses. Post-deposition annealing or elevated surface temperature is known to favor the de-wetting of metal films, favorable to island formation [24, 25]. This process parameter is particularly important for vapor deposition methods to improve NPs size distribution.

Some deposition methods offer mass-selected NPs deposition such as gas-phase aggregation [26], ligand [27] along with metal salt reduction [28, 29] and to some extent electrospray deposition [30]. While these methods provide precise control over the size of the NPs, it's not the case for the filling factor and material composition [31], two critical parameters for the aforesaid applications. Physical vapor deposition (PVD) has been used with great success for sputtering [32] and evaporation [33] of gold clusters over large surfaces. Although, the growth kinetics of the film must be understood to control the morphology and subsequently the optical properties. Moreover, an alternative to heating must be investigated to offer a means to control the NPs size distribution with PVD on polymers.

The work in this master's thesis is motivated by the still unexplored applicability of plasmonic thin-films for ophthalmic lenses in the context of light filtration and aesthetic purposes. As such, the incorporation of a plasmonic layer could serve as a new means to generate fashionable colors. Although, the use and development of colored glasses and lenses is not just a question of vanity as it has been found that color discrimination for color-blind individuals was improved by restricting light transmission bellow 590 nm [34]. However, tinted ophthalmic lenses can negatively impact the wearer's color differentiation capability if the color exceeds 20% of excitation purity, *i.e.* how much the color is filtrated [35]. Thus, tinted lenses use is generally not advisable except for the particular forenamed case of color blindness and aesthetic purposes.

The CR 39 polymer UV cutoff is 355 nm, insufficient to protect from UVA radiation which requires a cutoff at 400 nm to properly protect the wearer. A tinted lens with unacceptable UV protection exposes the wearer to even greater risk of suffering adverse effects from UV exposition since the closing reflex of the eyelids and reduction in papillary diameter is not triggered by UV light [21]. This drawback can be mitigated with the addition of an UV-filter. However, these filters are relatively thick ($\sim 6 - 10$ μm) and require post-deposition treatment for the tinting agent to penetrate the coating which is more often done before

the anti-scratch layer is deposited [21]. Hence, the general objective of this project is to evaluate what a plasmonic layer can achieve in term of light filtration and color to ease the manufacturing process by offering a mean to generate a film of wanted optical properties inside of a PVD system. Additionally, plasmonic filters have diverse and adjustable optical properties, enabling NIR filtration but also paving the way for sustainable color generation.

Consequently, the project consists of three specific objectives:

i) Demonstration of the achievable plasmonic colors and the different means to tune them.

ii) Evaluation of the plasmonic layer durability deposited on an organic lens.

iii) Recommendations (architecture and material choice) to maximize the performance of the plasmonic layer.

As a result, the essence of this master's thesis is to understand how plasmonic color can be controlled and, secondly, how the optical properties of a thin metal film are affected by the nanostructure which in turn influences the durability of the plasmonic layer.

1.4 Scientific contribution

Optical monitoring work conducted to understand the correlation between a gold-islands film optical properties evolution and its morphology has led to a presentation at the Optical Interference Coating (OIC) 2019 conference.

Table 1.1 OIC proceeding paper reference.

A. Riera, B. Baloukas, O. Zabeida, L. Martinu, Optimizing the Deposition of Sputtered Gold Island Films with Time Derivative Surface Reflectance, *Optical Interference Coating*, New Mexico, United States, June 2-7, 2019.

1.5 Thesis outline

The thesis is organized in 6 chapters. In the first chapter, the subject is introduced and the objectives defined. In the second chapter, a general introduction on the multiples subjects ranging from the growth dynamic of island films deposited with PVD to the theory surrounding their optical properties is complemented with literature on the addressed subjects. Thereafter, the experimental methodology describes the deposition system, the characterization apparatus, and techniques used through this work to conduct the experiments. The fourth chapter presents the color and durability of gold films deposited and how color can be tuned with ion bombardment. The fifth chapter discusses theory and results focusing on the *in situ* time-derivative reflectivity measurements. The last chapter summarizes the results followed by a conclusion and discussion about future work.

CHAPTER 2 LITERATURE REVIEW AND THEORY

2.1 Foreword

This chapter aims at introducing the underlying principles behind sputtering and the advantages of the method compared to evaporation in the context of metal-island film deposition. Both sputtering and evaporation are popular deposition methods in the industry but differences inherent to the process renders sputtering particularly advantageous within the framework of this research.

Secondly, the growth kinetic of metal-island films will be thoroughly investigated. Indeed, since this study's objective is to exploit the film's natural tendency to grow as an island film to control the optical properties of a composite material, a good knowledge of the atomistic processes of growth is mandatory. Later, the impact of ion bombardment on the growth of metal-island films is explored.

A general introduction on the origin of metals' optical properties is provided to better understand the origin of their peculiar behavior especially as nanoparticles. Further on, details are given concerning the various parameters that significantly affect a metal-island film's optical attributes. Finally, the evolution of a gold film's optical behavior is explained according to the underlying microstructure of the corresponding growth stage.

2.2 Physical vapor deposition

Physical vapor deposition (PVD) includes all processes characterized by thin film deposition from a vapor phase. Materials have a vapor-pressure point characterized by the equilibrium between their condensed and vapor phases in a closed system. The vapor phase can condense back on the surface of the enclosing system. This principle allows the use of a source material that is brought to a temperature where it is not in equilibrium with its vapor phase so that atoms from it can be transferred onto a cooler surface.

Thermal evaporation and sputtering are two popular PVD methods. The former is rapidly described in the historical context of thin gold film deposition. Sputtering is the method of choice for this study and is extensively detailed.

2.2.1 Thin gold film deposition by evaporation

Modern evaporation systems rely on a a high vacuum to grow thin films from a source material. Furthermore, the method allows the deposition of a broad variety of elements and compounds. The working principle is straightforward and resides in the heating of a material by some means that causes it to evaporate at a rate depending on its temperature.

Faraday was one of the first to experiment with evaporated films. Using the exploding wire method, he deposited thin gold films from gold leaves with varying parameters such as the atmosphere content and the pressure [36]. He was able to confirm that the evaporated thin gold film was optically and chemically identical to those he had produced through chemical methods. Indeed, gold was known to generate a variety of colors and its solubility in different acids and solutions allowed Faraday to confirm that the deposited film was gold of a purity comparable to that of the wire.

The impact of temperature on the deposition of gold offered a striking contrast of color due to the nonuniform heating of the discharge. Faraday could see a ruby tint where the heat had been the most intense. Furthermore, on that location, the gold could not be wiped off from the surface, suggesting that it was embedded into the glass, producing a color akin to the decorative glasses exhibited in churches. Subsequent heating of the film where the heat generated by the wire explosion had been less intense, produced an extraordinary change with the film's color going from violet, blue, or green in transmission into a ruby color while preserving metal-like reflecting behavior [36].

It was not until Mie, in 1908, solved the Maxwell equations for spherical particle inclusions in a dielectric matrix for the extinction and scattering cross-section that the peculiar behavior of metallic nano-particles could be explained [5].

2.2.2 DC diode sputtering

Grove was the earliest experimenter who observed metal depositing from the cathode of a glow discharge plasma in 1852 [37]. During one of his experiments, he noticed that when two wires of a battery terminal were put in proximity so that an arc would form, the positive end became red incandescent while the negative end remained relatively cool. Subsequent experiments under various atmospheres showed that he could obtain a deposition from different metal wires but he was unable to explain precisely what was the underlying physical phenomenon. However, he did have the intuition that the molecules in the atmosphere somehow interacted, preferentially with the cathode and so electrically charged species had to be involved in the phenomenon. Being one of the first to do this discovery, it still wasn't known that it was

charged atoms that struck the cathode and ejected atoms from it [38]. This observation can be explained considering that the positive ions are attracted to the cathode and momentum transfer to the electrode's surface will sputter some atoms. This deposition process is known as DC sputtering.

Sputtering is another physical vapor deposition technique allowing to produce thin films that relies on the kinetic energy of positively charged atoms from an ionized gas, *i.e.* a plasma, to eject particles from a negatively charged target through momentum transfer, usually at room temperature. The application of an electrical potential between two electrodes can generate a glow discharge. The electric field will accelerate any stray electron arising by some means, *e.g.* cosmic rays, toward the anode [39]. At a gas pressure of $\sim$ 100 mtorr, the electron is likely to have an ionizing collision with a gas atom between the electrodes. The ionized atom and the ejected electron immediately accelerated by the electric field and additional ionization events rapidly create new charged species. The higher mobility of the electrons comparatively to the ions, due to the significant mass difference, causes a charge imbalance since electrons leave the plasma at a faster rate. In turn, the plasma charges positively and a steady state is reached when the potential of the plasma is high enough to bring down the loss rate of electrons to that of the ions. The resulting ionized gas is a quasineutral gas displaying collective behavior upon electromagnetic field application [38]. The ionization fraction of the charged gas is in the range of 10^{-5} to 10^{-1} resulting in an electron density of 10^{9} to 10^{13} cm^{-3} depending on the process parameters [39].

Secondary electron emission from the target material is possible upon ion impact which helps to maintain the glow discharge. The working gas used is argon due to its inertness and abundance. The optimum operating condition for cathodic sputtering is around 100 mtorr. At this pressure, a good balance between ionization efficiency necessary to sustain the cathode discharge and the deposition rate is met. Indeed, higher pressures increase the likelihood that the sputtered atoms undergo collisional scattering, deflecting them toward the chamber's wall instead of the substrate's surface [38].

2.2.3 RF diode sputtering

If the cathode is of an insulating material, the restricted current flow will prevent the cathodic discharge to be generated in a conventional diode DC sputtering system [39]. To overcome this limitation, radio-frequency (RF) power operating at 13.56 MHz (standardized frequency for plasma processing) is applied on the electrodes. In essence, the working principle of an RF-powered discharge remains the same as its DC counterpart. The high voltage applied across the electrodes initiates a glow discharge except that the potential oscillates with time.

Since the electrons can quickly respond to the alternating voltage, the change of polarity of the electrodes will reflect them back and forth. This effect greatly reduces the need of secondary electron emission from the target to sustain the discharge and allows the use of lower pressures. Moreover, a proper impedance matching of the RF voltage allows to sputter a material independently of its resistivity.

A target self-bias to a negative potential arises from the asymmetric behavior of the discharge current-voltage curve emerging from the limited positive ion mobility [38]. During the positive half of the cycle of the alternative current (AC) signal, a large electron current is drawn whereas, during the second half, very little ion current flows. This results in a net current that cannot happen and, as a result, negative charge accumulations induces a voltage shift that compensates for the excess electron current. This self-bias acts akin to a DC voltage and positive ions are accelerated toward the target and through momentum transfer, it is sputtered - in the same fashion of DC sputtering.

2.2.4 Magnetron sputtering

The ionization efficiency can be further increased with the addition of permanent magnets underneath the target that generate magnetic field lines perpendicular to the electric field. Indeed, electrons are subjects to a force perpendicular to the magnetic field and their momentum direction, causing them to spiral. The alternating electrical field further traps the electrons in a drifting cycloidal motion along the direction where electrical and magnetic fields are perpendicular [39]. Furthermore, this orbital motion of the electrons increases the ionization probability which locally densifies the plasma where the fields are orthogonal. Consequently, the sputtering of the target is the most intense right underneath this zone and, with time, a typical erosion track appears on the target for this deposition method called magnetron sputtering.

2.2.5 Reactive sputtering

So far, the atmosphere considered was that of inert species. However, a plasma of reactive gases such as nitrogen, oxygen, carbides or sulfides can react with sputtered atoms by an inert working gas (usually Ar) from a metallic target on the substrate. The resulting film is either a solution of the target material with the reactive element (*e.g.* $AlO_{0.02}$), a compound (*e.g.* Al_2O_3) or a mixture [38].

One problem with reactive sputtering is the target poisoning which is attributed to the formation of a compound directly on it. This effect alters the dynamics of the plasma and is

accompanied by a decrease in the deposition rate and even an interruption of the discharge. It is mitigated by adjusting the ratio of the reactive gas so that the inert ions can sputter away the compound faster than it can form. Also, a pre-sputtering of the target with only inert species is mandatory to bring back the target in a metallic state, *i.e.* free of any compounds. Many metallic targets oxidize when exposed to the atmosphere and if no pre-sputtering with an inert species is done before reactive sputtering deposition, one will observe drastic differences, *i.e.* hysteresis, in terms of deposition rate until the target is brought back to a pure metal state [38].

2.2.6 Sputtering over evaporation

Emphasis has mainly been put on sputtering despite that both methods allow the deposition of a multitude of elements and compounds. The main difference resides in the physics of the process. Indeed, sputtered atoms are about two orders of magnitude more energetic than their thermally evaporated counterparts [40]. Also, in a specific study of Ag thermal evaporation, only 0.1% of the evaporated atoms were found to be positively charged which is about one order lower than in sputtering [40]. Additionally, due to the higher kinetic energy of the impeding sputtered atoms, it is expected that the produced film should be comparable to a film evaporated at a higher substrate temperature.

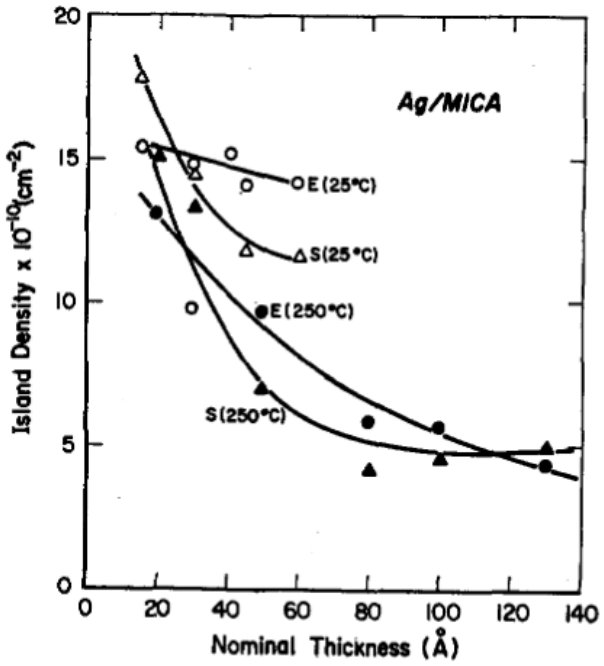

Figure 2.1 Evolution of the island density for sputtered (S) and evaporated (E) Ag/mica films at 25°C and 250°C [40].

The rapid decrease of the sputtered island density depicted in Fig. 2.1 is due to the higher mobility of the adsorbed atoms and promotion of island coalescence. More details concerning this behavior of the film growth at higher temperatures follow in the next sections. The difference between the two deposition methods is mainly due to the rise in the substrate's surface temperature due to the momentum transfer of the impeding atoms with contribution from electrons and argon ions bombardment. Lau *et al.* have determined that the contribution of the plasma and the cathode radiation is negligible compared to the latent heat of condensation and the electron bombardment for DC and RF sputtering. Indeed, sputtered atoms have an energy of 10 eV and higher for 1 keV Ar ions and the ΔH for gold is 3.5 eV. It's thus estimated that 20% of the heat comes from the sputtered atoms and the remaining 80% is probably due to the bombardment of secondary electrons and argon ions [41]. The temperature is also dependent on the deposited material's emissivity as it is the primary heat loss mechanism along with the heat transfer to the substrate holder.

2.3 Growth of island films

The deposition conditions such as the temperature of the substrate and the deposition rate both have an impact on the growth of thin films. To take advantage of a film's natural tendency to form as islands, one must understand what drives atoms to form a thin film. The different parameters influencing the capability of the atoms to arrange as 3D clusters are explored. Further on, the growth of an island-film is described in terms of different regimes associated with a specific morphology.

2.3.1 Growth modes of thin films

The main thin-film growth modes are depicted in figure 2.2. At equilibrium, the deposited film F on the substrate S has created a new surface film-vacuum with an interface film-substrate whereas the substrate-vacuum surface decreased [42, 43]. The respective surface energies of the interfaces are: γ_F γ_{FS} γ_S. The equilibrium equation can be written as the energy balance of the surface energies $\Delta\gamma = \gamma_F + \gamma_{FS} - \gamma_S$. For $\Delta\gamma \leq 0$ the growth behavior is that of Frank-van-der Merwe mode (Fig. 2.2a: layer-by-layer growth) whereas, for $\Delta\gamma > 0$, the covering of the substrate is not thermodynamically favorable and the growth is of Vollmer-Weber (Fig. 2.2c: island growth). The Stranski-Krastanov growth (Fig. 2.2b: layer plus island) depicts the case when the interfacial energy increases after the substrate has been covered, triggering island growth.

The presented growth models assume a thermodynamic equilibrium meaning that if allowed

to, the system will settles for a morphology that minimizes the surface energy. However, during deposition, the film cannot reach thermodynamic equilibrium since the material is constantly being added. Moreover, a simple kinematic model allows one to determine that the island density N is related to the adatom diffusion constant $D = D_0 e^{-E_a/k_b T}$, surface diffusion activation energy E_a and flux of deposition F by a proportional relation $N \propto (F/D)^{1/3}$ [44]. Thus, under kinetic conditions (supersaturation of adatoms), a quasi-2D growth is possible due to the high nucleation rate even in the case where $\Delta\gamma > 0$ [45]. Also, the deposition conditions, *e.g.* deposition rate and temperature, will affect the growth dynamics and in return the resulting structure.

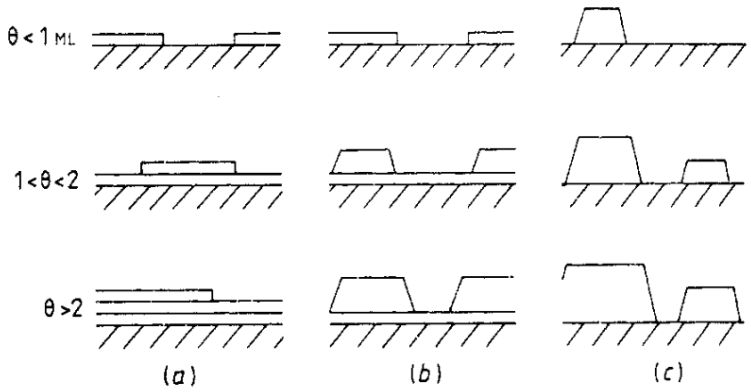

Figure 2.2 The three main growth modes are schematically represented here: (a) layer-by-layer (Frank-van der Merve), (b) layer plus island growth (Stranski-Krastanov) and (c) island growth (Vollmer-Weber) with θ the coverage in monolayer (ML). Taken with permission from Venables *et al.* [46].

2.3.2 Growth kinetics

Nucleation and crystal growth for vapor deposition can be decomposed into several atomistic processes [46]. The condensation of vapor on the substrate generates an adatoms density n_1 and these atoms diffuse on the surface until one of the processes depicted in Fig. 2.3 occurs. For each of these processes, a characteristic time is associated that mainly depends on the flux of condensing atoms and the surface temperature.

Venables *et al.* [47] have formulated the following rate equations for adatom density n_1 and

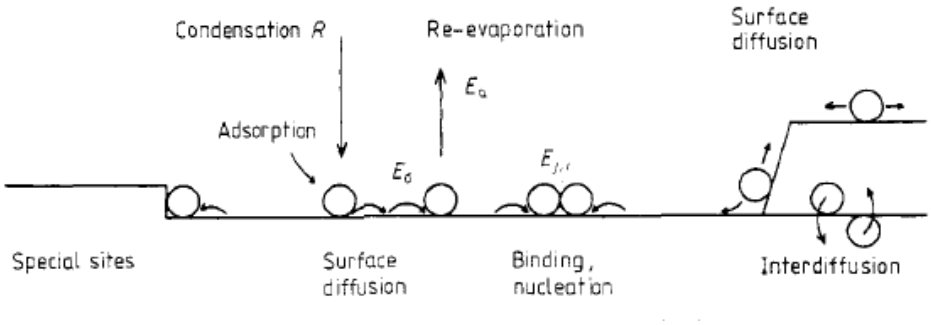

Figure 2.3 The atomistic processes and energies associated with nucleation and growth on surfaces. Taken with permission from Venables and Spiller [47].

stable cluster (of a size greater than 1 atom) n_x evolution:

$$\frac{dn_1}{dt} = R_c(1 - Z) - n_1\tau_\alpha^{-1} - D\sigma_x n_1 n_x - 2D\sigma_1 n_1^2 \tag{2.1}$$

$$\frac{dn_x}{dt} = D\sigma_1 n_1^2 - 2n_x\frac{dZ}{dt} \tag{2.2}$$

$$\frac{d(n_x\omega_x)}{dt} = R_c Z + D\sigma_1 n_1^2 + D\sigma_x n_1 n_x \tag{2.3}$$

with R is the rate of condensing adatoms, D is the diffusion coefficient and τ_α is the characteristic evaporation time of an adatom. σ_1 and σ_x are both capture numbers of adatoms and stable clusters respectively with the former depending on the total coverage of the atoms Z. $D\sigma_x n_x$ can be expressed as the characteristic capture time τ_c. The first term of Eq.(2.1) is the flux of condensing atoms on the substrate. The second term is the loss of adatoms due to re-evaporation, the third is associated with the stable cluster capture of adatoms and the last term the nucleation of two diffusing adatoms. On Eq. (2.2)'s right-hand side, the first term is the increase of stable clusters due to adatom capture by adatom. The second term is the coalescence of two stable clusters. The third equation is the evolution of the amount of atoms w_x in stable clusters n_x.

Reichelt *et al.* [48] used previous results to determine diffusion E_d and evaporation E_e energies to numerically integrate Eqs. (2.1), (2.2) & (2.3) which highlight the temperature dependence and deposition rate of adatoms and clusters as shown in Fig. 2.4 (impact of deposition rate shown elsewhere [49]).

From this result, 3 regions can be identified. First, the adatom density n_1 rises which increases the desorption term $n_1\tau_\alpha^{-1}$ until this term is equivalent to the adsorption term, resulting in a peak of adatom density. This balance is nonexistent at lower temperatures and sustained for a significant amount of time at higher temperatures. The lower adatom density

n_1 with increasing temperature is attributed to the smaller characteristic evaporation time $\tau_\alpha \propto e^{E_a/k_bT}$. Because there are less diffusing adatoms, the nucleation rate is slower. As a consequence, the probability of adatom capture by a stable cluster is more likely (n_1^2 vs $n_1 n_x$). Finally, the density of adatoms decreases as the coverage progressively increases up to a point when the average distance between the clusters is smaller than the diffusion length of the adatoms. Further deposition is characterized by growth only possible via direct adsorption of impinging atoms on clusters (term RZ of Eq. 2.3).

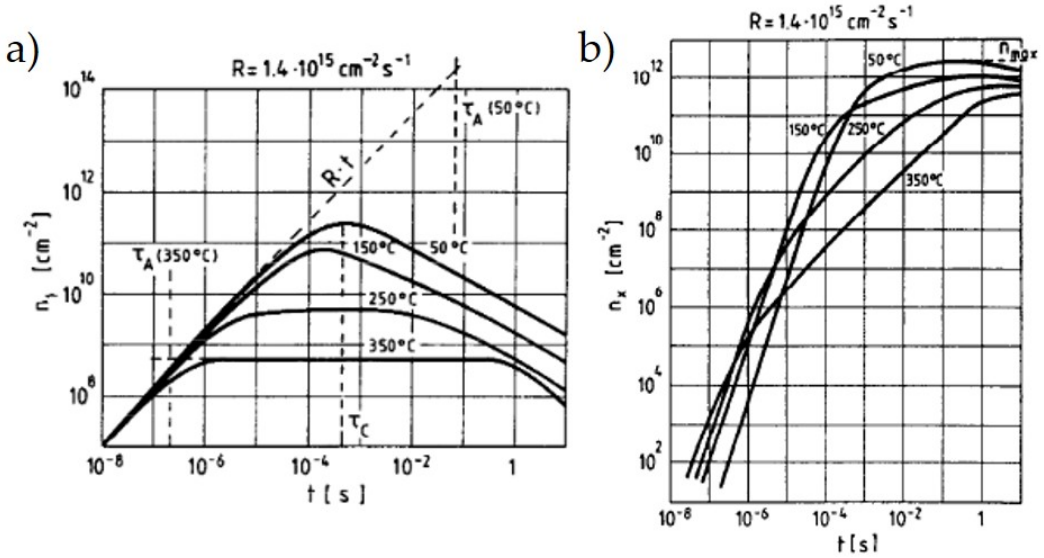

Figure 2.4 (a) Calculated adatom concentration n_1 and (b) stable cluster concentration n_x for an atom flux rate $R = 1.4 \cdot 10^{15}\ cm^{-2}s^{-1}$ of gold on NaCl at various surface temperatures. Taken with permission from Reichelt *et al.* [49]

2.3.3 Surface diffusion

As discussed previously (section: 2.3.2), the diffusion coefficient scales with temperature but the atomistic processes of surface diffusion are also characterized by an activation energy E_d. Not all diffusion steps have equal diffusion energies as illustrated in Fig. 2.5 and for an atom (copper in this example) on the edge of a cluster, hopping onto the terrace is prevented by the so-called *Schwoebel* barrier (represented by E_1) [50]. From this remarkable observation, one can wonder how 3D growth can be favorable when atoms are systematically attracted to the island's edge.

Experimentally, a 2D island growth is initially observed up until a critical 2D island radius when 3D growth becomes favored [51]. This phenomenon can be explained by considering that it's even more favorable for an atom to attach to the edge of a second layer [50]. This

explanation proposed by Ernst *et al.* was further confirmed by considering that even at 130 K, atoms can hop onto the terrace and diffuse back toward the 2D island edge [52]. However, as the perimeter of the cluster grows, more atoms have a chance to hop onto the terrace and meet another diffusing atom, forming a second layer that promotes even more atoms to join them.

Parker et al. have studied the effect of deposition rate, surface defect and temperature on the critical island size before 3D growth is initiated. Fig. 2.6b shows the impact of surface defects that delay the vertical growth of the islands the higher the density of surface defect is. Interestingly, the deposition rate had no impact.

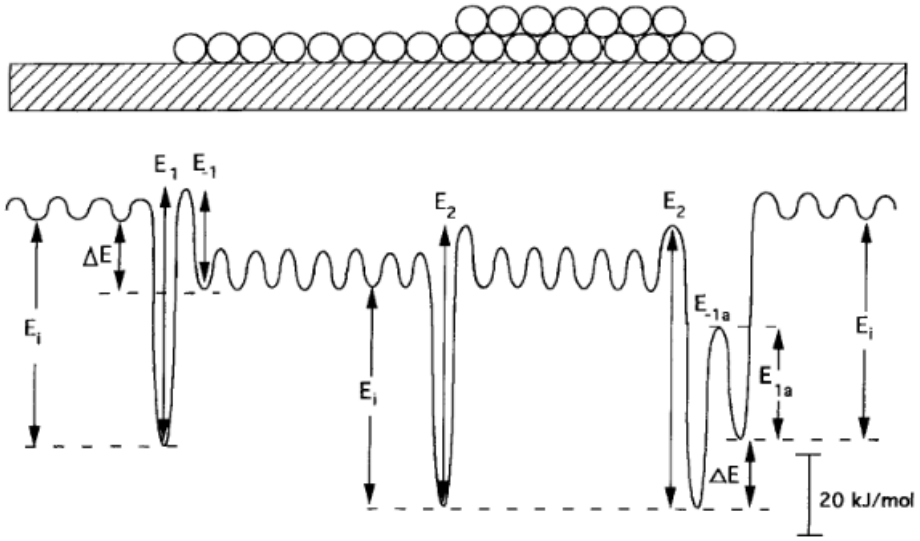

Figure 2.5 Side view of ZnO surface with a Cu island with a simplified energetic diagram highlighting the energy difference of diffusion barriers a Cu atom will encounter while diffusing. From Campbell *et al.* [50].

Additionally, increasing the temperature decreases the critical coverage θ_{cr} before the 3D growth transition [51]. In light of this study, it can be established that surface defects act as potential traps for atoms, preventing edge diffusion onto the cluster's terrace. Moreover, an increase of temperature favors diffusion and consequently the density of atoms on a terrace which accelerates the formation of a second layer, paving the way for other atoms to hop on.

Atoms are thus quite active, constantly shifting position, looking for some lower potential site to sit on. This random motion of atoms causes the cluster to move. Indeed, an atom detaching from the step edge can reattach to the step edge at the other side of the cluster after diffusing on the terrace. As a result, the island has translated and this random (Brown-

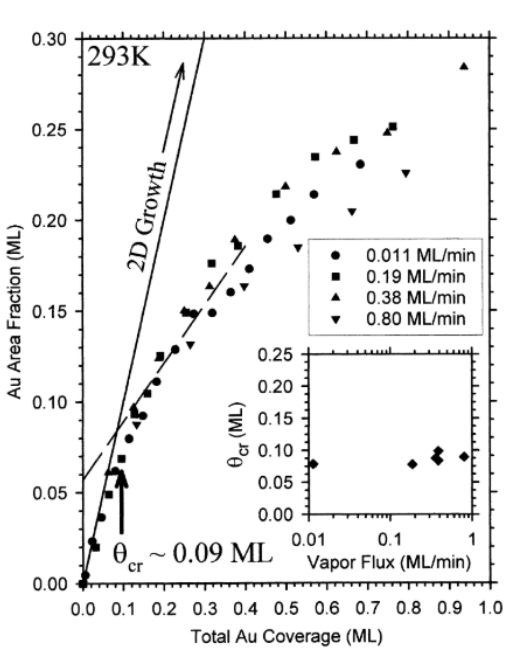

(a) Four different fluxes show no relationship with the critical coverage.

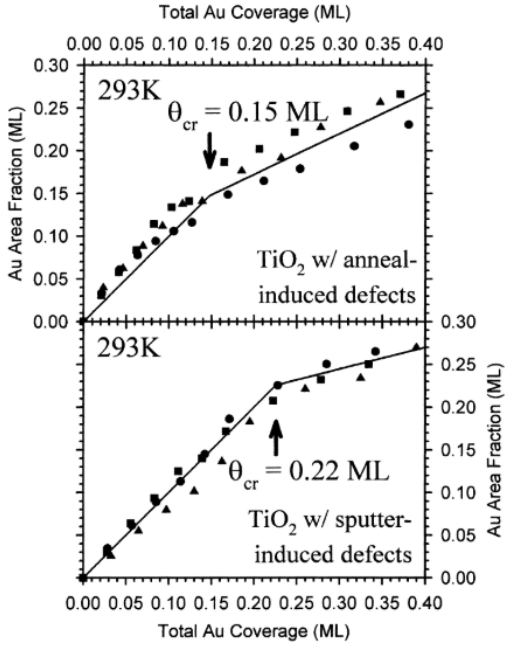

(b) The critical coverage is shifted toward greater values the more defects on the surface.

Figure 2.6 Gold deposition on TiO_2 shows a transition from 2D to 3D growth at a critical coverage θ_{cr}. The surface defects were induced by a thermal anneal at 900 K in O^2 atmosphere with the sputter-induced defects sample having an additional surface treatment of 1 keV Ar^+ plasma etch. Taken with permission from Parker *et al.* [51].

ian) motion has been observed with scanning tunneling microscopy [53]. This island motion can lead to coalescence, a process named Smoluchowski ripening [54]. Typically, only small islands tend to diffuse and coalesce. Atoms can also escape an island, but the likelihood of atom detachment is inversely proportional to the cluster's radius due to the greater surface/volume ratio [38]. Hence, the growth of larger clusters is amplified because they tend to lose proportionally fewer atoms and the larger surface area increases the capture probability of diffusing atoms [55]. This phenomenon is known as Ostwald ripening.

2.3.4 Coalescence process

The metal of interest for this study is gold due to its tendency to naturally grow as an island film on various oxide surfaces and its chemical stability alongside with peculiar optical properties. The wetting of a gold island on the surface of a substrate depends on the surface energy of the gold-substrate, gold-vacuum, and vacuum-substrate system and the minimization of the surface energy dictates the system's morphology, *i.e.*, the islands' shape. However,

during the nucleation and growth of islands, the initial shape is not necessarily in the most stable form due to topological and chemical constraints [56, 57]. Indeed, surface inhomogeneity can pin the island perimeter, preventing it from relaxing as the edge atoms cannot diffuse. This effect is particularly important during the coalescence of two islands, a surface diffusion mechanism [58]. During the process of island fusion, one grain orientation grows at the detriment of the other and the final island is a perfect crystal [59]. However, for this process to complete, atoms from one grain must diffuse past the boundary, a surface diffusion mechanism dependent on the activation energy [60] of the atomistic processes involved (see section 2.3.3).

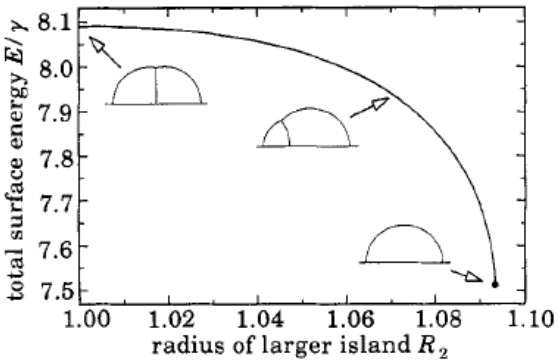

Figure 2.7 Calculated surface energy of two metal islands coalescing with a grain boundary separating them as a function of the radius of the bigger island (right). Taken with permission from Duxbury *et al.* [56]

As depicted in Fig. 2.7, the surface energy curve is nearly flat for similarly sized coalescing islands and, so, any substrate irregularity or contamination can trap the cluster into a metastable state where diffusion past the grain boundary is not favorable despite the island's surface energy not the most optimal (single crystal). This effect is amplified with other islands attaching to a metastable pair which further stabilizes the polycrystalline cluster [56].

The phenomenon of partial coalescence was observed in detail by Sato *et al.* with *in situ* electron microscopy of Ag and Au films on cleaved MgO and noted that for small nuclei, the fusion is complete but as the islands grow, a critical island height is reached at which complete coalescence is no longer possible, generating imperfect crystals attributed to elongated islands [58]. Yu *et al.* have formulated an interrupted coalescence model (ICM) where they introduce the critical island size R_c to Family and Meakin's model (FMM) [61] to incorporate the island-to-elongated-structure transition before percolation [59] as observed after Sato *et al.*'s work. In Family and Meakin's model, islands percolate and the final island radius is given by:

$$\mathsf{R}^{\mathsf{D}} = \mathsf{R}_1^{\mathsf{D}} + \mathsf{R}_2^{\mathsf{D}} \tag{2.4}$$

with $\mathsf{D} = 2$ for 2D circular islands and $\mathsf{D} = 3$ for spherical caps. For the ICM, where $\mathsf{R}_1 > \mathsf{R}_c$ & $\mathsf{R}_2 > \mathsf{R}_c$, no percolation occurs and the islands can be imagined as disks repulsing each other. In the initial growth stage, when $\mathsf{R} < \mathsf{R}_c$, a constant wiping of the surface due to smaller islands coalescing leaves clear surface gaps where smaller islands can nucleate. For each surface wiping, islands increase in size according to Eq. 2.4 and become less mobile which leaves gaps of a size comparable to the island radius in length. Eventually, only partial coalescence arises and little surface wiping reduces the available clean surface for new islands to nucleate. This transition has a considerable impact on the film's microstructure due to islands shifting from uniformly distributed spherical caps to elongated with low height/length ratio islands.

In essence, the coalescence process is driven by the reduction of surface energy as the final surface of two islands merging is lower. This can be easily deduced by finding the resulting radius for an island having a volume equivalent to the two islands combined as formulated in Eq. 2.4. In the case of two islands of identical radius R_0, the final radius is thus $\mathsf{R}_f = 2^{1/3}\mathsf{R}_0$. The surface area of a spherical cap Ω depends on the square of the radius, and it is found that the final surface area is reduced by a factor of $\frac{2\Omega_0}{\Omega_f} = 2^{1/3}$. Consequently, complete coalescence of islands should systematically be observed. However, that's not what experimental results show as the coalescence appears to be progressively inhibited when cluster size increases. José-Yacaman *et al.* provide an interesting explanation for this phenomenon by looking at the decrease of Helmholz's surface energy per unit area [62]. Indeed, the difference in surface with the constant volume for spherical caps can be expressed as such:

$$\Delta\Omega/V = \frac{\Omega_f - 2\Omega_0}{2 \times V_0} \tag{2.5}$$

$$= \frac{2\pi\mathsf{R}_0^2(2^{2/3} - 2)}{2 \times \frac{2\pi}{3}\mathsf{R}_0^3} \tag{2.6}$$

$$= \frac{-0.62}{\mathsf{R}_0} \tag{2.7}$$

The decrease of the surface area is accompanied by an energy releases in the form of heat [63]. This freed surface energy decreases proportionally with the radius of the merging islands which indicates that coalescence is more susceptible to be interrupted in a metastable state for bigger islands. Another effect reported by Yang *et al.* is the interaction between a cluster and the substrate surface that appears to increasingly hinder the coalescence process [64].

2.3.5 Thermal anneal and substrate's surface temperature

Metal-island films exhibit strong absorption in the visible due to their plasmonic properties (introduced in Section 2.4). The absorption is attributed to a resonant coupling of light with the free electrons of the metal-islands, generating an absorption peak. It is characterized by its position and full-width at half maximum (FWHM). The nanoparticles' (NPs) uniformity dictates the FWHM and tends to be broader for a larger size and shape distribution. Most studies, including the present one, aim at controlling both the peak position and FWHM. It was found that thermal annealing after deposition can be used to great extent to alter the film's microstructure [65]. Sun *et al.* were able to fine-tune the surface plasmon peak of a gold film on a quartz substrate to produce a plethora of colors ranging from greenish to yellowish-red as presented in Fig. 2.8. After about 200° C, the FWHM drastically decreases suggesting oblate to spherical islands transition [66].

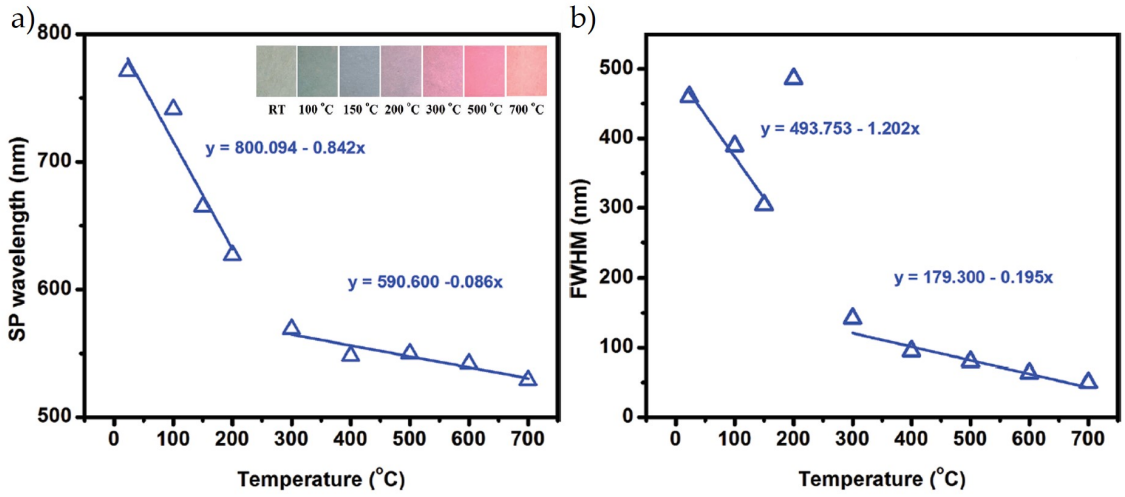

Figure 2.8 5 nm gold island film absorption maxima (a) position and (b) FWHM depending on the annealing temperature for 180 s treatment. Insert: optical images of the color associated with the spectra. Adapted with permission from Sun *et al.* [66].

Obviously, this thermal treatment was conducted *ex situ* and doesn't accurately depict the behavior of a growing film, but it highlights the diversity of the optical properties obtainable out of a 5 nm effective thickness gold film. One notable finding is the saturation of the island's aspect ratio at about 400° C from SEM & AFM measurements.

This study was conducted for a 5 nm gold film but the result will vary for different particle dimensions. Indeed, the melting temperature is found to have a size dependence, decreasing for smaller particles [67]. Asoro *et al.* have conducted a quick investigation of silver nanopar-

ticles melting temperature and discovered it to be in the range of $\sim 450-600$°C for particles of size going from 4 to 20 nm [68]. Silver has a slightly lower melting temperature than gold and it's foreseen that gold clusters will require higher temperatures to melt [69]. Moreover, during growth, contrarily to a deposited-then-annealed film, gold clusters increase in size and their sensitivity to lower temperatures is thus more significant in the early growth stage. As a result, it's expected that lower temperatures are required to induce an effect similar to the de-wetting from thermal annealing.

A direct comparison for a 5 nm film was not found with gold grown at various substrate temperatures. However, Venugopal *et al.* have witnessed a similar temperature dependence for a 1, 2, & 4 nm silver films with a FWHM minimum observed, respectively, at around 150, 200, & 300°C surface temperature during growth [25].

Loncaric *et al.* have compared 3 surface temperatures (25, 120, & 215°C) for e-beam gold and silver deposition for a 3 nm film [70,71]. Their results for Ag are consistent with Venugopal *et al.*, *i.e.* the 215°C temperature shows a minimal shift from 120°C. In comparison, Au's SPR peak goes from 640 nm at 25°C to 600 nm for 120°C, and finally to 585 nm at 215°C. Hence, the peak shift decreases and tends to reach a minimum value but at a higher temperature than silver.

In summary, both thermal annealing and higher surface temperature during deposition are found to significantly impact the optical properties of gold-island films. However, an *ex situ* thermal treatment is expected to require higher temperatures to reach a minimum in the FWHM peak since the particles are larger. Note that this assertion might be impacted with different thermal anneal durations.

2.3.6 Growth regimes

Schwartzkopf *et al.* have extensively studied the growth of gold on various surfaces which satisfy 3D growth thermodynamic conditions ($\Delta\gamma > 0$ as seen in section 2.3.1) [32,72,73] and have categorized the growth of a gold film on a dielectric into four growth regimes depicted in Figure 2.9.

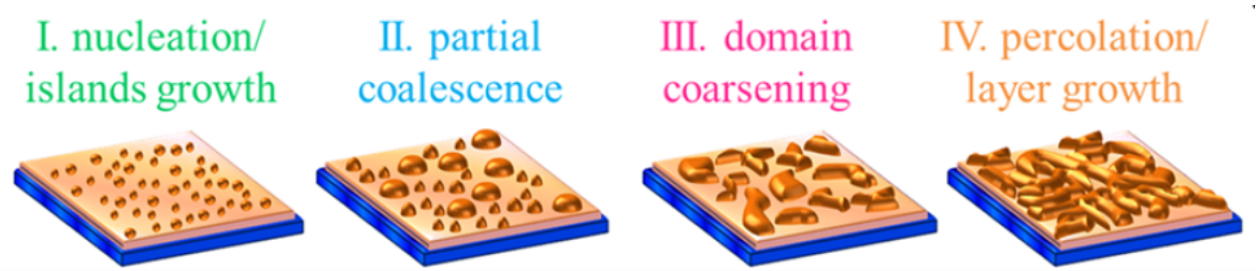

Figure 2.9 Illustration of the four growth regimes: nucleation and growth of isolated spherical islands (I), partial coalescence of hemispherical clusters (II), coarsening of branched domains of flat spheroids (III), and continuous layer growth after percolation (IV). The image taken with permission from Schwartzkopf *et al.* [72].

The first growth regime can be understood considering the simple kinematic model in section 2.3.2. Schwartzkopf *et al.* found that for a low atom flux, the island density increases before peaking but for higher deposition rates, it appears to immediately decrease. This result is best interpreted considering Eq. 2.1 for the case of a large adatom density n_1. In this situation, the term $n_1\tau_\alpha^{-1}$ cannot compete with the n_1^2. Hence, for a sufficiently high deposition rate, adatoms have practically no time to diffuse before they nucleate and so the adatom density is expected to collapse quasi-instantly. Meanwhile, the cluster density reaches right-away a peak and steadily decreases due to the island coalescence, coherent with Schwartzkopf *et al.*'s experimental data [32].

With increasing clusters size, the fusion process is gradually inhibited (sec. 2.3.4) and lateral island growth increases rapidly, marking the onset of the partial coalescence regime (II). Past this regime, the clusters' shape progressively loses any resemblance with spheroids which debuts the domain coarsening regime (III). Subsequent deposition increases the lateral size of the worm-like elongated clusters until the branched structures form a continuous network at the percolation threshold, *i.e.* the film becomes conductive and is filled with voids. The holes are gradually filled by the condensing atoms from the vapor until a continuous film is obtained (IV). The previous sections of this chapter have mainly focused on the early growth stages since past the regime II, islands form a branched domain and size or shape control is practically impossible.

In the context of metal-island film growth, the domain coarsening regime is not desirable for the previously cited applications necessitating NPs incorporation and having a means to rapidly identify the effective thickness threshold before its onset is of great interest. Since gold-island films exhibit strong localized surface plasmon resonance (LSPR), which depends

on the island size, shape & surrounding medium, the growth dynamics can be investigated exploiting this unique feature of plasmonic materials. In essence, the optical properties of the film are expected to reflect the underlying microstructure. Section 2.4 provides elaborated explanations on why this feature of plasmonic layers can be exploited to understand the growth kinetics of a discontinuous gold film.

2.3.7 Ion bombardment on metal-island films

Having seen the effect of thermal annealing and surface temperature on the film's nanostructure, one can wonder what other options are left to overcome the limitations of deposition at room temperature to sharpen the absorption peak for substrates which cannot withstand temperatures much higher than 100°C. For example, polycarbonate which is a very popular material due to its relatively low refractive index of 1.586, low Abbe value, high transparency, strength, and toughness but cannot sustain temperature much higher than 130°C [23].

Laser [74] and flash lamp [75] annealing come to mind as potential solutions but conventional deposition systems can't generate *in situ* surface treatments so that multiple composite layers of metallic nanoparticles would be difficult to produce without specialized equipment.

It was already demonstrated that sputtering is a lot more energetic than evaporation principally due to the constant bombardment of species on the substrate's surface during deposition. As reported, most atoms striking the substrate are neutral but some are ionized and typically more energetic than their neutral counterparts due to the plasma sheath accelerating them. Moreover, this kinetic energy transfer on the substrate's surface appears favorable to promote the diffusion of the atoms on the surface which was found to delay the partial coalescence regime onset and also to influence the size and density of the islands [76].

For instance, the application of a negative bias on the substrate can significantly increase the energy of the ions striking the surface. Controlling the bias voltage allows one to modify the film's microstructure, sputter physisorbed chamber gasses from the substrate's surface, resputter deposited atoms, promote adatom surface mobility, improve optical properties & more [38, 77].

The enhanced diffusion can be explained by the direct kinetic energy transfer from the ion to the atom during ion-atom collisions. The probability for an atom to diffuse on the surface is characterized by the diffusion constant $D = D_0 e^{-E_d/k_b T}$ and, so, the probability of diffusion P follows the proportional relationship $P \sim e^{-E_d/k_b T}$. For an ion of energy E_i, the probability for the atom to diffuse after a collision becomes $P \sim e^{-(E_d - E_i)/k_b T}$ [78]. Furthermore, the impinging particle not only generates local heating but can also become incorporated into

the growing film, modifying its properties in a way that cannot be reproduced simply by heating the surface [79].

Marinov *et al.* have found that the impact of ion bombardment (IB) of Ag affects even the early mechanism of growth from *in situ* electron microscopy diffraction pattern observations exhibiting a preferential $< 110 >$ orientation after IB. Furthermore, surface mobility was found to be significantly improved to the point that island nucleation was observed underneath a masked zone. Moreover, IB flux at later growth stages has also shown that a depletion zone around the larger nuclei increase of size the greater the ion flux [80].

A rise of surface temperature associated with the kinetic energy transfer of ions to the substrate is also expected which contributes to the formation of the islands (de-wetting) and Ostwald-ripening [81]. In addition, ion beam irradiation provides a controlled method to remove some material with the intent to better control the size distribution of a discontinuous island film. Paszti *et al.* have explored the idea and found that the size distribution could be improved by getting rid of the smaller islands upon IB irradiation [76]. However, the ion energy used in Paszti *et al.*'s study is of $1-2\ keV\ Ar^+$ which is quite high considering gold's sputter yield becomes linear for ion energies greater than 60 eV [82]. It is thus intriguing in the context of a surface modification study such high ion energies.

In summary, this method appears as a double-edged sword, both promoting island film growth and the formation of a thinner continuous film. The former is due to the added energy for the atoms to diffuse on the surface from the ballistic process but also because of the transferred kinetic energy that heats the surface. However, surface damage increases the number of defects and, hence, the island density increases which is known to favor early coalescence and percolation. This effect is amplified due to the resputtering of deposited material that diminishes the effective deposition rate and necessitates longer deposition times which further promotes surface defects.

Ion-assisted deposition (IAD) of 100 eV Ar^+ for evaporated gold films on silica was thoroughly investigated by Netterfield *et al.* with *in situ* transmittance, reflectance, and ellipsometry [83]. Increasing the ion energy reduces the coalescence thickness, a phenomenon explained by the surface damage induced by the ion bombardment, increasing the nucleation site density. Subsequent etching of the gold film after a continuous film formation showed a hysteresis in the film's optical properties from ellipsometry measurements as depicted in Fig. 2.10. Indeed, the thickness of the continuous film can be reduced significantly until the progressively thinner film becomes discontinuous once again. The authors attribute the morphology of the discontinuous film to the surface roughness which has a height feature of about 0.7 nm for this study, which is rather small compared to a film before percolation.

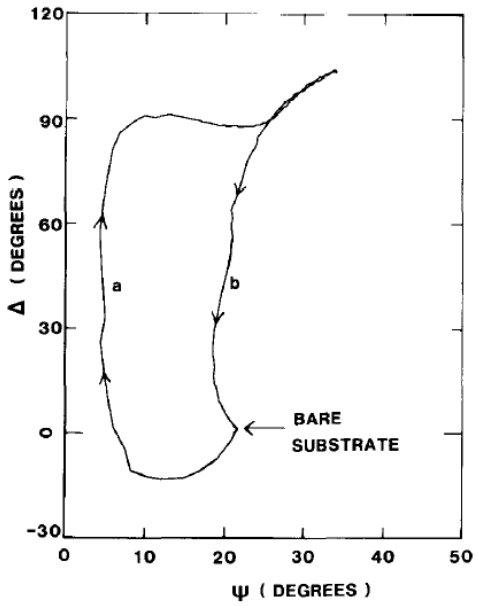

Figure 2.10 Ellipsometric angles Δ and Ψ during (a) deposition of gold film and (b) subsequent etching of the gold layer with 100 eV Ar^+ ion beam. Taken with permission from Netterfield *et al.* [83].

2.4 Plasmonic

In this section, the concept of local surface charge oscillations attributed to the resonant nature of metal-island film is defined. The dissimilar optical response of dielectric and metals is attributed to the free-electrons present in metals that are not subject to a restorative force when excited by an electric field. The Lorentz and Drude-Lorentz models are introduced to define the permittivity of insulators and conductors. These models allow to simply represent the optical behavior of matter in terms of electronic oscillations (or lack of in the Drude case). Furthermore, a composite material's electric permittivity can be described as a combination of the permittivity of its constituents.

The rest of the section is dedicated to the development of the necessary physical concepts and the introduction of the relevant literature to understand the underlying phenomena at the origin of the peculiar optical properties of a gold-island film. The choice of the surrounding medium along with the size and shape of the metallic inclusions in a host material all influence the line width and amplitude of the surface plasmon resonance.

Further on, one can view spherical nanoparticles as lossy nanoantennas which scatter but absorb electric field. The efficiency of the system to do so depends on the material used and how well far-field radiations are converted into local field energy. Finally, the chapter

ends on the particular structures which link the optical properties and the morphology of a gold-island film at the different growth stages.

2.4.1 Lorentz model

The Lorentz oscillator model describes the interaction of an electron with electric fields in the scope of classical mechanics. An applied electric field on a bound electron to the nucleus of an atom is akin to a mass-spring system and will behave according to Hooke's law.

From Newton's second law of motion:

$$\vec{F} = m_e \frac{d^2\vec{r}}{d^2t} \tag{2.8}$$

with $\vec{F}$ the force exerted on the electron, m_e the mass of the electron, and $\vec{r}$ the displacement. The electron's equation of motion can be expressed by considering all possible forces acting upon it:

$$m_e \frac{d^2\vec{r}}{d^2t} = F_{spring} + F_{damping} + F_{driving} \tag{2.9a}$$

$$m_e \frac{d^2\vec{r}}{d^2t} = -\mathtt{k}\vec{r} - \Gamma\frac{d\vec{r}}{dt} - e\vec{E} \tag{2.9b}$$

$$m_e\omega^2\vec{r} = -\mathtt{k}\vec{r} - i\omega\Gamma\vec{r} - e\vec{E} \tag{2.9c}$$

with $\vec{r}(t) = \vec{r}(\omega)e^{-i\omega t}$, Γ the damping factor, e the elementary charge, $\vec{E}$ the local field, $\mathtt{k}$ the spring constant due to the restoring Colombian force. The first term of Eq. 2.9 is the restoring force from the positive ionic core, the second the damping of the motion due to scattering events and the last term generates the driving force due to the electric field which can be written as $\vec{E}(t) = \vec{E}(\omega)e^{-i\omega t}$. The model assumes that the electron's displacement oscillates at the same frequency as the applied electric field.

This yields:

$$\vec{r} = \frac{e\vec{E}}{m_e\omega^2 + i\omega\Gamma - \mathtt{k}} \tag{2.10}$$

With substitution of $\zeta = \Gamma/m_e$, the damping ratio, and $\omega_0 = \sqrt{\mathtt{k}/m_e}$, where ω_0 is the resonant

frequency, one finds:

$$\vec{r} = \frac{e\vec{E}/m_e}{\omega^2 + i\omega\zeta - \omega_0^2} \tag{2.11}$$

If the dipole moment associated with each atoms is $\vec{p} = -e\vec{r}$, then the polarization density of the material as a whole (containing N_e electrons) can be expressed as:

$$\vec{P} = -N_e e\vec{r} \tag{2.12}$$

For a linear, homogeneous and isotropic material, the polarization vector $\vec{P}$, which represents the density of dipole moments induced as a result of the application of an electric field, can be expressed as follows [84]:

$$\vec{P}(\omega) = \varepsilon_0 \chi(\omega)\vec{E}(\omega) \tag{2.13}$$

where ϵ_0 is the free-space permittivity and $\chi(\omega)$ is the electric susceptibility for a dispersive media (frequency dependency).

The electric permittivity is defined as:

$$\varepsilon(\omega) = \varepsilon_0(1 + \chi(\omega)) \tag{2.14}$$

One obtains by combining Eq. 2.11 and 2.12:

$$\vec{P}(\omega) = \frac{-N_e e^2 \vec{E}_0/m_e}{\omega^2 + i\omega\zeta - \omega_0^2} \tag{2.15}$$

Inserting Eq. 2.13 and 2.14 into Eq. 2.15 renders:

$$\varepsilon(\omega) = 1 - \frac{N_e e^2/m_e}{\epsilon_0(\omega^2 + i\omega\zeta - \omega_0^2)} \tag{2.16}$$

Which is more often expressed as follow:

$$\varepsilon(\omega) = 1 - \frac{\omega_p^2}{\omega^2 + i\omega\zeta - \omega_0^2} \tag{2.17}$$

with $\omega_p = \sqrt{\frac{N_e e^2}{\varepsilon_0 m_e}}$, the plasma frequency.

Since the permittivity depends on the frequency, the media is said to be dispersive. In other words, the material's optical properties are wavelength-dependent. This attribute is at the

origin of the color refraction observed when white light is shone through a prism.

Fig. 2.11 shows the optical behavior for a resonant media (presence of restoring force). Three regimes are observed corresponding to low-, medium- and high-frequencies. In the low-frequency region $\omega << \omega_0$, the displacement is not maximal and in phase with the electric field. The medium-frequency region $\omega \approx \omega_0$ the amplitude of displacement is much larger and it is out of phase by $\pi/2$ with the electric field. This zone is the most absorbing, followed by the low-frequency one. At high frequency $\omega >> \omega_0$, the electrons cannot follow the applied force and their displacement tends to zero. The material's polarization is out of phase by π in this region.

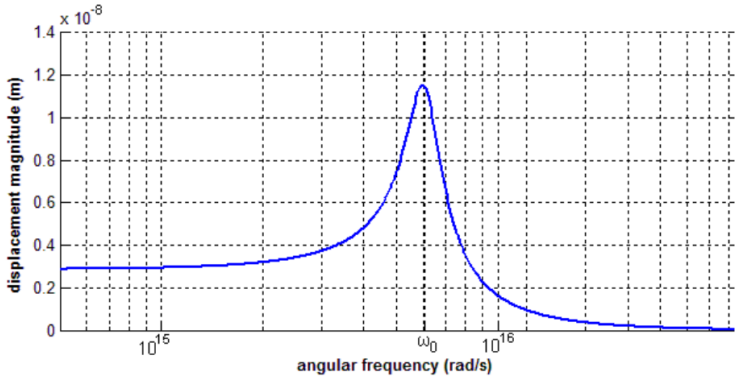

(a) Magnitude of the displacement $\Re\{\vec{P}\}$.

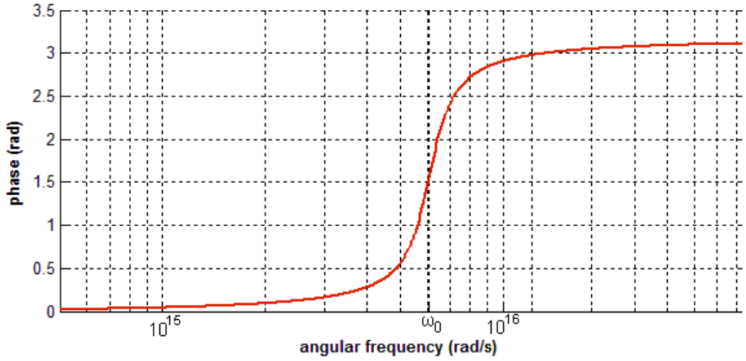

(b) Phase relative to the applied electric field $\Im\{\vec{P}\}$.

Figure 2.11 The magnitude of displacement and phase were obtained with the numerical application of the following values: $N_e = 10^{28}$ cm^{-3}, $\omega_p = 1.3 \times 10^{16}$ rad/s, $\omega_0 = 6.077 \times 10^{15}$ rad/s and $\zeta = 1.519 \times 10^{15}$ rad/s. Taken with permission from Almog *et al.* [85].

2.4.2 Drude-Lorentz model

Metals are known for their electrical conductivity which is due to the presence of free electrons, unbound to nuclei. This attribute is analogous to a restoring force of zero in the

Lorentz model, *i.e.* $F_{spring} = 0$ that effectively yields $w_0 = 0$ and the permittivity becomes:

$$\varepsilon(\omega) = 1 - \frac{\omega_p^2}{\omega^2 + i\omega\zeta} \tag{2.18}$$

known as the Drude-Lorentz model.

When $\omega < \omega_p$, the dielectric function is negative and there's no propagation in the metal whereas for $\omega > \omega_p$, the metal becomes transparent. For the former regime, Eq. 2.18 provides a simple approximation of a metal's dielectric function, although it's far more complex in reality. Indeed, to this dielectric function dubbed the Drude term, other contributions from phonon and interband transitions, for example, contribute to the dielectric function of metals [10, 55].

The metallic dielectric function is thus often expressed $\varepsilon = \varepsilon_1 + i\varepsilon_2$ for which

$$\varepsilon_1(\omega) = \varepsilon_\infty - \frac{\omega_p^2}{\omega^2 + 1/\zeta^2} \tag{2.19a}$$

$$\varepsilon_2(\omega) = \frac{\omega_p^2/\zeta}{\omega(\omega^2 + 1/\zeta^2)} \tag{2.19b}$$

where ε_∞ is the long-wavelength dielectric constant attributed to interband transitions. The plasma frequency can be understood at a frequency for which $\varepsilon = 0$, light is neither reflected nor transmitted [86]. At this frequency, electrons support a collective oscillation, known as plasma oscillation or plasmon, a quasi-particle, corresponding to a quantum of plasma energy ($\hbar\omega$) at $\omega = \omega_p$ [10] for the bulk plasma wavelength.

2.4.3 Effective medium approximation

Solving the Maxwell's equations for nanoscopic structures to obtain macroscopic properties such as the transmission requires incommensurate computational resources that renders this approach prohibitive. Finite-difference time-domain (FDTD) method computes the propagation of an EM field in a discrete space-time where the evolution of the electrical and magnetic fields, expressed as finite-difference, are solved in a leapfrog manner [87]. Such method has been used to simulate 200×200 nm^2 area of gold-island films with good precision [88] but remains limited to simulation size comparable to the wavelength of light due to hardware limitations [87].

Effective medium approximation (EMA) allows one to model the macroscopic optical properties of a composite material. The principle resides in describing an effective dielectric

constant as a function of the dielectric constants of the constituents of a composite material. Furthermore, this approach is considerably easier to compute.

A well known EMA model derived by Maxwell-Garnett (MG) [89] from the Clausius and Mosotti theory allows to explain color changes for discontinuous noble-metal films. The MG effective dielectric function ε_{eff}^{MG} is defined as:

$$\frac{\varepsilon_{eff}^{MG} - \varepsilon_h}{\varepsilon_{eff}^{MG} + g\varepsilon_h} = f\frac{\varepsilon_m - \varepsilon_h}{\varepsilon_m + g\varepsilon_h} \tag{2.20}$$

where ε_h is the dielectric function of the host matrix, ε_m the metallic spherical inclusion (see: Fig. 2.12b), f the filling factor and g the depolarization factor that depends on the shape of the inclusion (equal to 2 for spherical particles). Typically, $1 = g_x + g_y + g_z$ and $g_x = g_y$ because the models are restricted to ellipsoidal particles. For $g_z = 0$, the particle is flat, *i.e.* a thin film whereas for $g_z = 1$, the inclusions are needle-like [90].

Another EMA proposed by Bruggeman [91] (Fig. 2.12a) describes the effective dielectric constant of randomly distributed inclusions in a matrix. The Bruggeman effective dielectric constant is obtained according to:

$$f\frac{\varepsilon_m - \varepsilon_{eff}^{BM}}{\varepsilon_m + g\varepsilon_{eff}^{BM}} + (1-f)\frac{\varepsilon_h - \varepsilon_{eff}^{BM}}{\varepsilon_h + g\varepsilon_{eff}^{BM}} = 0 \tag{2.21}$$

For a small filling factor f, both models yield equivalent effective dielectric function values [92]. However, Bruggerman's model is more representative of sputtered metal-island films at higher filling factors when the islands coalescence. Maxwell-Garnett offers a simplistic view of the effect of the size, shape and surrounding medium's refractive index. Xu *et al.* [93, 94] studied the impact of modifying the surrounding refractive index which is found to redshift the absorption peak for increased refractive index values. Furthermore, increasing the equivalent film thickness also shifts the LSPR peak toward longer wavelengths.

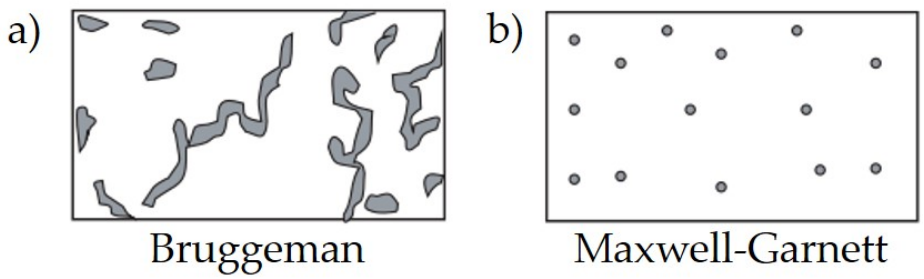

Figure 2.12 Two effective medium approximation models : (a) Bruggeman model which calculates the effective dielectric function of a random mixture of two materials, and (b) the Maxwell-Garnett model valid for small inclusions in a matrix. Taken with permission from Mandal *et al.* [95].

The MG model supposes an interparticle distance sufficiently large so that no interaction arises from the dipolar coupling. A plethora of models has emerged to extend the applicability of this model to accommodate a higher filling factors [96]. However, since the fitting of the experimental data is done via a software that does not support more complex models (as of now), the applicability of the EMA will be restricted to the two presented models.

2.4.4 Localized Surface Plasmon

Despite no mention of plasmonic, Gustav Mie's article published in 1908 is one of the most cited references in the plasmonic literature [5]. Indeed, Mie's theory allowed to find analytic solution to Maxwell's equations for the case of small particles with arbitrary refractive indexes and radii. Surface plasmons were defined in 1957 by Ritchie as a plasma mode along the interface of a metal and dielectric medium, propagating in the form of a charge density wave [97]. This plasmon is called surface plasmon polariton (SPP) due to the presence of an EM wave (photon) which arises from the propagation of the charge density wave as depicted in Fig. 2.13. Since this SPP is a propagating wave, light's wavevector must match that of the SPP which is only possible for light incident from a higher refractive index medium than that of the dielectric at which the SPP propagates along the metal interface [98]. However, this unlikely condition can be generated by utilizing an attenuated total reflection (ATR) set-up. For example, a thin metal film deposited on a dielectric, such as glass, can support SPP. Indeed, when light illuminates the metal/glass interface at an angle that meets the condition for total reflection, part of the light will "propagate" in the form of an evanescent wave inside the metal film with a wavevector high enough to excite a SPP at the metal/air interface (because $n_{glass} > n_{air}$). This evanescent wave decays very rapidly and the metal film's

thickness is a critical parameter so that the evanescent wave is not completely attenuated at the air/metal interface.

In the case of a metallic nanoparticle that is smaller than the wavelength of the radiation, due to the confinement of the electrons inside the particle, the charge density oscillation is confined and doesn't propagate, a phenomenon called localized surface plasmon (LSP). The momentum provision $\Delta \mathsf{p}$ of a nanoparticle of radius r can be approximated as $\Delta \mathsf{p} = j\frac{2\pi}{\mathsf{r}}$ with j an integer [99]. LSPs support multiple discrete modes and their excitation doesn't depend on the irradiating light's angle. For spheroid particles, modifying the size and their shape will induce very different LSP signatures that can be tuned to obtain a plasmonic absorption at the desired wavelength [10]. These modes are called localized surface plasmon resonance (LSPR) and give rise to strong coupling between light and surface charge density oscillations. In summary, despite being similar in nature, SPP and LSP are very different as illustrated by Fig. 2.13.

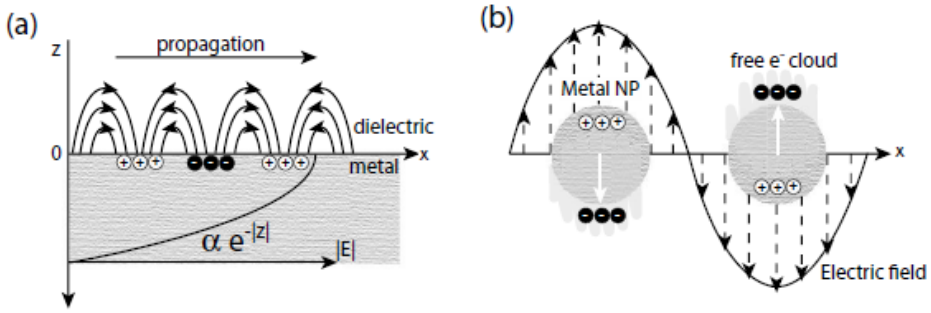

Figure 2.13 The schematic depicts (a) the case of a SPP propagating along a dielectric/metal interface with the decaying electric field in the metal away from the interface and (b) oscillations of the electronic cloud inside metal nanoparticles excited by an electric field. Taken with permission from F. Todescato [10].

2.4.5 Spherical nanoparticles

In essence, spherical nanoparticles convert far-field radiation into the near-field and inversely [100], a behavior attributed to a nano-antenna. The absorbed I_{abs} and scattered I_{scat} power can be related to the scattering cross-section $C_{scat} = \frac{I_{scat}}{I_{inc}}$ and absorption cross-section $C_{abs} = \frac{I_{abs}}{I_{inc}}$. Due to the size smaller than the wavelength of light, the retardation effects can be ignored and both cross-sections can be expressed as [101]:

$$C_{scat} = \frac{k^4}{6\pi}|4\pi\varepsilon_0 a^3 \frac{\varepsilon_{sph} - \varepsilon_{med}}{\varepsilon_{sph} + 2\varepsilon_{med}}|^2 \propto a^6/\lambda^4 \tag{2.22a}$$

$$C_{abs} = k\Im\{4\pi\varepsilon_0 a^3 \frac{\varepsilon_{sph} - \varepsilon_{med}}{\varepsilon_{sph} + 2\varepsilon_{med}}\} \propto a^3/\lambda \tag{2.22b}$$

for $k = \omega/\lambda$ and a the radius of the spherical NP.

Eq. 2.22 highlights the rapid rise of the scattered field (energy sent back to the far-field) in contrast to the absorbed power (dissipated within the particle). The resonance frequency ω_{SPR} appears at the $\varepsilon_{sph} + 2\varepsilon_{med} = 0$ and is $\omega_{SPR} = \frac{\omega_p}{\sqrt{3}}$ for $\varepsilon_{med} = 1$.

As seen from the previous section, the electron density of the inclusions is directly correlated with the plasma frequency from which the surface plasmon resonance ω_{SPR} frequency is derived. Another factor is the surrounding effective refractive index which can greatly shift the resonance as demonstrated in Fig. 2.14. This result can be understood by considering again that the resonance condition of a spherical particle is met for $\varepsilon_{sph} = -2\varepsilon_{med}$, and so $\varepsilon(\omega_{SPR}) = \frac{\omega_p}{\sqrt{1+2\varepsilon_{med}}}$ which increases for a higher refractive index.

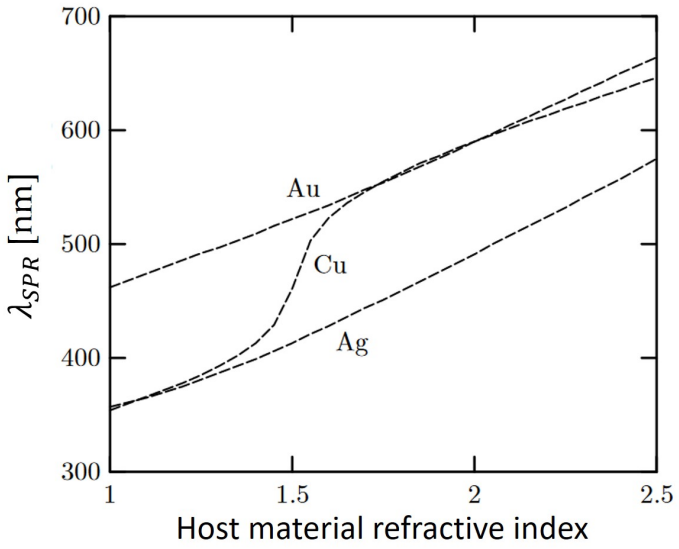

Figure 2.14 Wavelength where the absorption is maximum for the three coinage metals (Ag, Au and Cu) depending on the matrix dielectric constant n_m which redshifts for increasing n_m. Adapted with permission from J.M. Lamarre [102].

Absorption peak positions between Au and Ag can be achieved by varying the ratio between the two (and any other miscible elements) [103]. Indeed, Roy *et al.* have found a linear

dependence between the concentration of Ag and Au in the alloy and the respective absorption peak of the pure metals ($\sim$ 400 nm and 500 nm, respectively).

2.4.6 Plasmonic materials

Not every material has the same plasmonic performance and despite silver exhibiting the best performance, it falls short when it comes to environmental stability. Gold is thus often the material of choice for applications in more demanding environments with good plasmonic performance (see Fig. 2.15). The quality factor $Q = \frac{E_{loc}}{E_0}$ is defined as the local-field enhancement capability of a resonator, that is how much the incident field is amplified in contrast to the local field [104]. The quality factors for both LSPR and SPP are shown in Fig. 2.15 and explain why metals like silver and gold with negative ε' and small ε'' are popular plasmonic materials.

In Fig. 2.15, aside from Ag and Au, few elements can be practically used. Indeed, aluminum typically grows as layer-by-layer and other suggested materials are too reactive (sodium and potassium for instance) which prohibit their implementation. Due to the prohibitive cost of noble metals, alternatives have been explored like titanium nitride with a field enhancement comparable to gold but at a much lesser price [105]. However, like other options such as aluminum, novel methods are required to obtain NPs as their growth mode is 2D [106].

Material	LSPR & SPR		SPP		TO Devices	Superlens	Comments
	Maximum Q_{LSPR} (λ)	Q_{LSPR} (1.5 µm)	Maximum Q_{SPP} (λ)	Q_{SPP} (1.5 µm)	Q_{TO} (λ)	Q_{S} (λ)	
Ag*	392 (1.08 µm)	39.3	23413 (1.08 µm)	4530	1.82 (326 nm)	0.3 (339 nm)	Good for LSPR & SPP
Au*	16.66 (0.89 µm)	10.63	1410 (1.94 µm)	1140	0.29 (207 nm)	−0.13 (252 nm)	Good for LSPR
Al	13.56 (0.113 µm)	5.55	2677 (2.5 µm)	1315	26.32 (82 nm)	0.52 (114 nm)	Good for LSPR in UV
Na*	37.8 (1.00 µm)	27.3	1889 (2.25 µm)	1179	NA***	0.48 (312 nm)	Difficult to process
K*	40.6 (1.17 µm)	19.2	1287 (2.25 µm)	419	22.22 (326 nm)	0.5 (438 nm)	Difficult to Process
KAu	1.3 (2.5 µm)	NA**	1.1 (2.5 µm)	NA**	1.72 (2.38 µm)	0.18 (2.52 µm)	Difficult to process
ITO*	2.72 (2.3 µm)	NA**	16 (2.3 µm)	NA**	1.54 (1.69 µm)	0.13 (1.88 µm)	Good for TO in NIR

Figure 2.15 Tabulated values of the various quality factors associated with different plasmonic candidate materials. The $Q_{LSPR} = -\varepsilon'(\omega)/\varepsilon''(\omega)$ differs from the $Q_{SPP} = \varepsilon_m'^2(\omega)/\varepsilon_m''(\omega)$ due to the possibility to tune the resonance of the LSPR peak with the geometry of the nanoparticle with ε_m the permittivity of the bulk metal. Adapted with permission from West *et al.* [107].

As a consequence, gold has emerged as the material of choice to study the LSPR even despite its weaker enhancement factor in comparison to silver. Non-radiative processes are at the origin of the losses due to the excitation of LSPR and can lead to the decay of the surface plasmon [108]. Indeed, poorer performance of both gold and copper is attributed to the LSPR peak overlapping interband transitions, hindering the plasmonic performance [109,110]. This damping broadens the absorption peak which is detrimental to many applications. Note that the resonance peak can be adjusted with the shape of the NP to not overlap the interband transition, a strategy that can palliate this inherent weakness of gold. Indeed, a recent study found that gold nanorods didn't suffer from this drawback [110] but the fabrication of nanorods via PVD is a significant challenge.

2.4.7 Evolution of the optical properties of metal-island films

The following section offers a detailed explanation of the origin of changes in optical behavior throughout the growth of the film which is attributed to the presence of unique resonating structures for each growth stage.

In a simulation study of nanobars (NBs) and nanoparticle chains (NPCs), the effect of the junction between the nanoparticles was found to generate a transmission dip comparable to that of a much longer NB [30]. Indeed, the resonance of a NPC is directly related to its length and the longer it is, the further its peak is red-shifted as demonstrated in Fig. 2.16. This effect is of particular interest considering the tendency of islands to partially percolate which generates a neck at the junction between the islands, akin to NPCs. Moreover, this property shows how diverse the resonance wavelength can be depending on the shape of the clusters and could, technically, be adjusted to any wanted value [111].

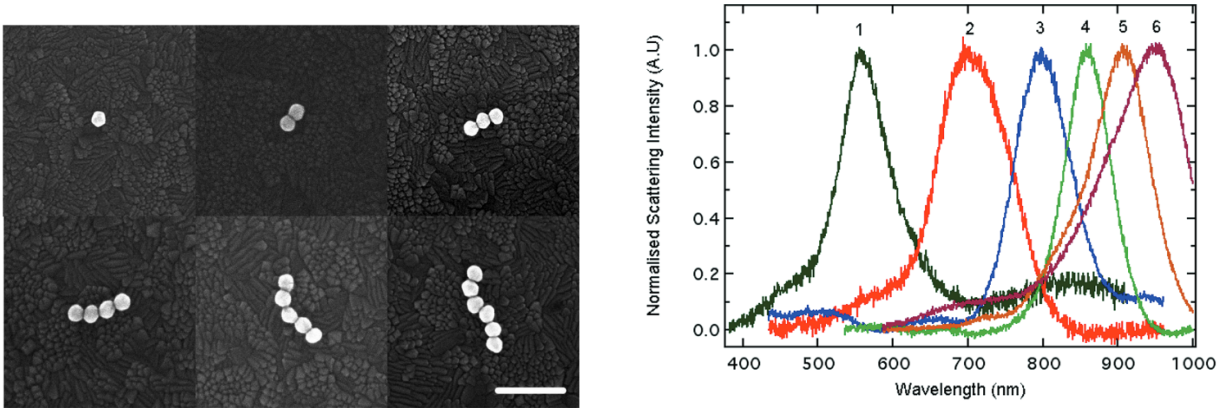

(a) SEM images of NPC on ITO. Particle size is 64 nm. Scale bar = 250 nm.

(b) Normalized spectra of the NPC labeled according to the associated chain length.

Figure 2.16 Experimental characterization of NPCs. Taken with permission from Barrow *et al.* [112].

The resonance peak can also be affected by the presence of the surrounding NPs due to inter-particle coupling. Atay *et al.* generated arrays of particle pair with a variable gap in-between and demonstrated that the inter-particle coupling allowed higher-order resonance modes to be excited [113]. Furthermore, the strength of the interaction is inversely proportional to the particles' distance. Higher modes only decay non-radiatively which is translated by increased absorption arising from the NPs dipolar coupling [114].

Additionally, the decrease of the gap distance between two NPs is accompanied by a red-shift as depicted in Fig. 2.17a. As the NPs overlap a similar behavior, shown in Fig. 2.17b, is also observed along with the apparition of a second peak attributed to the quadrupole resonance mode. Furthermore, the line width of the resonance peak is much broader for the overlapping particles, indicating a larger damping of the electronic oscillations.

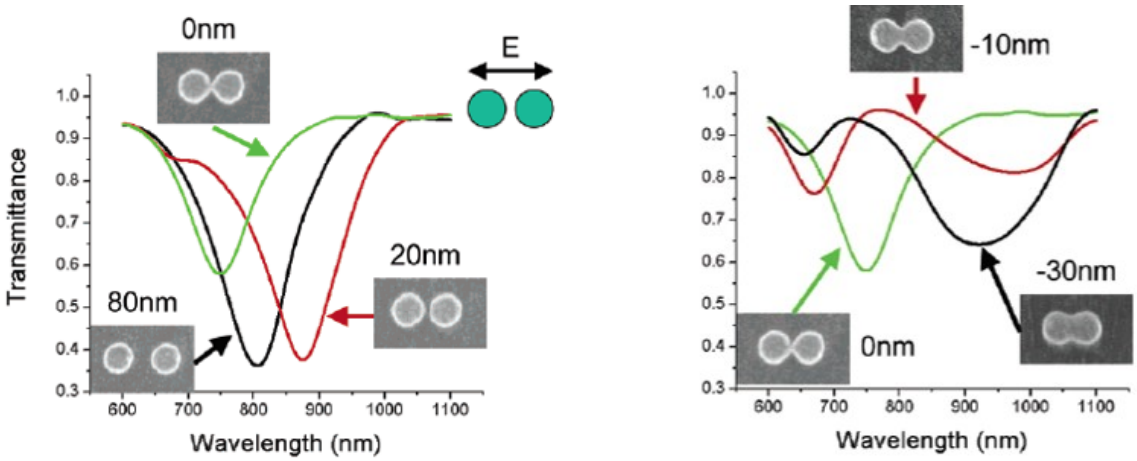

(a) Transmittance spectra of decreasing inter-particle gap distance.

(b) Transmittance spectra of particles increasingly overlapping.

Figure 2.17 Polarized transmission spectra (along the long axis of the NPs) of a 800×400 nm periodic lattice array of nanoparticle pairs. Taken with permission from Atay *et al.* [113].

Lastly, for large particles ~ 50 nm, multipole contributions and surface effects are dependent on the particle's size, causing a broadening of the absorption peak for increasing particle distance [115]. It was also found that the size influences the effective refractive index as the environment around the particle over a distance comparable to the particle's radius affects the resonance frequency [116].

A mode splitting is observed for elongated clusters since the resonance wavelength of the larger axis is significantly longer [117]. Around the percolation threshold, a special nanostructure is formed where isolated islands are surrounded by a conductive network. The formation of this structure is associated with an anomalous absorption band in the NIR [118]. Smith and Earp have modeled such structures as a ring of insulating material in a conductive medium and discovered that for an increasingly larger core, the resonant frequency was red-shifted.

At percolation, the film exhibits a Drude-like component characterized by a rapid gain in reflectivity in the IR for gold on silica [119]. Additionally, the authors have compared their experimental data to the Bruggeman EMA model and have found strong deviations at high frequencies and an overestimated conductivity. Worst, the plasmon peak is neither correctly positioned nor the amplitude properly reproduced.

CHAPTER 3 EXPERIMENTAL METHODOLOGY

This section presents the experimental methodology used to produce and characterize the studied samples. First, the sputter system is presented with all of its components and and parameters is presented. The optical apparatus used for *in-situ* surface reflectance spectroscopy is explained in more detail in the subsequent section which focuses on the optical characterization of the samples. Finally, the surface imaging methodology is described.

3.1 Experimental apparatus

3.1.1 Deposition chamber

Depositions were performed inside an in-house sputter process chamber presented in Fig. 3.1. The chamber configuration is of a "sputter-up" type with four magnetrons heads oriented upward toward the substrate holder (schematic of the sample arrangement presented in Fig. A.1). The targets' diameter was 2" (5.08 cm). RF and DC power supplies can be used to power the magnetrons. In the present context, just one RF power supply was available so all depositions were performed with the same RF generator. Another RF generator is connected to the substrate holder and used for biasing either as a deposition surface pre-treatment. Argon and oxygen are controlled by MKS mass flow controllers. The films' thickness is measured with a quartz crystal microbalance (QCM) inside of the system. A shutter masks the crystal when other films than gold is being deposited.

The chamber has multiple view-ports to allow for an optical system to be used during deposition. Two view-ports can be used as a reflection set-up with an angle of 65°. A resistive heating element allows one to reach temperatures of up to 200° C on the sample's surface. The substrate holder can rotate to increase uniformity of the deposition but, in the context of this study, had limited use.

The base pressure was typically at 2×10^{-6} $Torr$ using a turbo-molecular-pump. Without a load-lock, the chamber was systematically exposed to the atmosphere and a minimal pumping time of 3 hours was necessary to reach a base pressure $< 5 \times 10^{-6}$ $torr$. A butterfly valve allowed one to control the chamber's pressure upon gas insertion.

A ZnSe IR-transparent window installed on the bottom of the deposition system allowed for a reading of the substrate temperature using an infrared camera. In order to ensure a proper temperature reading with the camera, a thermocouple was used to validate the parameters suggested by the manufacturer (emissivity of the substrate's surface and background con-

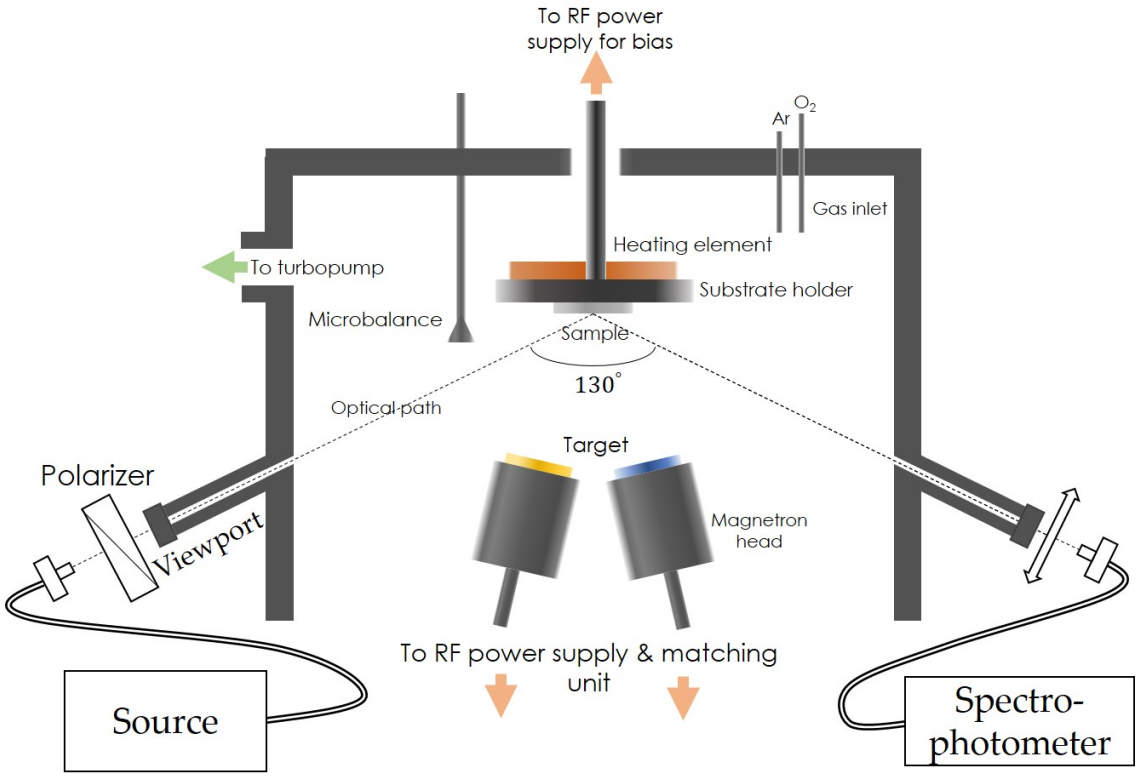

Figure 3.1 Schematic of the sputtering deposition system used for the deposition of all the samples.

tribution). Since the samples were relatively small, the thermocouple was not used during deposition to prevent it from masking the surface.

3.1.2 Deposition conditions

The choice of plasmonic material was mainly restrained to the noble metals gold and silver due to their interesting plasmonic properties (presented in Section 2.4). It is known that mid to late transition metals as solids do not wet oxides in the absence of kinetic constraints [44]. Furthermore, gold was tested on Al_2O_3, TiO_2 and SiO_2, three commonly used dielectric materials, and showed a 3D growth mode [120–122]. Gold is the noblest transition element and its low reactivity virtually immunize it from oxidization, an attribute that simplifies the study and characterization of the optical properties which are affected by many parameters, *i.e.* the size, shape, surrounding medium, and inter-particle coupling as detailed in Sec. 2.4.6.

The gold films were deposited by radiofrequency (RF) magnetron sputtering from a 5 cm gold target (99.99%) in an Ar (99.999%) atmosphere at a pressure of 6 mTorr and a power of 25 W (deposition rate of about 0.4 $Å/s$, verified for each experiment).

The substrates, 5×5 cm borosilicate glass, were ultrasonically cleaned using an alkaline solution, then bathed in isopropanol, rinsed with distilled water, and finally dried with nitrogen. Before deposition, the surface was exposed to a plasma of argon/oxygen mixture (2:1 flow ratio) with an RF-bias of $-100\ V$ for 5 minutes.

For most experiments, a SiO_2 passivating underlayer was deposited in an argon and oxygen (99.999%) containing atmosphere (5:1 flow ratio) at a pressure of 5 mtorr (0.21 Å/s) from a SiO_2 target (99.995%) at 150 W of RF power. Alumina was deposited (2.9 nm/min) via reactive sputtering from an aluminum (99.99%) target. The target was conditioned for 5 mins using an argon flow of 25 sccm (partial pressure of 3.6 mtorr) at a constant power of 150 W resulting in a self-bias voltage of 350 V. A 2 sccm flow of oxygen was subsequently introduced and the shutter kept closed for 2 mins which was determined to be long enough for the self-bias value to stabilizes at 331 V. The butterfly valve was kept open and the total pressure was 3.75 mtorr upon oxygen insertion. Akin to alumina, titania was deposited (2.4 nm/min) from a titanium (99.99%) target via reactive sputtering. The pre-sputtering of the target during 5 mins with a 25 sccm Ar flow stabilized to a 205 V self-bias value at a constant power of 150 W. The oxygen flow of 2 sccm resulted in a total pressure of 3.75 mtorr and a self-bias of 220 V after 2 mins.

3.2 Optical characterization

The optical behavior of metal-island films can reveal information on the underlying nanostructure. Indeed, the presence of LSPR is a key indicator that the film is still discontinuous but the amplitude and bandwidth of the peak disclose information about the size and shape distribution of the islands. Consequently, the characterization of the film in reflection and transmission is of utmost necessity to understand the impact of growth on the thin film's microstructure. The following sub-section describes the optical methodology used to characterize the metal-island films, but also all of the other films deposited such as silica, titania and alumina.

3.2.1 Ellipsometry

The deposition rate during sputtering was obtained using a Drude-Lorentz model with the ellipsometric measurements. The working principle of ellipsometry resides in the detection of the change of state in polarization of light upon reflection or transmission. A non-polarized beam of light can be separated into two components: one perpendicular (s-polarization) and one parallel (p-polarization) with the optical plane. The ellipsometric parameters, Ψ and Δ,

are expressed using the ratio of s- and p-polarization intensity (r_s and r_p respectively) from the following equation:

$$\rho = -\frac{r_p}{r_s} = \tan\Psi e^{i\Delta} \tag{3.1}$$

Ψ is directly related to the amplitude ratio of both polarizations and Δ their phase difference [123]. The ellipsometric measurements were conducted using a J.A. Woollam $RC2-XI$ ellipsometer and analyzed with the *CompleteEase* software to extract either the refractive index of the film or determine its thickness and other parameters such as the roughness/porosity. This ellipsometer is equipped with a xenon lamp allowing to probe the material's optical behavior from 200 nm to 2500 nm. Since the measurement is based on a ratio of the two polarizations, it is less sensitive to source intensity fluctuation.

3.2.2 Spectrophotometry

Near-normal (6°) reflectance R and normal transmittance T were measured by a universal measurement accessory (UMA) is installed on a *Cary 7000* UV-Vis-NIR Universal Measurement Spectrophotometer (UMS) from Agilent. Tungsten and deuterium lamps provide a wavelength range of $250-2500$ nm with a wavelength accuracy of ± 0.08 nm @ $190-900$ nm & ± 0.4 nm @ $760-3300$ nm. The dual-beam spectrophotometer allows comparing the measured intensity from a reference beam intensity to prevent skewed data from an unstable light source or even the detectors. The UV-Vis detector is a $R928$ PMT and the NIR detector is a cooled PbS photodetector.

The reflection R and transmission T were obtained from sample angle measurements of 6° and 65°. The extinction Ext is obtained from the relation:

$$Ext = A + S = 1 - R - T \tag{3.2}$$

with A the absorption and S the scattering. The latter term is often neglected. Although, metal-island films are known to scatter and this assumption is not valid. For oblique angle reflection measurements, the backside of the sample was covered with tape or sandblasted to prevent any backside reflection.

3.2.3 Colorimetry

In 1675, Newton published his discovery that white light could be decomposed into multiple colors and *vice-versa*. The perception of color has been a fundamental tool in physics and

chemistry, giving rise to spectrum analysis that fueled the discovery of new elements for which specific color emission bands were observed. It was found that the perception of white light could be produced from the addition of three primary colors: red, green and blue. This attribute is due to the underlying working principle of the human eye that relies on three types of cones with variable sensitivity to different wavelengths from 380 to 780 nm. Moreover, the cones' spectral sensitivity overlap and a single wavelength can excite all of them. Thus a color can be expressed by a tristimulus value and represented by the simple addition of three primary colors [124]. The same tristimulus values can be obtained from different spectra, a phenomenon called metamerism.

The concept of color perception was a hotly debated topic following Newton's work as color perception depends on the source of light & the observer. For this reason, the *Commission Internationale de l'Éclairage* (CIE) defined color spaces in 1931 with standardized colorimetric specifications for controlled light sources I_λ and standard photometric observers represented by x_λ, y_λ, and z_λ color-matching functions.

To obtain the color from spectral data, one must compute the tristimulus values XYZ from the spectral reflectance (or transmittance) distribution of the sample $\mathsf{S}(\lambda)$ multiplied by the reference illuminant's $\mathsf{I}(\lambda)$ spectral power distribution and the CIE 1931 color matching function for a 2° observer as follows [125]:

$$\begin{gathered}\mathsf{X} = \frac{1}{\mathsf{N}}\sum_i \bar{\mathsf{x}}_\mathsf{i}\mathsf{S}_\mathsf{i}\mathsf{I}_\mathsf{i}\Delta\lambda,\ \mathsf{Y} = \frac{1}{\mathsf{N}}\sum_i \bar{\mathsf{y}}_\mathsf{i}\mathsf{S}_\mathsf{i}\mathsf{I}_\mathsf{i}\Delta\lambda,\ \text{and}\ \mathsf{Z} = \frac{1}{\mathsf{N}}\sum_i \bar{\mathsf{z}}_\mathsf{i}\mathsf{S}_\mathsf{i}\mathsf{I}_\mathsf{i}\Delta\lambda \\ \mathsf{N} = \sum_i \bar{\mathsf{y}}\mathsf{I}_\mathsf{i}\Delta\lambda\end{gathered} \tag{3.3}$$

From the XYZ color coordinates, the conversion to RGB is done by applying a transformation matrix for a D65 illuminant as:

$$\begin{bmatrix}\mathsf{R}\\ \mathsf{G}\\ \mathsf{B}\end{bmatrix} = \begin{bmatrix}3.2404542 & -1.5371385 & -0.4985314\\ -0.9692660 & 1.8760108 & 0.0415560\\ 0.0556434 & -0.2040259 & 1.0572252\end{bmatrix}\begin{bmatrix}\mathsf{X}\\ \mathsf{Y}\\ \mathsf{Z}\end{bmatrix} \tag{3.4}$$

The $CIE\ L^*a^*b^*$ color parameters are defined as:

$$\begin{aligned}L^* &= 116f_y - 16\\ a^* &= 500(f_x - f_y)\\ b^* &= 200(f_y - f_z)\end{aligned} \tag{3.5}$$

where

$$
\begin{aligned}
f_x &= \begin{cases} \sqrt[3]{\mathsf{x_r}}, & \text{if } \mathsf{x_r} > \epsilon \\ \dfrac{\kappa \mathsf{x_r} + 16}{116}, & \text{otherwise} \end{cases} \\
f_y &= \begin{cases} \sqrt[3]{\mathsf{y_r}}, & \text{if } \mathsf{y_r} > \epsilon \\ \dfrac{\kappa \mathsf{y_r} + 16}{116}, & \text{otherwise} \end{cases} \\
f_z &= \begin{cases} \sqrt[3]{\mathsf{z_r}}, & \text{if } \mathsf{z_r} > \epsilon \\ \dfrac{\kappa \mathsf{z_r} + 16}{116}, & \text{otherwise} \end{cases} \\
\epsilon &= 216/24389 \\
\kappa &= 24389/27
\end{aligned}
\tag{3.6}
$$

The normalized reference white $\mathsf{x_r y_r z_r}$ is found from the reference white $\mathsf{X_r Y_r Z_r}$ which is computed as follows:

$$
\begin{gathered}
\mathsf{X_r} = \frac{1}{\mathsf{N}} \sum_i \bar{\mathsf{x}}_\mathsf{i} \mathsf{I_i} \Delta\lambda, \ \mathsf{Y_r} = \frac{1}{\mathsf{N}} \sum_i \bar{\mathsf{y}}_\mathsf{i} \mathsf{I_i} \Delta\lambda, \ \& \ \mathsf{Z_r} = \frac{1}{\mathsf{N}} \sum_i \bar{\mathsf{z}}_\mathsf{i} \mathsf{I_i} \Delta\lambda \\
\mathsf{x_r} = \mathsf{X}/\mathsf{X_r}, \ \mathsf{y_r} = \mathsf{Y}/\mathsf{Y_r}, \text{ and } \mathsf{z_r} = \mathsf{Z}/\mathsf{Z_r}
\end{gathered}
\tag{3.7}
$$

The saturation of a color is defined as:

$$
s_{ab} = \frac{\sqrt{a^{*2} + b^{*2}}}{L^*} \tag{3.8}
$$

The $L^*a^*b^*$ color space has the advantage of providing uniformly visual spacing and correlation with color perception. The L^* is for lightness where 0 is black and 100 white. a^* goes from green (negative values) to red (positive values) and b^* from blue (negative values) and yellow (positive values). The fundamental idea behind this color space is that equal changes in numerical values of coordinates correspond to identical perceived difference of coloration [124].

In situ transmission was obtained from a configuration as shown in Fig. 3.2.

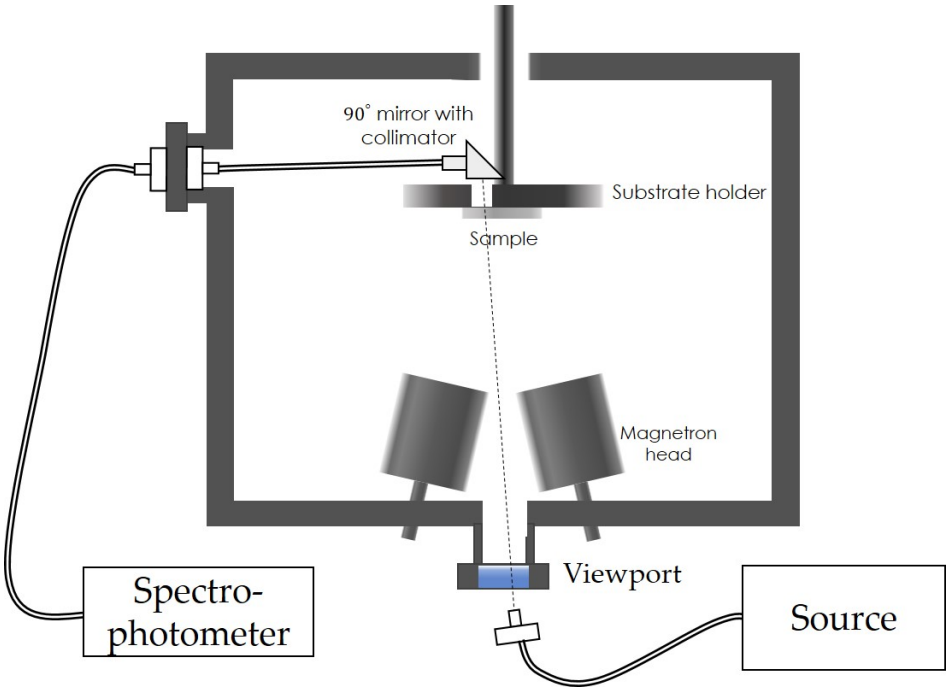

Figure 3.2 Schematic of the optical set-up configured for transmission monitoring to obtain color parameters of the gold film *in situ*.

3.2.4 Differential spectrometry

The change in reflectance during deposition is attributed to the formation of a thin film on the substrate. The reflectance depends on the coverage, the thickness, and the dielectric constants of the thin film, substrate, and ambient. Since no rotating hardware is required, the acquisition time is typically faster for reflectance spectroscopy comparatively to ellipsometry. As seen in Fig. 3.3, such an optical system is quite straightforward and requires fewer components than an ellipsometer.

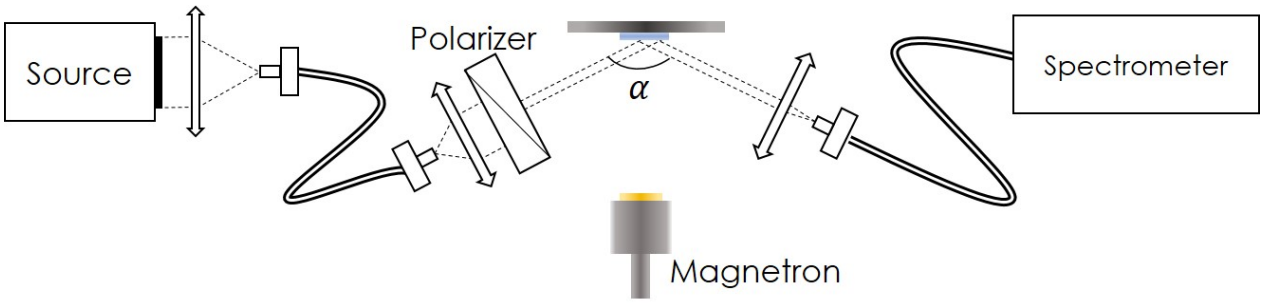

Figure 3.3 Schematic of a differential reflectance spectrometry system installed on the deposition system allows one to follow the evolution of reflectance during deposition.

Taking the differential of the normalized reflected signal highlights minute changes in the reflectivity of the surface, even for just a monolayer as shown in Fig. 3.4. Thus, differential reflectance is particularly sensitive for absorbing films.

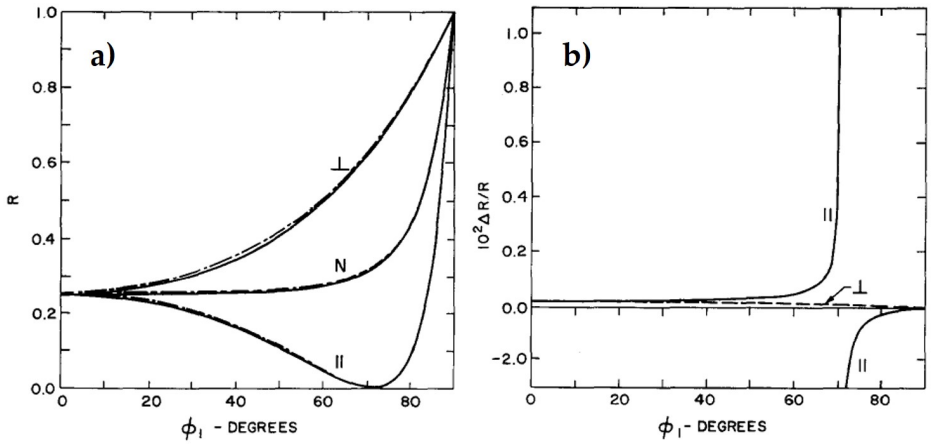

Figure 3.4 a) Reflectivity of a dielectric substrate (solid) and the same substrate with about one monolayer of an absorbing film (dashed) and b) the differential reflectivity $\Delta R/R$ caused by the absorbing monolayer film as a function of the angle of incidence of light and its polarization (thickness of the thin film d is very small compared to the wavelength $d/\lambda = 10^{-3}$). Taken from McIntyre and Aspnes [126].

For this research, a xenon lamp was initially used but the collimator system was very primitive and the lenses' AR coating affected the transmittance for wavelengths outside the range of 350 nm to 700 nm. Moreover, the lenses and the optical fiber's aperture was difficult to properly align as the mounting elements didn't have any angle adjustment. As a result, to reduce the risk that the source intensity drifted with time due to either the lamp's instability

or the vibration of the system, a compact super-continuum Energetiq $EQ-99X$ Laser Driven Light Source was later installed with a single wide-band metal-mirror collimator. This source is typically used to calibrate high-precision optical metrology equipment and is left constantly running so it doesn't require hour long pre-heating times, unlike the xenon lamp.

The silver mirror collimator from ThorLab $RC02FC-P01$ allows obtaining a 2 mm collimated beam from a 0.40 numerical aperture (NA) optical fiber. Since the mirror is parabolic, the focal length is constant for a broad range of wavelengths contrarily to lenses, a great advantage. Despite being advertised as 450 nm$-$2 μm @ 97.5% reflectance, more than 90% at 400 nm for both s- and p-polarization is still reflected.

In-situ optical measurements were carried out using a TEC5 UV-VIS-NIR spectrophotometer with an acquisition time of 125 ms - each spectrum consisting in the average of $25 \times$ 5-ms-spectra. To prevent backside reflection from the sample, the rear surface was sandblasted. Polarization was controlled via a broad-band polarizer from an old variable angle spectroscopic ellipsometer (VASE).

The differential reflectance is defined as:

$$\frac{\Delta R}{R} = \frac{R(\delta) - R(0)}{R(0)} \tag{3.9}$$

with δ representing the effective deposited thickness.

In this study, instead of the differential, it's the time-derivative of the reflectivity for each wavelength of the spectrum that is calculated. First, a reference spectrum $R_0(\lambda)$ is acquired using the UMA that allows the conversion of the *in situ* intensity measurement $I(t, \lambda)$ into reflectivity spectra $R(t, \lambda)$. To do so, the system is calibrated from a reference spectrum intensity $I_0(\lambda) = I(t = 0, \lambda)$ which is done right before deposition. Then, a transformation vector ν is found to convert subsequent intensity measurements into reflectivity:

$$\nu = R_0/I_0 \tag{3.10}$$

$$R(t, \lambda) = I(t, \lambda) \times \nu \tag{3.11}$$

This calibration step is crucial. Any change of alignment or fluctuation of the source intensity will affect the measured reflectivity of the film. Furthermore, the numerical time-derivative

is calculated by:

$$\frac{\partial R(t,\lambda)}{\partial t} = \frac{R(i+1,\lambda) - R(i,\lambda)}{t_{i+1} - t_i} \tag{3.12}$$

Note that the time can be converted into the film's effective thickness δ knowing the deposition rate (nm/s). The *in situ* transmission can be obtained in a similar fashion.

3.2.5 Reflection and transmission coefficients

The refractive index dictates the behavior of a material when exposed to light, *i.e.* how much of it is reflected R, transmitted T, absorbed A and scattered S from the initial incident light. Absorption and scattering are more often combined and denoted as the extinction Ext because absorption and scattering are evaluated using the relation $A + S = 1 - R - T$. The Fresnel coefficients of a multi-layer system can be obtained by applying the matrix approach developed by Abelès [127]. A software called *Openfilters* [128], developed at the *FCSEL*, has implemented the method to calculate the optical coefficients at various angles, thicknesses and for many layers of thicknesses d_i and respective refractive indices N_i. For each layer, the incident light comes from a medium of refractive index N_{inc} and exit medium N_{ex} and a matrix M_i is defined as:

$$M_i = \begin{bmatrix} \cos\phi_i & (i/\eta_i)\sin\phi_i \\ i\eta_i \sin\phi_i & \cos\phi_i \end{bmatrix} \tag{3.13}$$

with

$$\eta_i = \begin{cases} N_i \cos\theta_i & s\text{-polarisation} \\ N_i/\cos\theta_i & p\text{-polarisation} \end{cases} \tag{3.14}$$

and

$$\phi_i = \frac{2\pi}{\lambda} N_i d_i \cos\theta_i \tag{3.15}$$

being the phase shift of the EM wave inside the layer. θ_i is the angle of incidence in the i^{th} layer which changes as the wave propagates in the stack of N_i refractive indexes according to Snell-Descarte's law $N_{inc}\sin\theta_{inc} = N_i \sin\theta_i$.

The product of all the i^{th} matrices yields the characteristic matrix:

$$M = \begin{bmatrix} m_{11} & m_{12} \\ m_{21} & m_{22} \end{bmatrix} \tag{3.16}$$

for which the Fresnel coefficients R and T can be found according to:

$$R = \mathrm{r}\mathrm{r}^* \tag{3.17a}$$

$$T = \frac{\Re(N_{ex})}{\Re(N_{inc})}\mathrm{t}\mathrm{t}^* \tag{3.17b}$$

with

$$\mathrm{r} = \frac{\eta_{inc}m_{11} - \eta_{ex}m_{22} + \eta_{inc}\eta_{ex}m_{12} - m_{12}}{\eta_{inc}m_{11} + \eta_{ex}m_{22} + \eta_{inc}\eta_{ex}m_{12} + m_{12}} \tag{3.18a}$$

$$\mathrm{t} = \frac{2\eta_{inc}}{\eta_{inc}m_{11} + \eta_{ex}m_{22} + \eta_{inc}\eta_{ex}m_{12} + m_{12}} \tag{3.18b}$$

Note that Eq. 3.17 don't consider the backside reflection. However, it's exhaustively detailed in Larouche *et al.*'s article [128].

3.3 Surface imaging

3.3.1 Electron microscopy

The maximum resolution of an optical microscope is defined as [129]:

$$r = \frac{0.61\lambda}{N\sin\alpha} \tag{3.19}$$

with λ the wavelength, N the refractive index between the object and objective, and the angle aperture α. The lowest light wavelength used in microscopy is approximately 200 nm as anything lower would require an exotic lens system. For green light, the absolute resolution limit is around 150 nm (for $N\sin\alpha \approx 1.6$) [129].

With electron microscopy, μ can be asserted as unity and α is very small so that $\sin\alpha = \alpha$. The wavelength is determined using the de Broglie relation $\lambda = h/p$ and with $\alpha = 0.1\ rad$ ($\sim 5°$) and as such, the resolution limit of a 1 kV electron beam is 236 pm. However, the magnetic lenses of an electron microscopy cause aberrations (largely due to the energy distribution of the electrons) and the resolution is actually far from this limit, but still much lower than that of optical microscope. For TEM, sub-atomic resolution is easily attainable.

Transmission electron microscopy (TEM) was used as the preferred imaging method since the resolution is much higher than scanning electron microscopy (SEM) for instance. The TEM images were obtained using a JEOL $JEM-2100F$ at a 200 kV working voltage on 30-nm-thick silicon nitride membranes (window size 0.25×0.25 mm) from Norcada. The microscopes was equipped with a Schottky field emission gun (FEG).

The resolution of an electron microscope is affected by the electrons' velocity (accelerating voltage) and the interaction volume of the electrons within the sample [130]. An SEM working voltage is much lower to prevent electrons to penetrate too deep inside the sample which decreases the resolution. Also, non-conductive materials suffer from charge accumulation (electrons are trapped inside) which deflects the probing electron beam. The use of a low-current and conductive coating helps to mitigate this latter effect.

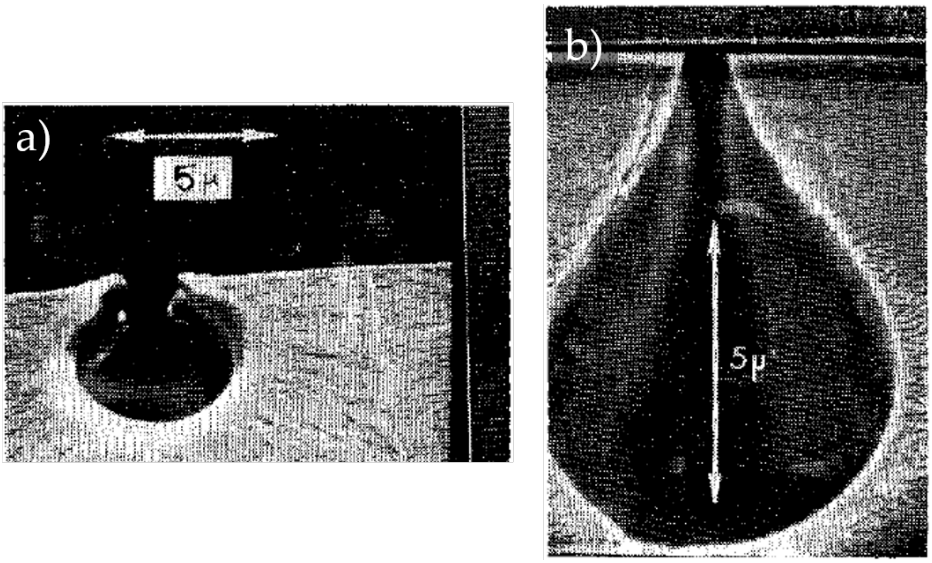

Figure 3.5 Scanning electron micrographs showing the profile of the interaction volume of electrons regarding the working voltage used for (a) 14.86 kV and (b) 29.5 kV beam voltages. Taken from Herzog *et al.* [130].

Conversely, TEM does not suffer from any of the SEM's drawbacks except that the sample must be very thin (< 100 nm), a condition difficult to obtain in most studies. In the present case, the deposition of gold was after a 10 nm SiO_2 seed layer on top of the 30 nm thin membrane. However, the imaging was done on a different sample than the one where the *in-situ* surface reflectance was conducted. The impact of this difference was not studied but will be discussed further. Since the electrons are transmitted, the volume of interaction is very small and no charges are accumulated; this allows the use of greater beam energy, improving the resolution (smaller wavelength and interaction volume).

3.3.2 Image analysis

The images were obtained by TEM observations and were treated using an in-house thresholding script combined with the *ImageJ* software. The first step is to smooth the image with a median filter to reduce the noise, detrimental to the thresholding process. The median

filter is preferred as it preserves the edges contrarily to other types of filters, *e.g.* Gaussian blurring [131]. Then, the image brightness and contrast are modified using an *ImageJ* built-in function. The insert in Fig. 3.6b shows a typical bi-modal gray-level distribution of a gold-island film. The thresholding process aims at separating the two populations by attributing to every object pixel the value 255 (white) and background pixel the value black (0). As seen in Fig. 3.6a, the background is lighter than the gold islands and is set to black.

In order to help the algorithm differentiate between the two populations, the brightness and contrast are manually adjusted in *ImageJ* as shown in Fig. 3.6b. Then, an adaptive threshold function is applied to the image via a *Python* script from the *OpenCV* library and the resulting image after this step shown in Fig. 3.6c. This function locally averages the pixels' intensity value of a user-set amount of pixels. To put it simply, the algorithm scans the image and for every position, it determines an average pixel intensity value. If the current pixel has an intensity higher than the average, it is set to a wanted value, *e.g.* 0 (black) in this case. To include the islands' edge, an offset value is set so that it's either subtracted or added to the mean calculated value. The pixels that don't meet the requirement are automatically set to white.

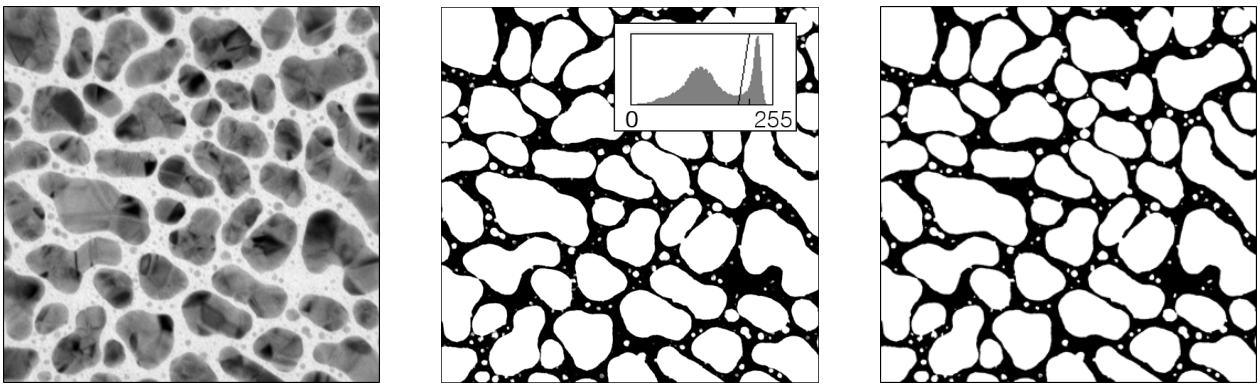

(a) TEM image as-is.

(b) After brightness and contrast adjustment.

(c) After local thresholding.

Figure 3.6 a) 6 nm effective thickness of gold deposited at 100° C on B270 substrate. b) Intermediate step to improve c) the adaptive threshold accuracy algorithm. Parameters used for the local threshold: kernel size for local mean was 143 (12×12) and the offset was 0.

To make sure that the threshold algorithm preserves correctly the islands' boundaries, the brightness and contrast step is mandatory and especially for higher deposition temperature as the film tends to have very big islands surrounded by much smaller ones. This contrast of size pushes the local threshold to its limit as a too large averaging area will cast the

smaller islands as background pixels while a smaller one causes some pixels inside of the big clusters to be in turn considered as background. Increasing the contrast make the smaller islands stand out more, increasing their weight on the local average so they aren't classified as background pixels.

Once satisfied with the thresholded image, the island density, area, average distance, and coverage can be swiftly obtained with the *ImageJ* integrated tools. The software can detect the edge of the particles in the thresholded image. This step can be done via the *OpenCV* function *findContour* as well, but since *ImageJ* has multiple already integrated scripts and plugins, it was the preferred option. From the software analysis of particle count, area and circularity are extracted. The circularity of a NP is defined as:

$$Circularity = 4\pi \times Area/Perimeter^2 \tag{3.20}$$

and is used to describe how close a 2D particle is to a true circle. The idea is very simple, a circle's perimeter is $2\pi \times radius$ and its area $\pi \times radius^2$. A true circle will yield 1 whereas any other form will tends to have a larger perimeter comparatively to the area ($Circularity < 1$).

CHAPTER 4 RESULTS AND DISCUSSION

In this chapter, the results from gold deposition on two different seed layers and capping materials are presented. To explore the available color space, a broad variety of gold films with different effective thicknesses were produced with multiple configurations of seed and capping layer materials. Subsequently, the adhesion in function of the gold thickness is tested to explore the limitations of gold-island film incorporation into an ophthalmic lens coating.

Ion bombardment was identified in Sec. 2.3.7 as a potential alternative to annealing to improve the SPR peak attributes, *i.e.* bandwidth and amplitude. *In situ* transmission monitoring is used as a method to investigate if the addition of a substrate bias during deposition is beneficial for color generation.

4.1 Effect of the seed layer and encapsulating material

As seen in Fig. 4.1, increasing the effective refractive index generates a red-shift of the absorption peak, in accordance with Fig. 2.14. Silica and titania were used due to their refractive index contrast (1.50 vs 2.65 at 550 nm respectively) and the relative ease of deposition.

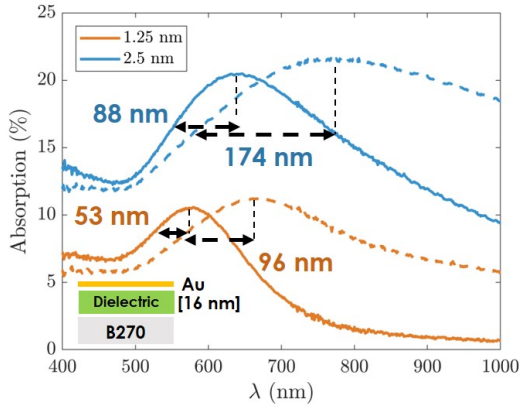

(a) SiO_2 (solid) and TiO_2 (dashed) seed layers for different gold effective thicknesses. The FWHM is provided to compare the impact of the change.

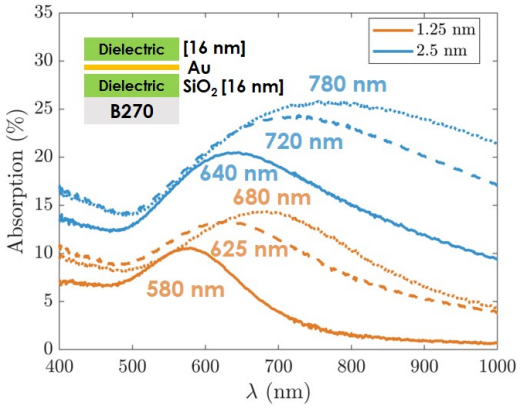

(b) Variation of the encapsulation material for gold films uncoated (solid), SiO_2 overcoat (dashed) and TiO_2 overcoat (dotted). The peak position is identified for each curve

Figure 4.1 *Ex situ* absorption measurements of gold films deposited at room temperature with a) different seed layers and b) encapsulating material. Two effective thicknesses of 1.25 nm (red) and 2.5 nm (blue) were deposited on a B270 substrate and the thickness of each dielectric layer was 16 nm.

One can note a broadening but also an increase of the amplitude of the peak with an increase of the surrounding refractive index. This behavior is commonly observed for redshifted SPR peak due to the increasingly heightened free-electron damping attributed to gold's dielectric constant ε'' higher value at longer wavelengths [132] whereas ε' gets more negative which results in a greater Q factor (as seen in Sec. 2.4.6), explaining the increase in amplitude of the peak.

To obtain a better idea of the resulting colors, 40 gold films were deposited with different combinations of dielectric and gold effective thicknesses. The colors in transmission are represented in Fig. 4.2.

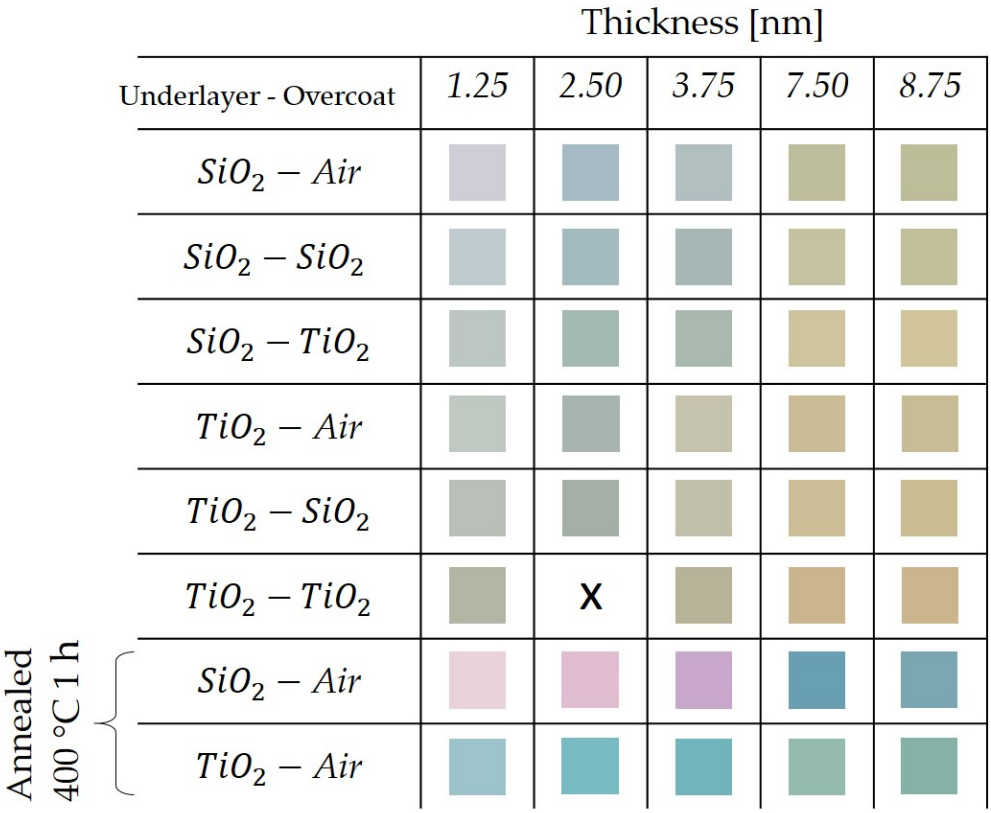

Figure 4.2 Corresponding transmitted colors in sRGB (CIE 1931 2° observers, D65 illuminant) of gold films with different configurations and effective thicknesses. Depositions were done on B270 substrates and the TiO_2 and SiO_2 layer thicknesses was 16 nm. The last two rows of gold films were annealed after deposition. Note: the missing sample detached from the sample holder during deposition and was lost.

The 1.25 nm SiO_2 film at room temperature has a slight reddish hue whereas the 1.25 nm TiO_2 undercoated film presents a more greenish color attributed to the redshift of the absorption

peak. One can quickly notice that annealing is the parameter that affects the coloration the most. The Fig. 4.3 shows the comparison of the same film before and after annealing. The resulting colors have increased saturation (narrower absorption) and amplitude (absorption intensity). This feature heightens the contrast between silica and titania.

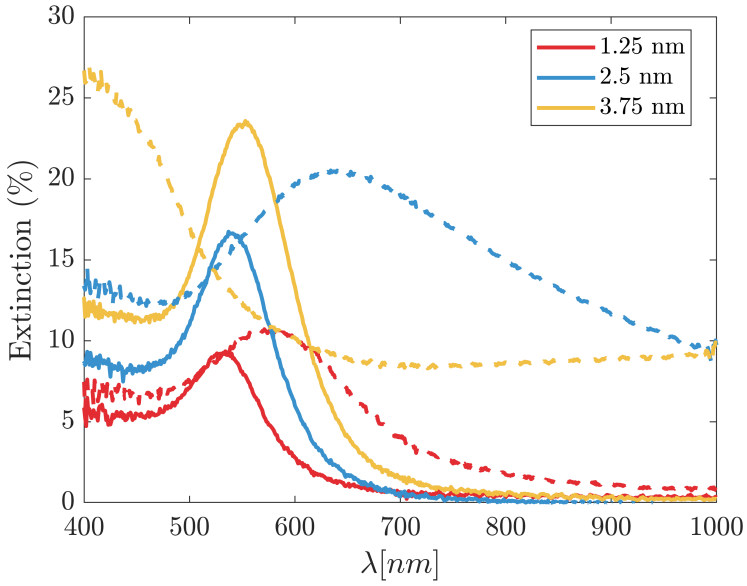

Figure 4.3 Gold films deposited at room temperature on B270 as-deposited (dashed) and after annealing at 400°C for 1 hr (solid).

From these results, one can conclude that the variation of the surrounding medium has a major impact on the resonance peak location but also its amplitude. Furthermore, annealing was found to significantly improve the color vividness of the films. Moreover, annealed films at a high effective thickness ($\delta > 7.5$ nm) still exhibit colors attributed to surface plasmon excitation which effectively disappear already at $\delta = 3.75$ nm for films deposited at room temperature. This effect can be explained due to the de-wetting of the continuous film, allowing it to reorganize as islands which relax into a spheroidal shape during the annealing treatment (see Sec. 2.3.5).

4.2 Durability

Faraday discovered that thermally evaporated gold films could easily be wiped off from the glass surface but not where the gold had incorporated into the substrate due to the heat of the explosion (see Sec. 2.2.1). This discovery highlights the vulnerability of metal-island films that have poor adhesion which is a direct consequence of the 3D growth mode. Since

the thin gold film bonding with the substrate is low, the layer integrity depends on the seed and capping layer bond instead. To asses the applicability of plasmonic layers incorporation on ophthalmic lenses, an in-house layer adhesion test was used that mimics a human cleaning a lens.

Three gold films of 2, 4 and 8 nm with different colors (blue-, green- and yellowish respectively) were deposited to test the impact of the gold thickness on the adhesion of the seed and capping layer. Furthermore, a second gold layer of a 2 nm gold film was added on top of a layer of the same film thickness (capped with SiO_2) to increase the color saturation and study the impact on the durability of the coating with an additional plasmonic layer (the 2x2 nm film). The extinction spectra of the samples are presented in Fig. 4.4.

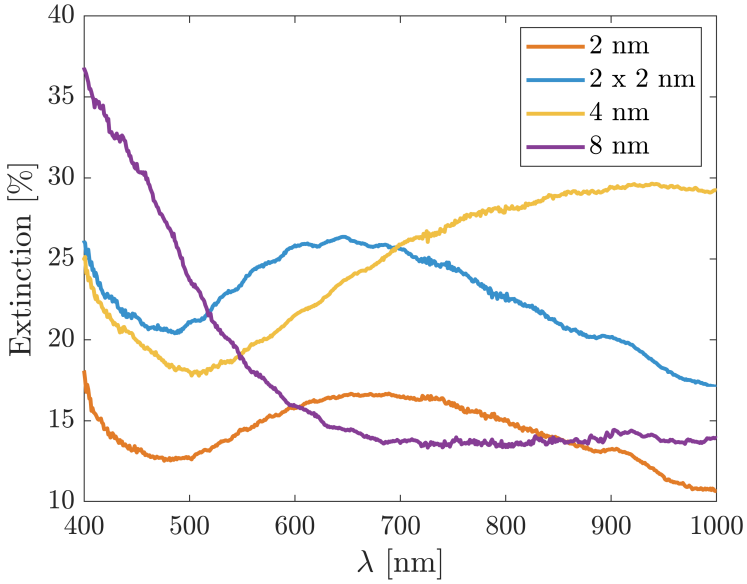

Figure 4.4 Gold films deposited at room temperature on 20 nm SiO_2 seed layer and capped with another 20 nm silica layer on a borosilicate glass substrate.

Both 2 nm and 2x2 nm samples exhibit a well-defined LSPR peak, suggesting an island-film. The anomalous absorption in the NIR for the 4 nm sample corresponds to a structure of isolated islands surrounded by a conductive network as described in Sec. 2.4.6. Lastly, the 8 nm sample's spectra are typical for a continuous gold film. Gold films of corresponding thicknesses to that presented in Fig. 4.4 were deposited on curved Orma substrates.

The experimental apparatus consists of a tip of about 1" × 2" which applies 60 N load on the sample covered by a Selvyt cloth lightly soaked in isopropanol alcohol. Every 10 times the tip rubs the sample (which corresponds to $\mathsf{N} = 1$), the operator inspects visually the

lens. Upon visible delamination, the test stops. The delaminated gold films deposited on the curved Orma are shown in Fig. 4.5. One can note that the adhesion decreases rapidly as the gold film's thickness is increased. Moreover, adding a second layer also reduces the durability of the composite. At $\mathsf{N} = 12$ which corresponds to 120 passes, the adhesion of the film is considered good.

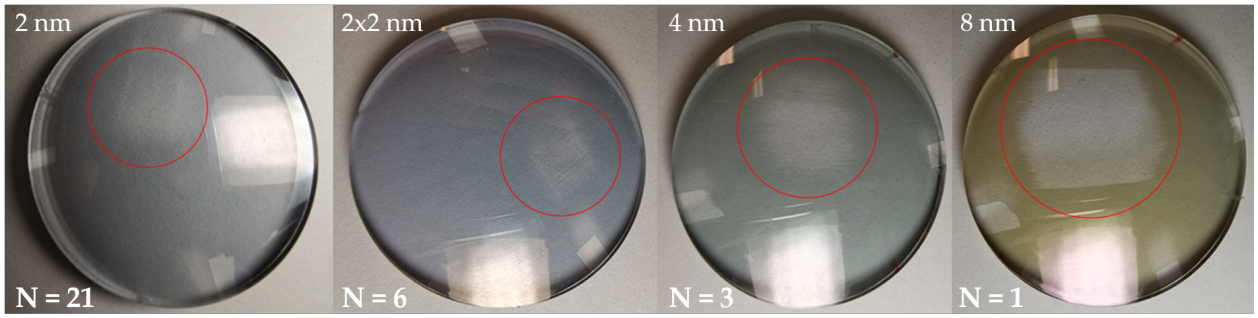

Figure 4.5 Photography after delamination of the gold films deposited at room temperature on curved Orma substrates with 20 nm SiO_2 seed and capping layer. A fluoro-carbon top coat $\sim$ 5 nm was deposited by thermal evaporation usually used on ophthalmic lenses for its anti-smudge propriety and low coefficient of friction to simulate a typical lens. The film thicknesses are identified in the figures. Note: the 2x2 nm film consists of two 2 nm gold films separated by a 20 nm silica layer in-between.

In light of these results, coating adhesion can be improved by reducing the gold film filling factor. However, color saturation is stronger for thicker gold films. One can add a second layer to increase such parameter, at the cost of lower durability. Yet, the 2x2 nm sample fares twice as much as its 4 nm counterpart. Thus, it is possible to obtain a viable coating by limiting the effective thickness of gold.

Color can further be adjusted for a given gold-island by modifying the surrounding medium refractive index as demonstrated in Fig. 4.1. In fact, the LSPR peak shift is known to have a linear dependence with the surrounding refractive index change [94]. However, the broadening of the peak's linewidth can be undesirable to properly tune the color. This effect is attributed to a greater ε'' value at longer wavelengths resulting in an increasingly dampened free-electrons oscillations as the SPR peak is redshifted. Silver has considerably less variation of this dielectric parameter and would thus be the ideal candidate to obtain a film with a tuneable absorption peak that remains narrow. This attribute would allow one to select a wanted color and through multiple plamonic layers deposition obtain the desired color saturation.

4.3 Gold film optical monitoring and effect of ion bombardment during growth

Notwithstanding the limitation of gold for the studied application, one can wonder how to optimize the system to mitigate this downside. The first answer to that question was already addressed, *i.e.*, minimization of the surrounding medium refractive index. Secondly, from the results shown in Fig. 4.1, the increase of the gold film's effective thicknesses enlarges the resonance peak's linewidth. This effect can be mitigated by heating the sample. Although, annealing temperatures are largely superior to what plastic substrates can sustain which severely limits the margin for color tuning. Ion bombardment has been introduced in Sec. 2.3.7 as a potential alternative to the heating of the substrate's surface to improve a metal-island film's optical properties. To evaluate if the addition of ion bombardment during growth is beneficial in terms of color hue, *in situ* transmission monitoring is conducted through the depositions of gold films with different bias voltages.

4.3.1 Color evolution during gold film growth

Literature on the subject of *in situ* color evolution and impact of ion bombardment is nonexistent for deposition via sputtering. To obtain transmission spectra, a new sample holder was designed to allow light collection from the rear of the sample using an optical fiber inside of the vacuum chamber. The light source was installed right underneath the deposition chamber and an optical feed-through allowed to illuminate the sample as depicted in Fig. 3.2. Obviously, the *in situ* monitoring of color is practical to rapidly explore for a given deposition condition (seed layer, surface temperature, deposition rate, etc.) whether it improves the desired color hue (a^* and b^*) and luminance (L^*) or not. Furthermore, this optical monitoring system can help to understand the underlying phenomena at the origin of the change in the evolution of the optical properties of the layer.

Alumina was selected as a seed layer due to its lower sputter yield comparatively to SiO_2 (about 1:2 at 600 eV [133]) and a low refractive index (1.68 at 550 nm [134]). Indeed, ion bombardment treatments are known to roughen surfaces [51], unfavorable for island growth, an effect discussed in Sec. 2.3.7.

Figure 4.6 presents the a^*b^* color parameter evolution throughout gold deposition on Al_2O_3 for each condition.

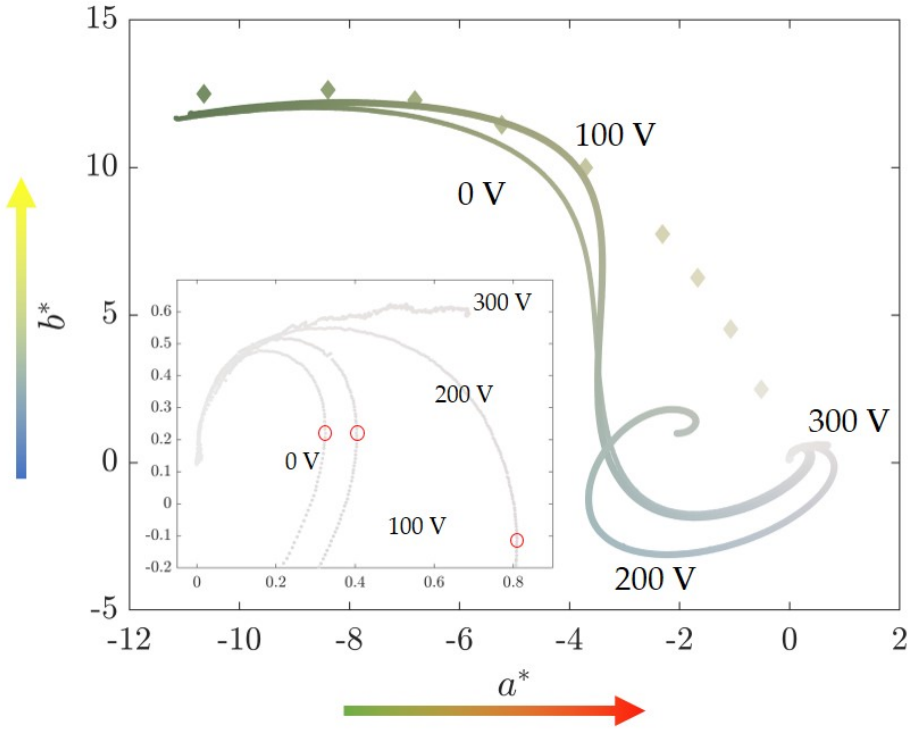

Figure 4.6 *In situ* transmission of a gold island film deposited on a 20 nm Al_2O_3 seed layer with varied bias values from 0 to -300 V. Diamond markers is the color of theoretical continuous gold films of thicknesses from 1 to 20 nm. Inset shows a zoomed region corresponding to the beginning of the gold deposition. The color arrows indicate toward what color hue the numerical value leans to. Each plotted markers on the figure exhibit the corresponding RGB value of the $L^*a^*b^*$ coordinates plotted. The red circled markers are attributed to the maximal a^* value on the graphic for each condition.

The saturation s_{ab} (see Eq. 3.8) refers to the color intensity and is shown in Fig. 4.7 from the experimental transmission spectra previously presented in Fig. 4.6.

Aside from the -300 V deposition condition, all exhibits initially the same behavior of both a^* and b^* value increasing followed by a decrease of b^* as it goes from positive to negative value. For this stage of growth, the color goes from orangish to reddish. Then, blue becomes dominant (b^* negative and a^* decreasing) as the saturation starts to increase back again at 28, 36 and about 58 s for 0, 100 and 200 V respectively.

A shift in coloration is observed later as the a^* parameter considerably increases comparatively to b^* in Fig. 4.6, this moment is characterized by a kink in the saturation curves of Fig. 4.7 and the color becomes greenish. The b^* parameter reaches a minimum and past

this point, subsequent deposition for 0 and 100 V conditions turns the films yellowish. Then, a strong increase of the green hue (a^* more negative) follows which is characteristic of a continuous gold film. However, for the 200 V film, when the b^* parameter starts to become more positive for $a^* \approx 3.7$, the color evolution curve deviates significantly from the 0 and 100 V ones. Additionally, The final transmission spectrum does not correspond to a continuous gold film (see Fig. 4.8).

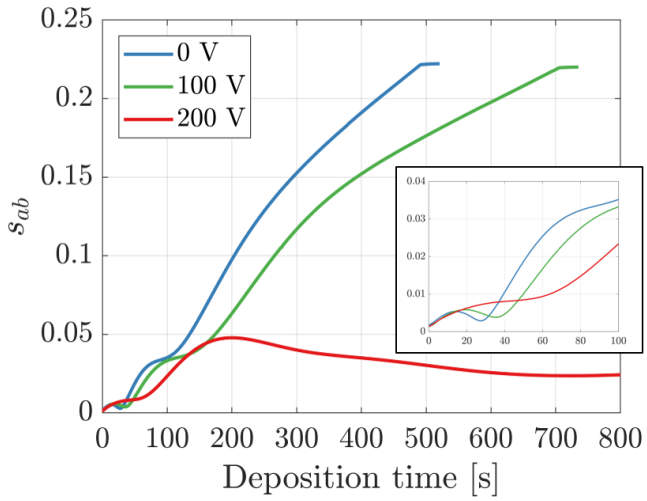

Figure 4.7 Saturation s_{ab} of the gold films in function of the deposition time for each condition.

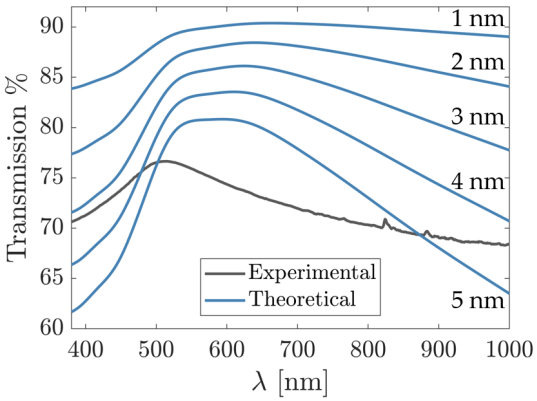

Figure 4.8 Transmission spectrum at the end of the -200 V gold film deposition experiment compared with the theoretical spectra of continuous gold layers at different thicknesses.

Looking at the spectra corresponding to a a^* maximum, which are presented in Fig. 4.9, the -200 V bias spectrum shows a rather selective blocking for $\lambda = 544$ nm whereas the other two conditions have a barely perceptible transmission dip around $\lambda \approx 540$ nm. The

luminosity (L^*) is similar but the color hue of the -200 V spectrum is nearly purely red with a a^* parameter value twice that of the 0 and -100 V bias conditions. Surprisingly, subsequent deposition past the reddest color parameter shows a decrease of luminance and reduction of the a^* parameter as seen from Fig. 4.9a for each condition. The final color parameters converge to that of a continuous gold film for both 0 and -100 V bias conditions.

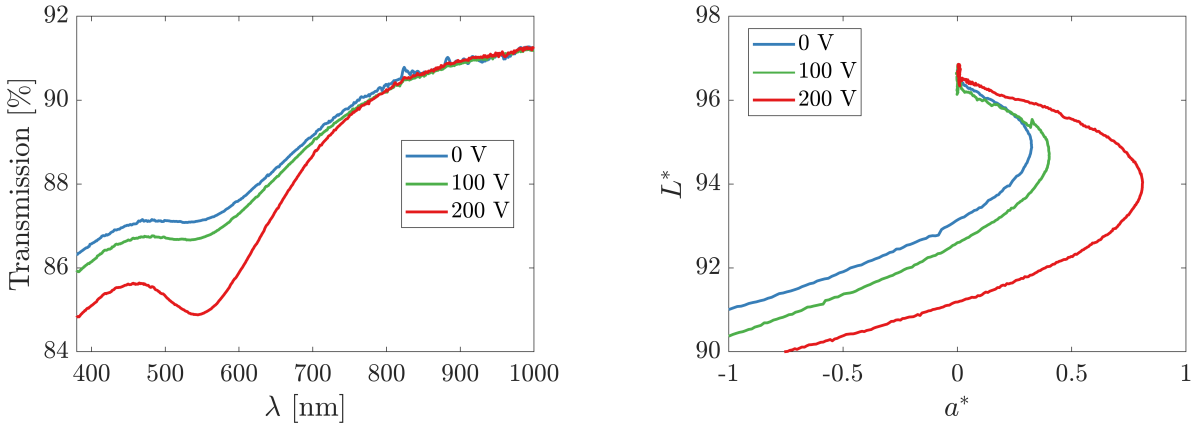

(a) Transmission spectra of the maximum a^* for each condition.

(b) Evolution of the L^* in function of a^*.

Figure 4.9 The $L^*a^*b^*$ parameters of the three spectra of the left figure are: [95 0.32 0.22], [95 0.40 0.22] and [93 0.81 -0.11] for 0, -100 and -200 V respectively. The corresponding deposition time are: 22, 28 and 56 s (as identified on Fig. 4.6).

In essence, these results demonstrate that ion bombardment promotes a more saturated red color to be obtained for depositions at room temperature on alumina. To obtain the color table presented in Fig. 4.2, 5 gold films per condition had to be deposited. With the *in situ* transmission monitoring method presented here, only a single experiment was necessary to explore the available color space for a specific configuration, *e.g.* a seed layer of alumina and a bias value.

From this study, it was determined that the bias value of -300 V highlights the limitation of the proposed method as the color evolution stagnates after a minimal color shift. This behavior is attributed to a rising sputter yield as a function of the gold coverage on the substrate. Such a hypothesis suggests that the atom condensation and resputtering rate must reach an equilibrium, and so the growth ceases once a critical coverage is attained.

4.3.2 Gold-island film morphology and color evolution

The presented *in situ* transmission monitoring method allows one to optimize a gold-island film color hue and saturation. Furthermore, it was determined that lower thickness films fared better in the durability test presented in Fig. 4.5. Hence, the available colors to generate a durable coating are limited to islands films with low filling factors to promote the bond strength between the seed and capping layer. This section associates a morphology for each color perceived for gold island films at different growth stages.

To obtain microstructural information of the gold-island films, TEM observations were conducted at various deposition times and bias values shown in Fig. 4.10, 4.11, and 4.12. The size and shape distributions of the islands are given in Fig. 4.13.

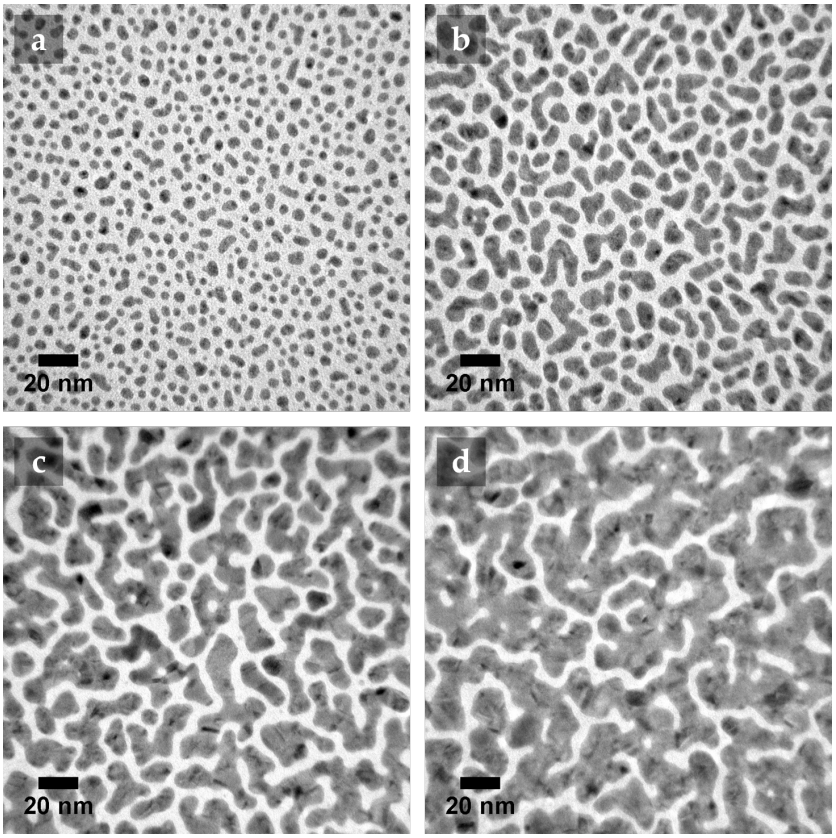

Figure 4.10 TEM images of the reference gold films deposited with no bias applied for a) 25, b) 50, c) 75 and d) 100 s corresponding to an effective thickness of about 1.1, 2.2, 3.3, and 4.4 nm respectively. Note: the deposition rate was 0.44 nm/s.

On the 25 s film at 0 V, many islands have already coalesced which suggests that the growth stage II has been reached. This deposition time is close to that attributed to the maximum in a^* parameter observed at 22 s in Fig. 4.9 and confirms that round and isolated islands

have a narrower absorption peak. For the 50 s film, all islands have coalesced and some became worm-like which can be associated with the beginning of the growth stage III (refer to Sec. 2.3.6). The film deposited for 75 s shows a branched structure, typical for the domain coarsening (III) growth stage, where very few isolated islands are left accompanied by a skyrocketing island average surface area (see Fig. 4.13). The size distribution is no longer normal and the circularity far from that of spheroids. Lastly, the 100 s film is percolated which corresponds to the growth stage IV.

In terms of coloration, the island film (25 s) is pinkish (some red mixed with blue) as the LSPR peak absorbs mostly between $\lambda = \{500,\ 600\}$ nm. When islands coalesce (50-75 s), their shape becomes elongated and the resonance peak along the longer axis is greatly redshifted (covered in Sec. 2.4.7). Moreover, the size distribution broadens and the redshift of the LSPR enlarge the peak linewidth. The resulting extinction spectra (similar to the 2 nm film shown in Fig. 4.4) blocks significantly more the light above $\lambda = 500$ nm and the film is consequently blue in transmission. The 100 s film is percolated and the conductive network couples with isolated islands and gives rise to an anomalous NIR absorption (described in Sec. 2.4.7). The corresponding extinction spectra are shown in Fig. 4.4 for the 4 nm film which absorbs significantly more for $\lambda > 600$ nm and the film is, as a result, greenish in transmission.

The 25 s film's morphology at -100 V is nearly identical to the reference one at 25 s. The average island area is similar (21 vs 18 nm^2) and the circularity slightly higher for the -100 V film (0.87 vs 0.90). The size distribution is also tighter, shown by the error bar corresponding to the standard deviation of the distribution in Fig. 4.13. The 75 s at -100 V film is visually similar to the 50 s at 0 V film which is confirmed by the coverage (50.25 vs 54.5%) and the statistical analysis of the surface area that is 87 vs 90 nm^2 for the 0 and 100 V films in order. Although, the standard deviation for the 100 V is smaller as well as the circularity (0.72 vs 0.76) respectively.

The higher circularity for the 100 V film suggests that the ion bombardment promotes shape relaxation. This latter point could be proven considering islands as hemispherical caps and finding the associated volume and contact angle satisfying the deposited volume of gold.

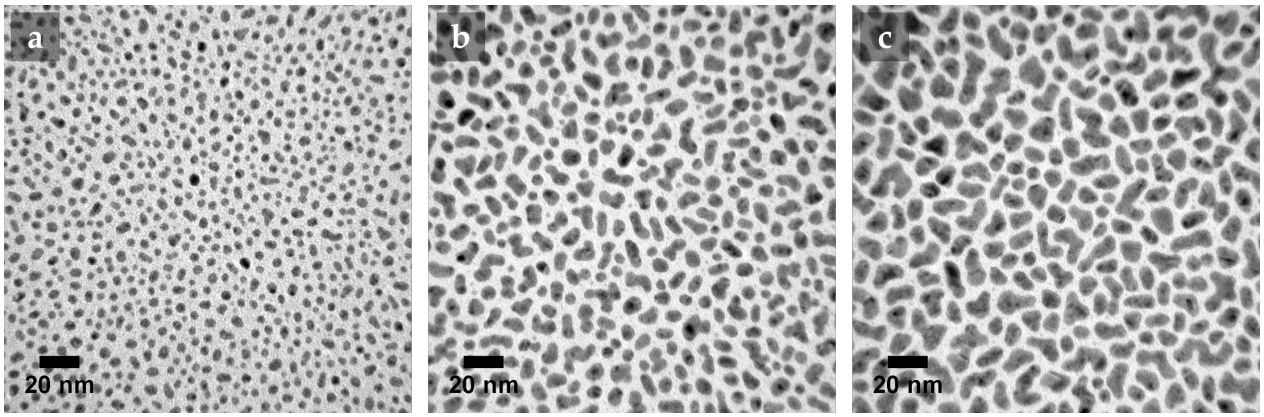

Figure 4.11 TEM images of gold films deposited with a bias value of -100 V for a) 25, b) 50, and c) 75 s.

Due to their similarities, one could make the educated guess that the 50 s at 0 V and 75 s at 100 V films effective thicknesses are close (considering the nearly identical coverage) and conclude that the observed differences, especially the circularity, are related to the dewetting of the islands due to the ion bombardment. However, the measurement of irradiated film's effective thickness is challenging. The effective deposition rate varies as previously discussed and the QCM is not subjected to the generator bias. The crystal could be placed on the substrate holder but to obtain a similar growth behavior one should coat the resonator with a dielectric. Secondly, the dielectric thickness must be sufficient to sustain the etching during deposition to prevent the gold layer underneath to be exposed. Lastly, the etched material from the disk has to be evaluated which is not trivial. For this hypothesis to be verified, one should obtain an accurate value of the height of the islands. Such a feat has been accomplished by Catin *et al.* who were able to determine the height of gold islands from X-ray photoelectron spectroscopy (XPS) analysis [135]. Although, this method is limited to only 10 nm height features due to the photoelectron's low kinetic energy limiting the probing depth.

A gold film was arbitrarily deposited for 75 s at a bias of -200 V which appeared to correspond to the point when the film starts to become blue dominant after a closer look at the color saturation curves features (see Fig. 4.7). Small kinks are visible at the start of the deposition for 0 and -100 V especially. Right before the (b^*) parameter increases rapidly, a small change of trend is visible at 34 and 43 s for 0 and -100 V. For -200 V, this point happens to be around $\sim$ 75 s as well.

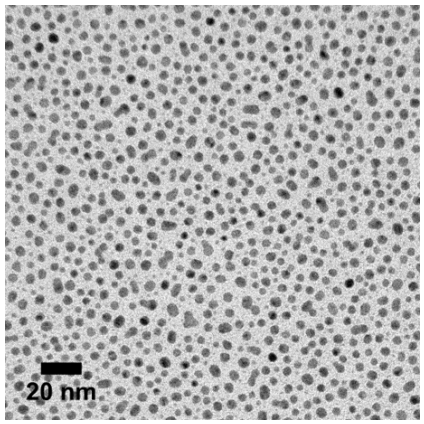

Figure 4.12 TEM image of a gold film deposited with a bias value of -200 V for 75 s.

Comparing the morphology statistics of the films, the 25 s at -100 V film is evidently the closest match to the film deposited for 75 s at -200 V (see Fig. 4.12). The circularity is the same (0.9) with a size distribution slightly better for the -200 V than the -100 V film (0.06 vs 0.07). However, despite an average island size smaller (12 vs 18 nm^2) for the -200 and -100 V films respectively, the size distribution is comparatively worse 7.9 vs 8 nm^2. This latter observation can be attributed to the formation of tiny islands that are not visible in the 25 s -100 V film. This phenomenon can be attributed to the side effect of ion bombardment: surface roughness. Indeed, as extensively discussed and seen in Sec. 2.3.7, the surface damage hinders the surface diffusion of the adatoms and promotes island nucleation.

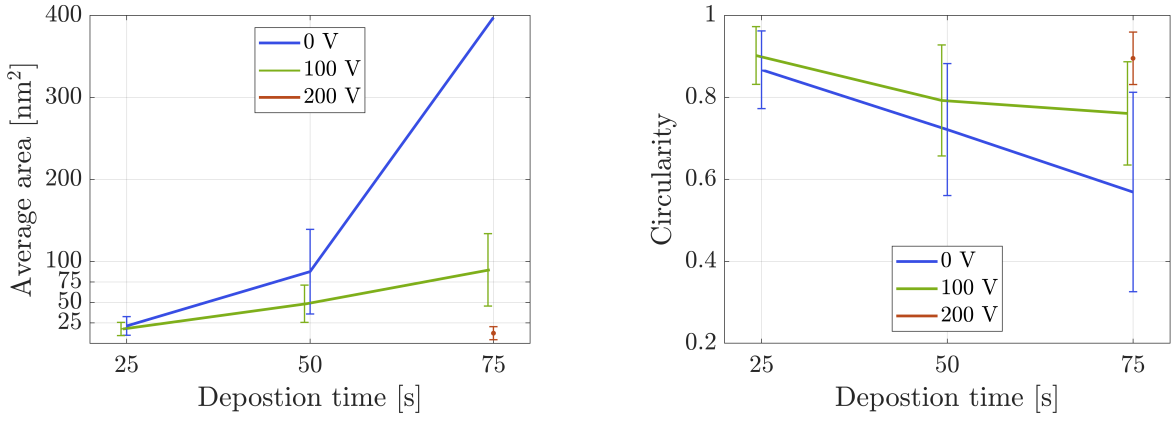

(a) Islands average area.

(b) Average circularity of the islands.

Figure 4.13 Statistical representation of the size and shape distribution of the islands for different deposition time & bias value. The circularity is defined as $Circularity = 4\pi \times Area/Perimeter^2$. The standard deviation of the island distribution for 0 V at 75 s was greater than the average island area due to a distribution no longer normal and was left out.

One last effect to consider is the heat contribution of the ion bombardment which hasn't been evaluated for these experiments. Judging from the TEM images, the deposition rate at −200 V is at least a third of the one with -100 V bias. Although, from the presented result, no clear improvement attributed to this effect could be determined.

In summary, the film morphology could be attributed to observed color hues at different growth stages.

4.3.3 Post-deposition ion bombardment

So far, ion bombardment has been used during deposition and it was not possible to conclude precisely whether it is the substrate heating or the momentum transfer effect (local heating) that contributed the most to the improvement of the film's color parameter in terms of a red hue. An experiment was done with reflectivity monitoring to explore the effect of post-deposition ion bombardment on the film's color parameters. The result of such an experiment is shown in Fig. 4.14.

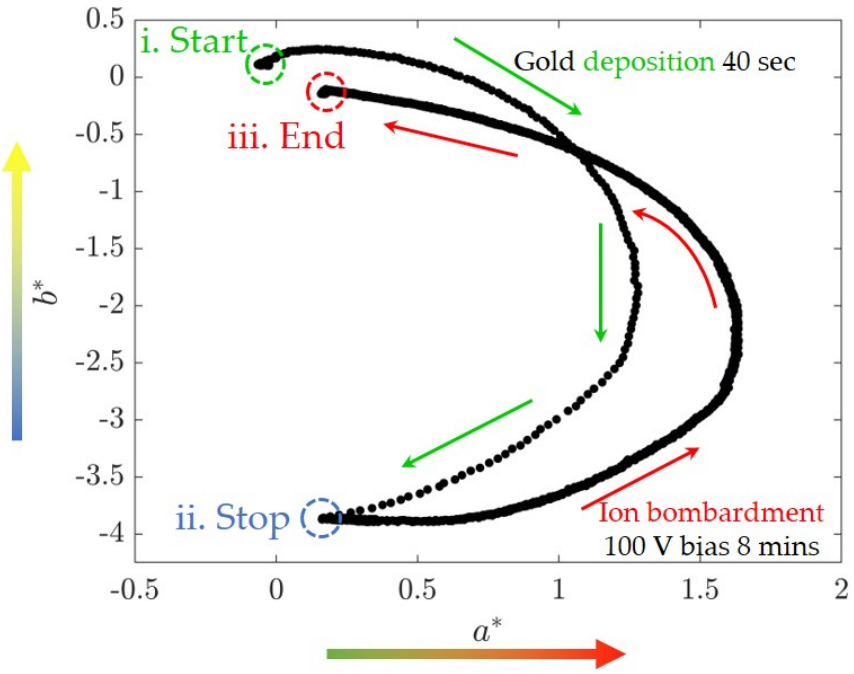

Figure 4.14 *In situ* color in reflection measurements in p polarization of a gold-island film on 20 nm Al_2O_3 seed layer during i) 40 s deposition, ii) interruption of the deposition and beginning of plasma etching at a -100 V self-bias value for 8 minutes and iii) end of etching.

During the gold film deposition, the reflected color evolves from a red to blue film, which is

expected from the previously presented experiments in this chapter. Once the deposition is finished, RF generator ignites a plasma and is set to maintain a substrate bias of -100 V. The etching lasted 8 mins after which the film's color parameter went back to color coordinate very close to what it was initially. One can notice that the color during etching exhibits a "color hysteresis", similar to what was observed by Netterfield and Martin [83].

In the context of coloration, such means to control the film's optical properties are particularly interesting. One can adjust *in situ* the color parameters after each thin film deposition. Moreover, the hue increases as the film are etched which suggests a beneficial effect in terms of microstructure, *i.e.* a more uniform size distribution. Indeed, Paszti *et al.* have observed a narrower size distribution due to the rapid disappearance of the smaller islands [76]. No quantitative data on the circularity or the aspect ratio of the islands could be found, unfortunately.

4.3.4 Ion bombardment and deposition on Orma

In the scope of this project, the ion bombardment and post-deposition etch can both be used to control the film's optical properties. The previous section has shown that the etching of a gold-island film can help to attain larger color hue parameters. Furthermore, at each deposition step, the optical monitoring system can track whenever the wanted parameter is attained or missed, which can be corrected with the use of ion irradiation. Obviously, this concept is not new but the growth of the plasmonic layers has not been *in situ* monitored in the context of color nor *in situ* coloration tuning by etching.

In situ transmission measurement reference of gold deposition on Orma would have been the proper way to explore the use of ion bombardment in a deposition process. This experiment thus serves as a proof of concept for the development of a multi-layered plasmonic stack.

During the deposition of two layers gold stack, the plasma unexpectedly died on the target (but the etching continued). This event is due to the two matching units interfering since two RF generators necessary to simultaneously sputter the target and generate a bias on the substrate. Notwithstanding this unfortunate occurrence, the deposition was resumed with apparently no ill effects. The initially aimed deposition time was 120 s which happens to be right before a kink in the saturation evolution curve (see Fig. 4.7) corresponding to a blue hue. It is interesting to note that there's practically no hysteresis as if a film deposited with ion bombardment didn't benefit from the extra ion irradiation.

The deposition of the second layer induces a substantial color shift of the sample which goes from $L^*a^*b^* = [93.7,\ 0.20,\ -0.62]$ to $[90.1,\ 1.22,\ -1.32]$.

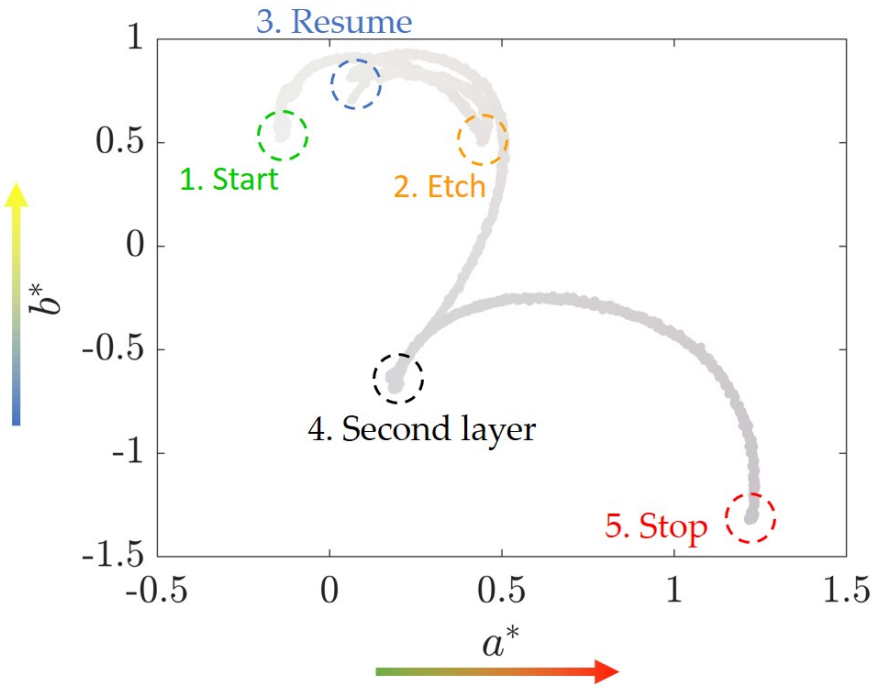

Figure 4.15 *In situ* transmission monitoring of gold deposition on a 20 nm alumina seed-layer with -200 V bias for 1) 41 s until plasma on the target shut down and the film was 2) etched for 69 s and deposition resumed for 3) 63 s thereafter. 4) A capping alumina layer of 20 nm was deposited before a second gold-island layer growth for 5) 120 s.

Despite the limited work conducted on this topic, *in situ* transmission monitoring has proven to be practical to rapidly explore the available color space especially considering the wealth of possibilities offered by plasmonic composites. The proposed methods thus offers a means to optimize a multi-layered optical film to generate a particular color.

CHAPTER 5 REFLECTIVITY MONITORING OF GOLD FILMS

In the previous chapter, colors were associated with the different growth stages presented in Sec. 2.3.6. In this chapter, the reflectivity of a growing gold film is studied to understand the microstructural changes attributed to the observed optical properties of a metal-island film. The effect of surface heating on the reflectivity evolution is explored to compare with room temperature (RT) experiment if the expected behavior, *i.e.* better surface diffusion and island growth promotion, can be predicted from the reflectivity spectra. The observations are confirmed with TEM imaging and the microstructural changes are linked with a shift of trend in the evolution of the reflectance. Then, the EMA models presented in Sec. 2.4.3 are tested. Lastly, general considerations are given to better the optical monitoring method.

5.1 Motivations

Since microstructure and optical properties are convoluted, a notable contrast of the optical behavior is expected from gold films at different growth stages which were previously presented in Sec. 2.3.6. Schwartzkopf *et al.*'s growth regimes model allows one to understand the evolution of the morphology throughout the deposition of the metal-island films. The authors have conducted *in-situ* reflectance in conjunction with their study of the X-ray scattering evolution of a gold film on polystyrene [72]. The authors have observed an initial decrease in the reflected intensity that they attributed to an increase in the surface roughness. Then, the average reflected light intensity increases linearly for wavelengths higher than $\lambda = 530$ nm which is reported as being around the typical SPR band of colloid gold clusters [136]. In Sec. 2.3.5, the reported SPR for hemispheric clusters found is slightly higher, around $\lambda = 575$ nm instead. Nonetheless, the authors note a localized reflectivity, associated with the SPR of the gold-island film that redshifts attributed to the growth stage II around these frequencies.

Furthermore, an anti-reflective behavior is observed at about an effective thickness of $\delta = 2.9$ nm. Grompf *et al.* made similar observations but for an effective thickness of $\delta = 3$ nm on silicon (covered by native oxide) [137]. The origin of this anomalous absorption was associated with the emergence of a branched domain, *i.e.* growth stage III, and is caused by the coupling of the smaller islands with large aggregates as explained in Sec. 2.4.7. Moreover, no clear delimitations of the different regime transitions were observed from the surface reflectance spectroscopy data alone.

This study aims at identifying growth stage transitions from reflectivity measurement during

deposition solely. While *in situ* X-ray scattering measurement has proven to be an excellent method to characterize the growth of metal-island films, it is not readily accessible. In contrast, a white light source and a spectrometer are affordable and easy to install on a deposition system.

Important morphological changes emerge as islands increase of size. The most significant one arises from partial coalescence which causes elongated islands to form and, at a later growth stage, a branched structure (see Sec. 2.3.4). This size-dependent effect can be delayed by enhancing surface diffusion with increased substrate temperature (see Sec. 2.3.3).

The previous chapter has demonstrated the utility of *in situ* optical monitoring to rapidly explore the color space accessible with a plasmonic layer. The scope of this work here is to gain a deeper understanding of the processes involved in order to better optimize a future fabrication process involving this type of film from *in situ* reflectivity monitoring.

5.2 Evolution of the reflectivity

To better explore the wealth of possibilities offered by plasmonic materials for color generation, an *in situ* optical monitoring system, previously introduced in Sec. 3.2.4, was used to track a change in the optical behavior and understand how to optimize the surface plasmon resonance for a given deposition condition. Reflection spectra, obtained *in situ*, for different effective thicknesses, are shown in Fig. 5.1 and compared with spectra of theoretical continuous layers of equivalent effective thicknesses (see Sec. 3.2.5).

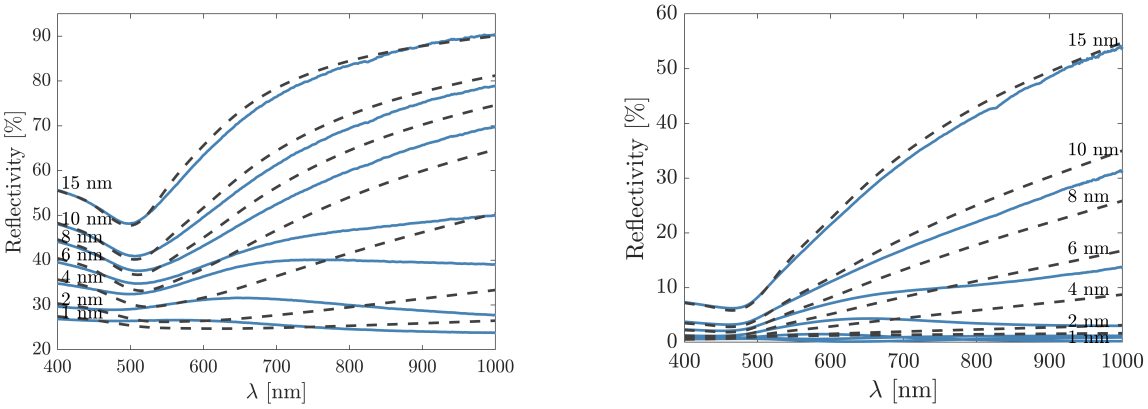

(a) *s*-polarization (b) *p*-polarization

Figure 5.1 *In situ* reflectivity (solid blue lines) and theoretical reflectivity curves (black dashed lines) of gold deposited at room temperature on B270 glass with a 20 nm SiO_2 seed layer for *s*- and *p*-polarization.

One can note, as expected, that the experimental data differs widely from the theoretical curves until the film becomes continuous. Most importantly, the high reflectivity observed in the continuous films for wavelengths above 700 nm is absent due to the lack of conducting electrons (Drude component). Around $\delta = 10$ nm the match between experimental and theoretical curves is much closer indicating that a bulk-like behavior has been reached. A simple analysis of the reflectivity is thus sufficient to highlight important changes in the film growth. However, changes of regime before the film becomes conductive cannot be highlighted by simply comparing the experimental curves to the theoretical ones. Although, knowing the effect of the variation of a deposition parameter on the growth, one can associate similar features of a reflected spectrum with a specific morphology.

5.2.1 Impact of the temperature

The same experiments were performed for a 100° and 200°C surface temperature, but only for *s*-polarization, and are presented in Fig. 5.2. The choice of investigating only *s*-polarization will be further explained in the following section but it can mainly be attributed to the significantly higher reflected intensity. Indeed, at the angle of 65°, the intensity of *p*-pol. is weaker due to light's angle of incidence being close to the Brewster angle θ_b of the borosilicate substrate. This angle is defined as $\theta_b = \tan^{-1}(n_2/n_1)$, with n_1 and n_2 the refractive indexes of the incident medium and the substrate respectively [84].

The expected impact of raising the temperature is higher island mobility and a delayed partial coalescence onset which favors the growth of bigger islands compared to deposition at RT [25]. At 100°C, the theoretical curve fit with experimental data is very good for $\delta = 20$ nm, twice as much comparatively with the RT film. For the film deposited at 200°, no satisfactory fit is attained and this divergence is attributed to the high surface roughness of the film and not that of a discontinuous film which gives it the appearance of a "smoky" mirror. The grain size of the film has is comparable with the wavelength of light, inducing light scattering. The temperature effect on grain growth can be understood according to Thornton's structure zone model [138]. To briefly resume the model, a higher temperature will promote grain boundary and dislocation mobility, *i.e.* bulk diffusion. Surface faceting is a by-product of the recrystallization and grain growth becomes increasingly important for temperatures closer to the melting point of the magnetron sputtered material.

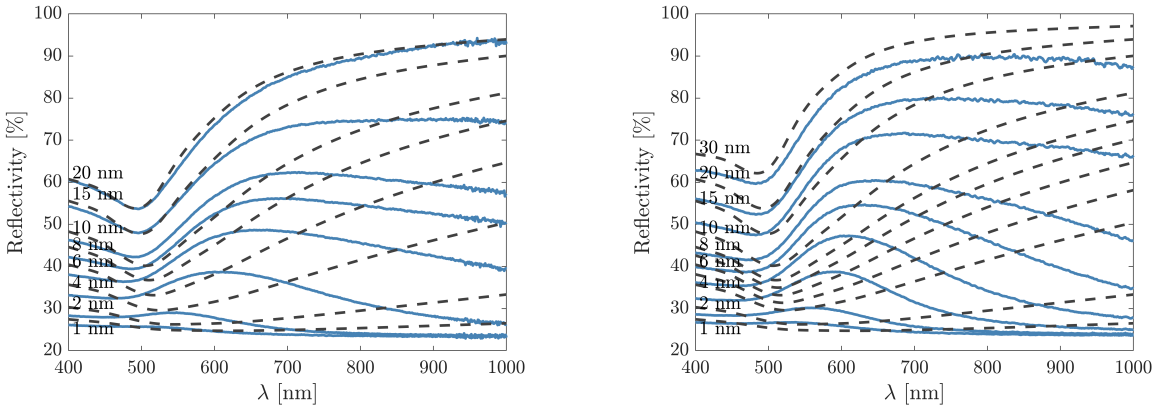

(a) 100°C (b) 200°C

Figure 5.2 *In situ* reflectivity (solid blue lines) and theoretical reflectivity curves (dashed black lines) of gold deposited at different temperatures on B270 glass with 20 nm SiO_2 seed layer for *s*-polarization.

5.2.2 Reflectivity evolution trends

The evolution profile of the reflectivity at the three deposition temperature is presented in Fig. 5.3 for just one wavelength to simplify the visualization of the films' growth behavior. Two kinks in the curves for RT and 100° are visible, whereas at 200°C only one is clearly defined.

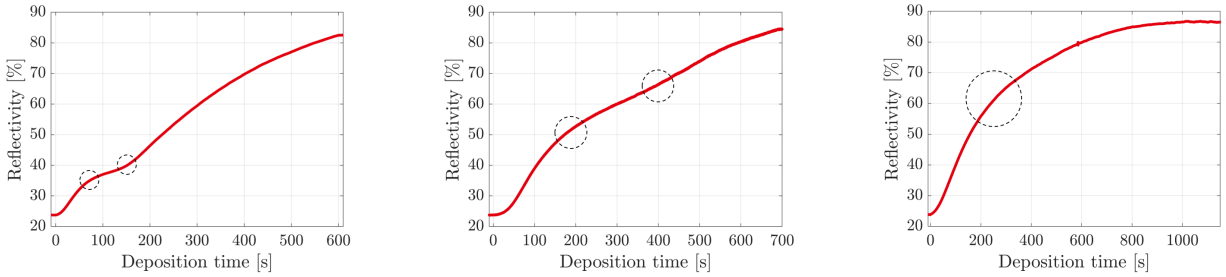

(a) Room temperature (b) 100°C (c) 200°C

Figure 5.3 Evolution of *s*-polarization reflected intensity at $\lambda = 600$ nm for each temperature condition as identified from the *in situ* reflectivity measurements. The dashed circles highlight kinks in the curves.

The presence of similar trend changes in the evolution of the reflected intensity for the RT and 100°C films is of interest to associate morphological changes from the time-resolved reflectivity behavior. Moreover, the absence of a second change of trend for the 200°C should

be further investigated with the help of electron microscopy in the following section.

5.3 TEM observations

The evolution at each wavelength is further presented and analyzed. For now, the objective is to demonstrate a correlation between change of trend with the reflected intensity evolution and growth stages. To do so, six films were deposited at RT for different deposition times. QCM measurements were validated with *in situ* the measurements of the reflected intensity as shown in Fig. 5.4. First, a gold film is deposited until a thick (> 30 nm) continuous layer is obtained. The thickness is evaluated from ellipsometric measurements on borosilicate glass and silicon substrates (see Fig. A.1). *In situ* reflectivity monitoring is done throughout the deposition on the glass and it allows one to obtain the real deposition time down to 125 ms of precision. Furthermore, it serves to validate that the island films deposited for TEM imaging are of the expected effective thickness, *i.e.* when the spectra match.

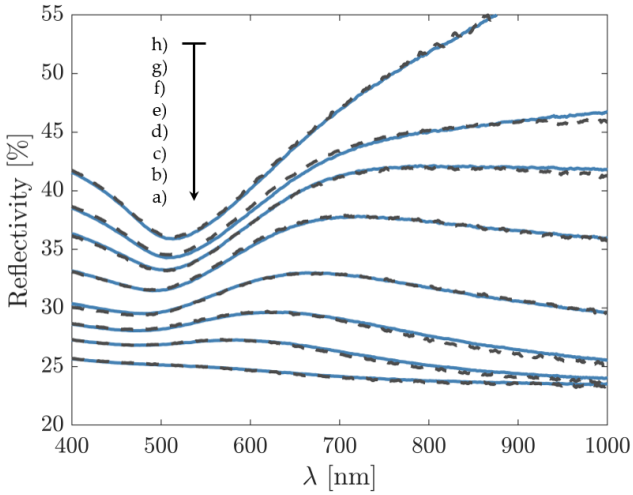

Figure 5.4 Reflectivity spectra of thin gold-film on B270 substrates with a 10 nm SiO_2 seed layer at room temperature. Each spectrum of the thin film deposited (dashed black lines) are fitted with spectra from the *in situ* monitoring of the think film characterized by ellipsometry measurements (solid blue lines). The corresponding effective thicknesses of the thin-films are: a) 0.5, b) 1.0, c) 1.4, d) 2.0, e) 2.9, f) 3.9, g) 4.9, and h) 5.9 nm.

The measured thicknesses from *in situ* reflectivity spectra are, on average, -3% lower than the QCM measurements.

5.3.1 Room temperature

The different regimes can be summarized as follow: (i) nucleation and growth of isolated hemispherical islands that transition into a (ii) partial coalescence of islands until (iii) a branched domain of large aggregates is formed and (iv) percolates before becoming continuous as the voids are progressively filled as described in Sec. 2.3.6.

The extinction and reflectivity spectra of the deposited films at room temperature are presented in Fig. 5.5 and the corresponding TEM observation in Fig. 5.6. The arrows in Fig. 5.5a serves to guide the viewer as to what is of interest in terms of optical behavior. First, a LSPR peak redshifting can be observed from 0.5 until 2.0 nm (arrow 1.). Past this point, the films e)-f) exhibit the "anomalous" absorption reported in the literature as seen in Sec. 2.4.7 (arrow 2.). A maximum of absorption in the NIR is reached at the film of 2.9 nm equivalent thickness which is consistent with Grompf *et al.*'s finding.

In contrast, the reflected intensity at 65° shows a preferential reflection peak, attributed to LSPR, visible until $\delta = 2.9$ nm. Moreover, a rapid gain in NIR reflectivity becomes considerable around the onset of the anomalous absorption. However, no clearly visible changes of behavior are qualitatively observable other than the redshifting peak at the lower effective thicknesses for the reflected spectra from Fig. 5.5b.

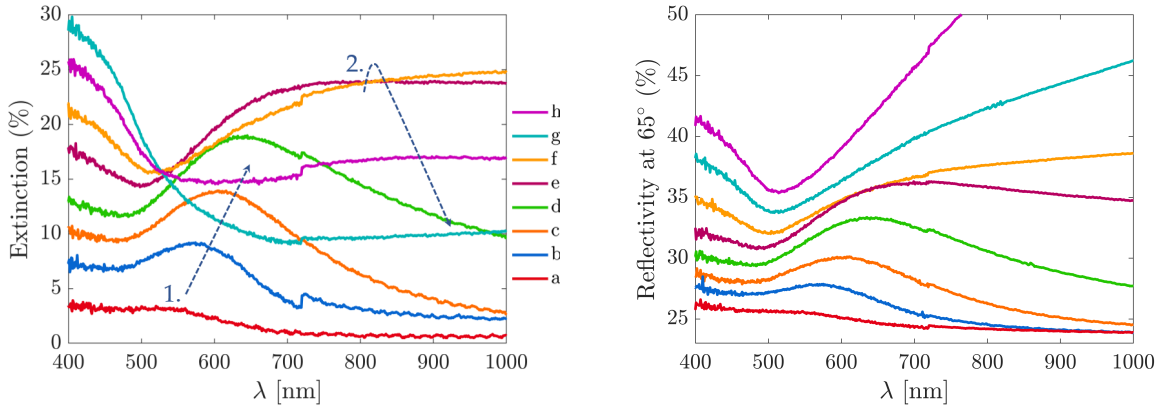

(a) (b)

Figure 5.5 *Ex situ* a) extinction at 6° and b) reflectivity at 65° measurements of gold films deposited with SiO_2 seed layer and B270 substrates at room temperature. The equivalent thicknesses are: a) 0.5, b) 1.0, c) 1.4, d) 2.0, e) 2.9, f) 3.9, g) 4.9, and h) 5.9 nm.

Observation of the TEM images of the films, presented in Fig. 5.6, allows one to associate the redshifting of the peak with isolated islands increase of size for the films a)-d). From b) to d), nearly all islands have coalesced, suggesting that this behavior is attributable

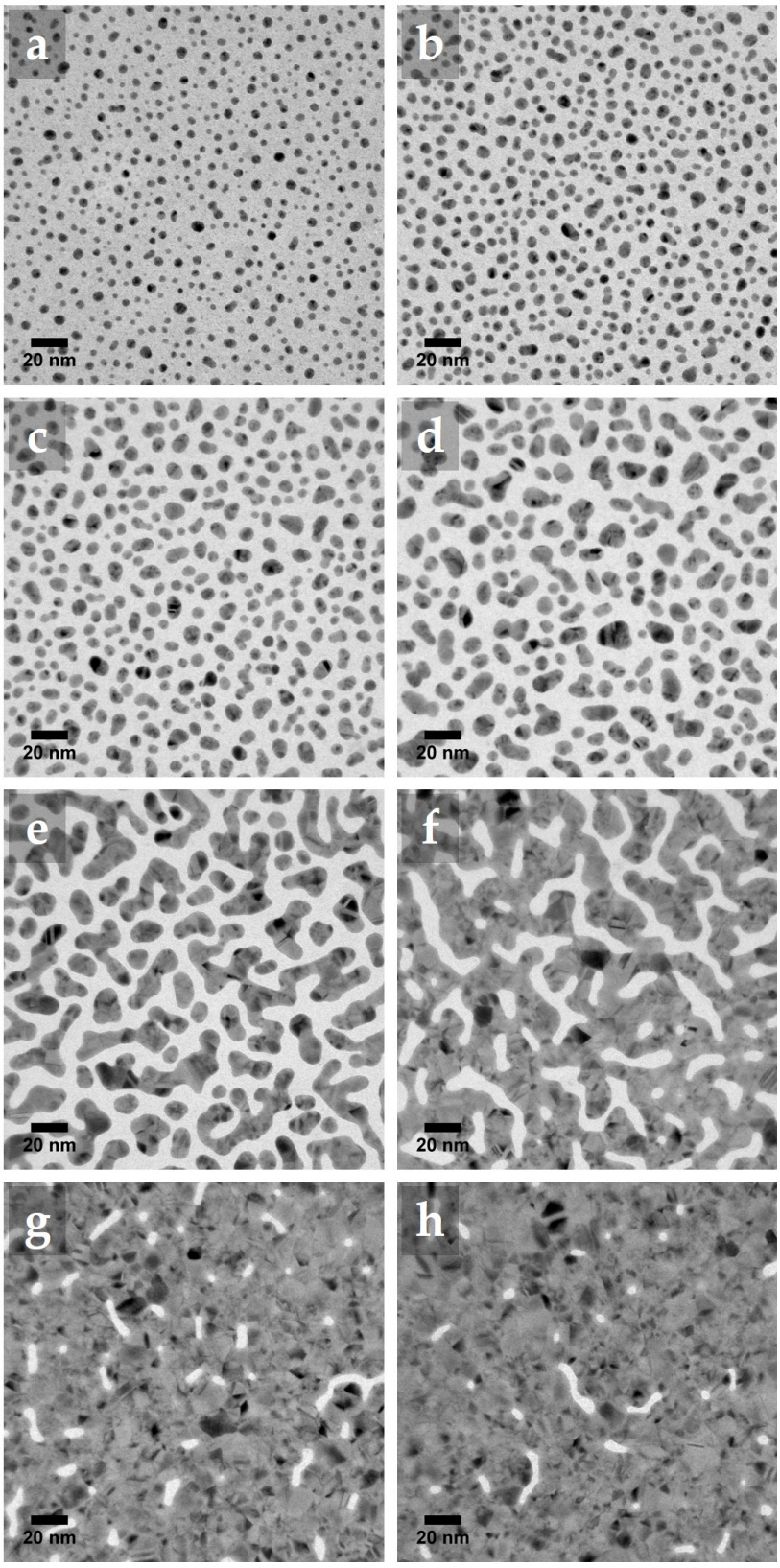

Figure 5.6 TEM imaging of thin gold-film on SiN membranes deposited at room temperature for a) 0.5, b) 1.0, c) 1.4, d) 2.0, e) 2.9, f) 3.9, g) 4.9, and h) 5.9 nm.

to the growth stage II. Whereas for the film a), very few partially coalesced islands are visible. The coverage of this film is 16% and the first growth stage is expected to end for coverage of just 25% but this reported value from Schwartzkopf *et al.* was attributed with an effective thickness of $\delta = 0.27$ nm [32]. This growth stage basically corresponds to the presented kinetics model in Sec. 2.3.2 where the island density rapidly rises before decreasing as the adatom concentration plummet. One can conclude that the onset of the partial coalescence growth regime is very close to the film a) effective thickness. Furthermore, the beginning of this growth stage can be associated with a gain in reflectivity for $\lambda > 700$ nm.

The analysis of the size and shape distribution of the films are shown in Fig. 5.7 and it is obvious that the 2.9 nm has a morphology quite different from the other films. The significant increase of the average island area is quite telling. This point corresponds to the coverage threshold where islands act similarly to what's predicted with the FMM (see Sec. 2.3.4), *i.e.* close to percolation, the islands form elongated aggregates due to the complete interruption of the coalescence process, *i.e.* the domain coarsening (III) growth stage.

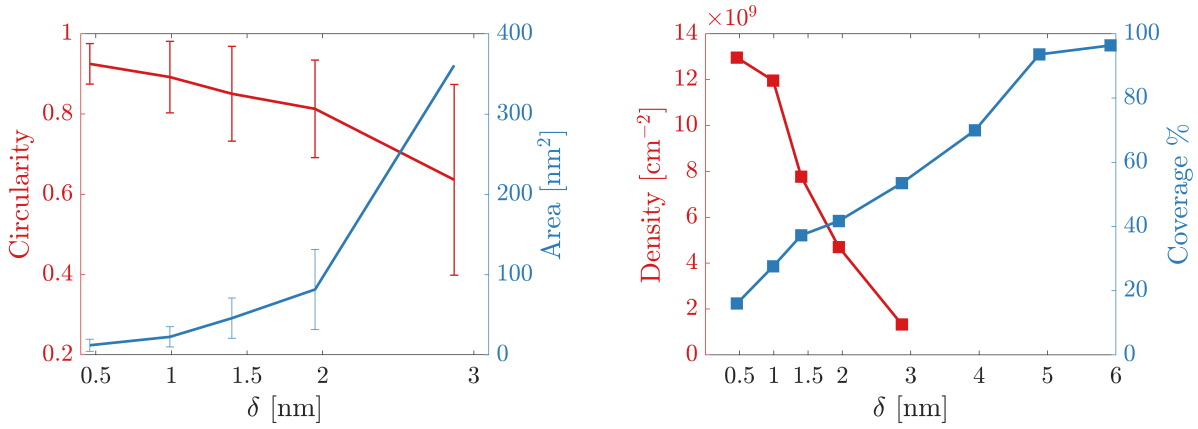

(a) Average circularity and island area.

(b) Coverage and density of the islands.

Figure 5.7 Left: circularity (red) and mean area size (blue) of the island-films for δ from 0.5 to 3 nm (6 nm for the coverage). The 3 nm film size distribution was no longer normal and the larger standard deviation than the mean was left out. Right: coverage of the gold on the surface and density of the islands. The data was extracted from the analysis of the films presented in Fig. 5.6.

Hovel *et al.* have associated a sharp gain in reflectivity past the percolation threshold [119]. This threshold is attributed with the formation of a continuous network and characterized by a rapid gain of conductivity; the film transitions from an insulator to a conductor. As a result, subsequent deposition is characterized by a rapid gain in reflectivity from the NIR

toward shorter wavelengths as the film becomes bulk-like. In the current case, the 3.94 nm effective thickness film is percolated.

5.3.2 High temperatures

For the higher temperatures, 4 and 3 films were deposited at 100° and 200°C respectively. The same precautions were taken, *i.e.* association of each spectrum at the end of the deposition with the *in situ* island-to-continuous film with one notable difference for the 200°C for which the deposition rate was calibrated from the QCM reading instead of ellipsometry measurements that were impossible to properly do due to the scattering.

At 100°, similar behavior is observed compared to deposition at RT, *i.e.* a redshifting SPR peak transitions into an anomalously absorbing layer as shown in Fig. 5.8. TEM images of the films, presented in Fig. 5.9, confirm that the branched structure is indeed related to the aforementioned high absorption in the NIR. As expected, the absorption peak is narrower, has a higher amplitude and is still well defined at 4.3 nm. Moreover, greater selectivity in reflectivity is observed centered around 584, 630 and 664 nm for the 2.8, 4.3 and 6.4 nm films respectively. In comparison, the RT film hardly has any selective reflectivity at 0.46 nm but clear peaks are visible at 575, 608 and 641 nm for the 1.0, 1.4 and 2 nm films in order.

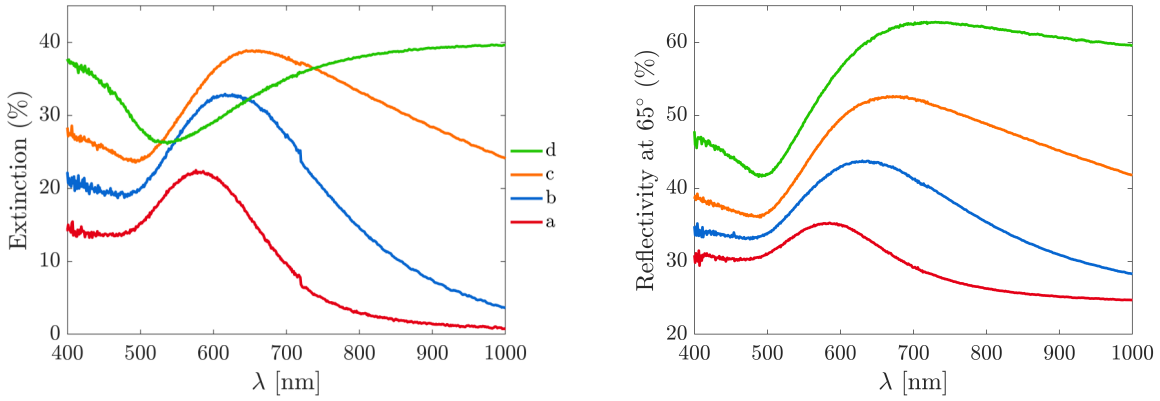

(a) (b)

Figure 5.8 *Ex situ* a) extinction at 6° and b) reflectivity at 65° measurements of gold films deposited with SiO_2 seed layer and B270 substrates at 100°C. The equivalent thicknesses are: a) 2.8, b) 4.3, c) 6.4, and d) 11.4 nm.

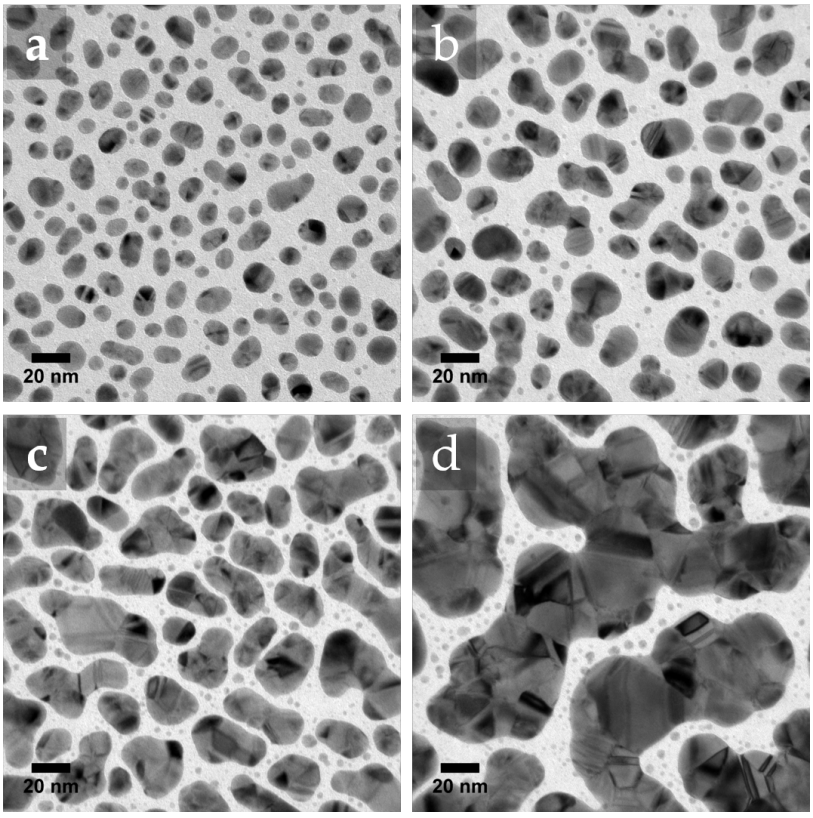

Figure 5.9 TEM imaging of thin gold-film on SiN membranes with SiO_2 seed-layer deposited at 100°C for a) 2.8, b) 4.3, c) 6.4, & d) 11.4 nm.

The films deposited at 200°C have a SPR peak respectively at 566, 576 and 659 nm for the 3.0, 4.0 and 10.0 nm effective thicknesses as shown in Fig. 5.10. The corresponding TEM images in Fig. 5.11 reveals that up to 10 nm, the film is still of isolated islands. Moreover, the clusters are much more faceted than any other film previously observed, a clear indication that recrystallization allows the reorganization of the coalescing islands.

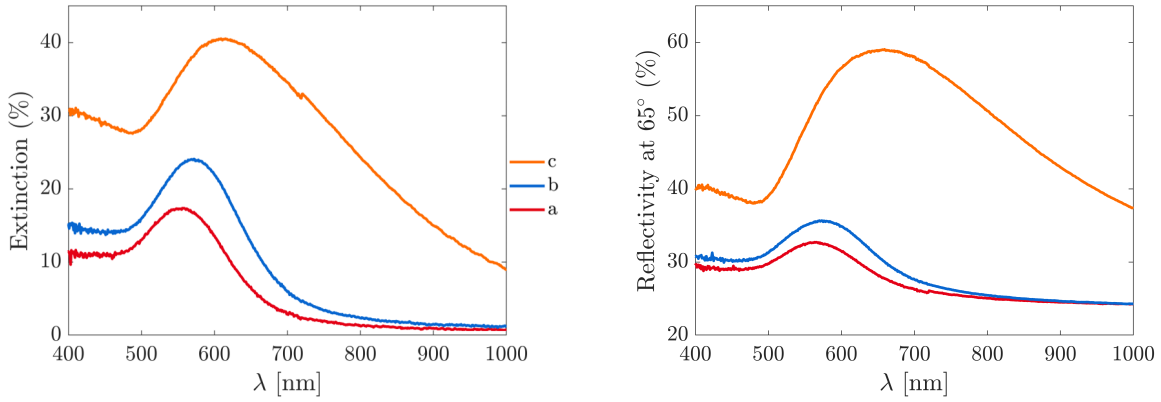

(a) (b)

Figure 5.10 *Ex situ* a) extinction at 6° and b) reflectivity at 65° measurements of gold films deposited with SiO_2 seed layer and B270 substrates at 200°C. The equivalent thicknesses are: a) 3.0, b) 4.0, and c) 10.0 nm.

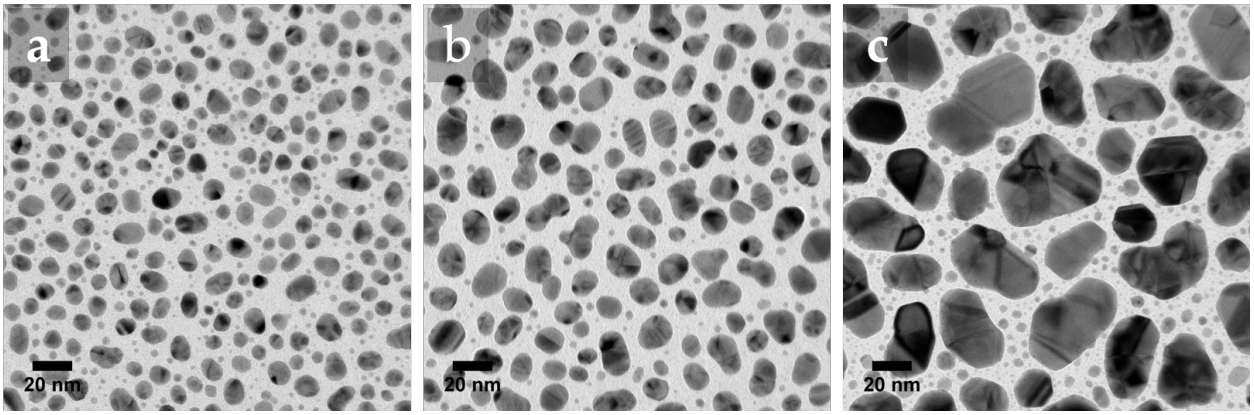

Figure 5.11 TEM imaging of thin gold-film on SiN membranes with SiO_2 seed-layer deposited at 200°C for: a) 2.9, b) 4.0, & c) 9.9 nm.

From these results, one can conclude that the onset of the branched domain (III) growth stage is significantly delayed with increased surface temperature. Each temperature condition reveals an initially redshifting SPR peak. For the RT and 100°C conditions, the two kinks in the evolution of the reflectivity at 600 nm (see Fig. 5.3) appear to indeed be related with morphological changes. Not enough sample were deposited for the 200°C to observe the structure associated with anomalous absorption in the NIR. However, from the evolution of the reflectivity curve (Fig. 5.3c), it is hypothesized that this structure is never attained.

This hypothesis is strengthened with the analysis of the island population distribution of the films shown in Fig. 5.12. Indeed, the 100°C films exhibit a sharp increase in the average surface area from 4.3 to 6.4 nm whereas the 200°C films do not follow the same trend as it appears to reach a plateau. Interestingly, no dip in the average circularity is apparent at 100°C contrarily to what was observed with the RT films.

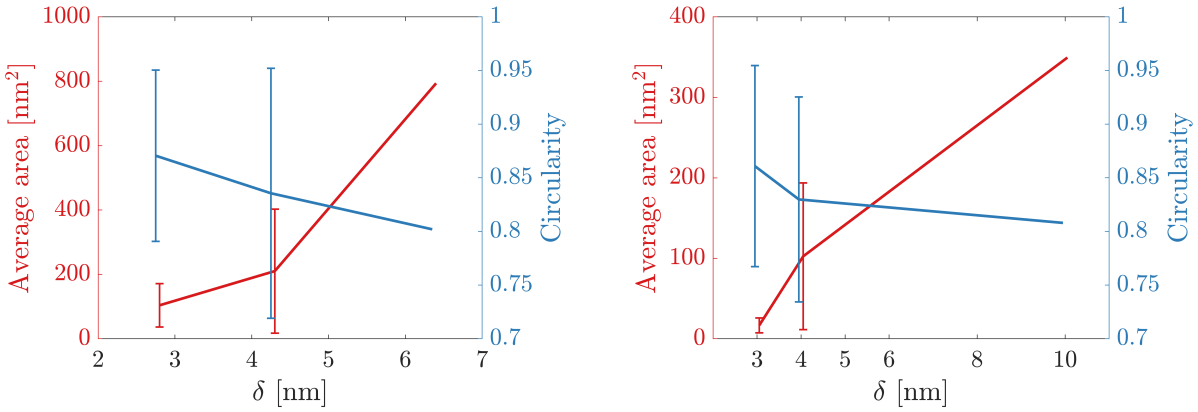

(a) 100°C (b) 200°C

Figure 5.12 Circularity (red) and mean island area size (blue) of the island-films for all a) 100° (except the 11.4 nm) and b) 200°C films. The 6.4 nm at 100°C and 10 nm at 200°C films size distribution were no longer normal and the larger standard deviation than the mean was left out. The data were extracted from the analysis of the films presented in Fig. 5.9 and 5.11.

5.4 Time derivative surface reflectance

In the context of the growth of noble metals, as the deposition progresses, the mean islands' size increases and, in the case of Au, a well-defined absorption peak red-shifts from approximately $\lambda \approx 500$ nm to $\lambda \approx 600$ nm [139]. Evolution of the reflectivity at 600 nm in Fig. 5.3 has revealed changes of a trend which appear related to the evolution of the film's morphology. Hence, calculating the time derivative of the reflectance can amplify these subtle changes and hopefully, be attributed to different growth stages.

5.4.1 Room temperature

The Fig. 5.13 presents the *s*-polarization reflectivity rate of change (RRC), *i.e.* the slope of the reflectivity intensity curve at various wavelengths.

One can note a peak for each wavelength from 400 to 1000 nm at increasingly higher effective

thicknesses until a decrease of the RRC. Looking at the TEM images, the isolated island structure (0.5-2 nm) coincides with a rapidly rising reflectivity of redshifting wavelengths. Then, the 2.9 and 3.9 nm films are associated with a slowing gain of reflectivity at all wavelengths and have a branched domain morphology. Past percolation, the growth of the conductive film is accompanied by a sharp gain in reflectivity.

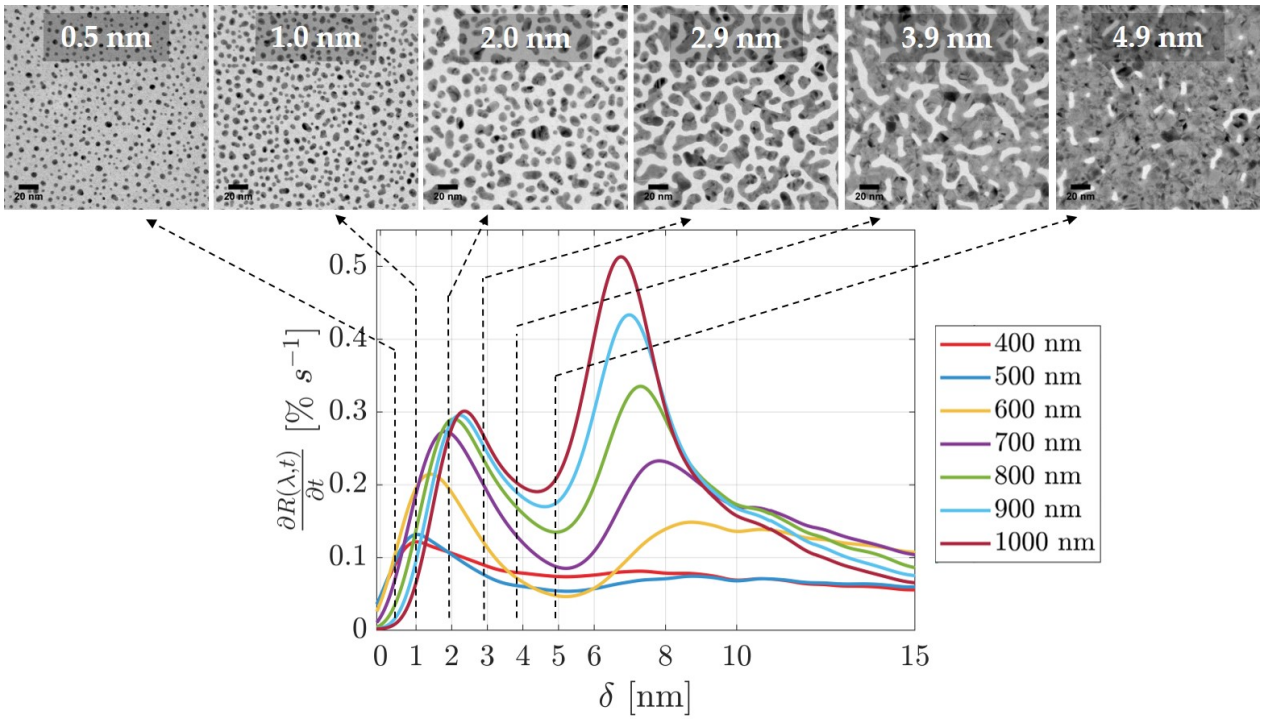

Figure 5.13 Time derivative surface reflectance of the *s*-polarization reflectivity data of gold film deposited at room temperature. TEM images of films corresponding to each deposition time is shown to accommodate the viewer.

For the *p*-polarization, an initial decrease of the reflected intensity is observed. This behavior can be understood as a plasmonic pseudo-Brewster angle [2]. Radiating dipoles can only emit perpendicularly to their dipole moment. As such, *p*-polarization is preferentially transmitted whereas a gain of reflectivity is observed for *s*-polarization instead. Again, a peak redshifting toward greater effective thicknesses is coherent with islands increasing of size. Around the percolation threshold, the change of reflectivity becomes positive. Past-percolation, a sharp gain of reflectivity is observed, similarly to *s*-polarization.

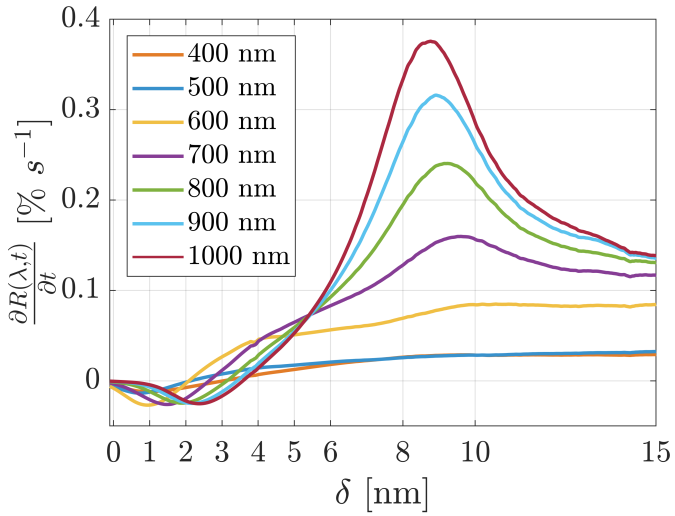

Figure 5.14 Time derivative reflectance of the *p*-polarization reflectivity data of gold film deposited at room temperature.

The peak characteristics of the time derivative reflectance for both polarization are presented in Fig. 5.15 and attributed to the isolated island morphology growth stage, based on the TEM imaging.

During the growth of the islands, an increased size is expected to red-shift the LSPR peak. Fig. 5.15a shows that the maximal gain of reflectivity for *s*-polarization is progressively higher the longer the wavelength until it caps at around 2 nm for $\lambda > 730$ nm. Similar observation can be made for *p*-polarization (Fig. 5.15b) were the maximum decrease of reflected light remains relatively constant past 730 nm. However, a minimum at 630 nm at an effective thickness of 1.1 nm shows that both polarizations do not follow the same trend, *i.e.* the absolute value of the RRC increases the longer the wavelength. This small kink in the curve likely corresponds to a growth sub-stage of the partial coalescence (ii) regime [72] where the island aspect ratio starts to decrease considerably. Indeed, the *p*-polarization field is within the optical plane so that it's affected by vertical and parallel characteristics of the island film morphology. The field's component perpendicular to the sample's surface contributes more weakly to the peak although [140]. This effect is absent for *s*-polarization since the electric field is perpendicular to the optical plane. Hence, LSPR can only be excited in the plane parallel to surface which provides higher sensitivity and more insight to interpret the observed changes in the evolution of the reflectivity. Moreover, Schwartzkopf and co-workers have found that the start of lateral growth is around $\delta = 1.33$ nm, close to our finding. Lastly, the high gain transition shifting to longer wavelengths is coherent with a coalescence driven growth regime [30, 112, 114].

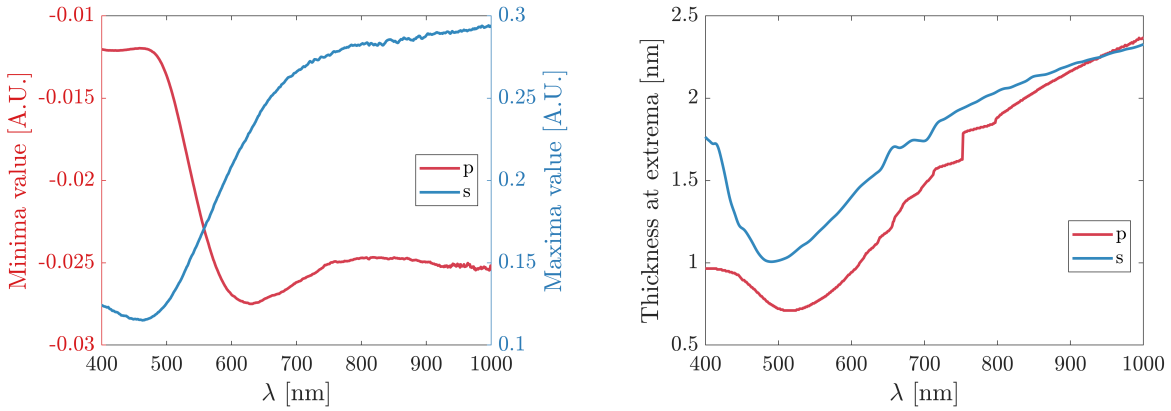

(a) Amplitude of the peak.

(b) Corresponding thickness of the peak.

Figure 5.15 Extraction of the time derivative reflectance peak characteristics: (a) amplitude and (b) corresponding effective thicknesses when it occurs.

Already at 0.5 nm, partially coalesced islands are visible but most islands are round and isolated. Around 1 nm, a local maxima for $\lambda = 500$ nm is reached (fig.5.15a) and past this thickness, a significant island density decreases, indicating that most islands have coalesced which results in a film exhibiting elongated clusters shape at 1.4 nm. In light of this observation, the first phase of growth ends right before the first time derivative peak effective value, in this case, $\lambda = 500$ nm at $\delta = 1$ nm. Subsequent deposition shows a marked increase in island surface area and a decrease of circularity in Fig. 5.7 past $\delta = 2$ nm. This shift in morphology is accompanied by a decrease of the RRC for all wavelengths as previously discussed. The 3.9 nm film is percolated and a sudden change of trend of the RRC reflects the onset of the third phase.

From the time derivative reflectance data, one can conclude, in conjunction with the TEM observations, that a regime transition between $\delta = 2$ and 3 nm is consistent with the onset of the branched-domain (iii) structure. Another transition is observed at about $\delta = 4$ nm which corresponds to the formation of a conductive network (iv). Finally, the stable RRC at for $\delta \approx 10$ nm is associated with a continuous layer growth. This last assumption can be validated by looking at the reflectivity measurements which are in good agreement with the theoretical curves only until $\delta = 10$ nm, especially for the *p*-polarization spectra. For the lower effective thicknesses, a rapid gain of reflectivity at 1 nm for the longer wavelengths is synonymous with islands becoming elongated attributed to the coalescence regime (ii).

We propose a theoretical explanation for the change of RCC regime that can be understood considering a film that is initially 2D array of resonators transitioning into a hole array film. Nanoislands behave as resonator, concentrating far-field energy into strong locally enhanced

field. For a structure with inversion symmetry, only the lower (dipole) mode can couple with the external field which can decay radiatively and non-radiatively [141]. If two particles are in close proximity it's possible that a dipole mode couples with the other particle's higher modes, which can only decay non-radiatively [114] and contribute to the anomalous dubbed absorption. Since higher mode volume is much smaller than that of the dipole one, an optimal distance exists where the dipole mode can be out-coupled.

5.4.2 High temperatures

The analysis will be limited to *s*-polarization henceforth due to the higher signal intensity and electrical field component parallel to the surface which simplifies the analysis. The time derivative of the *s*-polarization reflected intensity for 100° and 200° C are shown in Fig. 5.16.

Two key differences from the room temperature reflectivity evolution can be drawn: 1. the higher temperature has shifted the initial characteristic peaks that were previously associated with a growth regime transition and 2. the 200°C temperature condition lacks a second peak which was determined to arise right after the percolation of the film. The onset of partial coalescence depends on the surface mobility of the atoms so a higher surface temperature is expected to delay this growth stage, a satisfactory explanation for the shifted peaks position. The lack of apparent transition from isolated islands to continuous film at 200°C can be attributed to the absence of isolated islands surrounded by a conductive network.

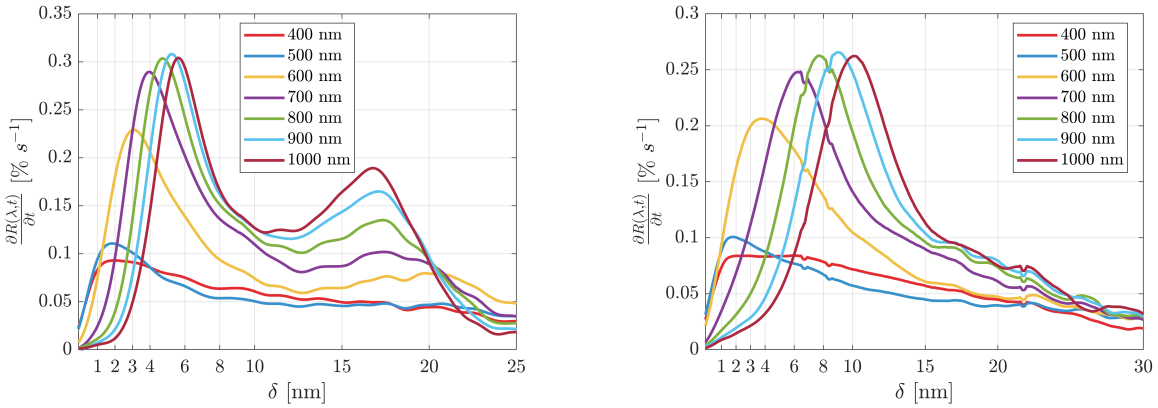

(a) 100°C (b) 200°C

Figure 5.16 *s*-polarization TDSR for gold deposited at high temperature on B270 glass substrate with 10 nm SiO_2 seed layer.

This finding suggests that, as the islands (or crystals) touch each other at 200° C, the atoms have enough mobility to diffuse and reorganize as a bigger crystal. Thus, the ICM is not valid at this temperature and no coalescence interruption is observed, *i.e.* no branched domain.

Looking strictly at the peaks' amplitude and position in Fig. 5.17 and 5.18 for 100° and 200°C respectively, the thickness at maximum for $\lambda = 500$ nm is 1.8 and 2.2 nm respectively. The peak redshifts until it reaches $\lambda = 1000$ nm at 5.6 nm for 100° and 10 nm for 200°C. Room temperature deposition had an interval much narrower, *i.e.* 1.1 to 2.3 nm (see Fig. 5.15).

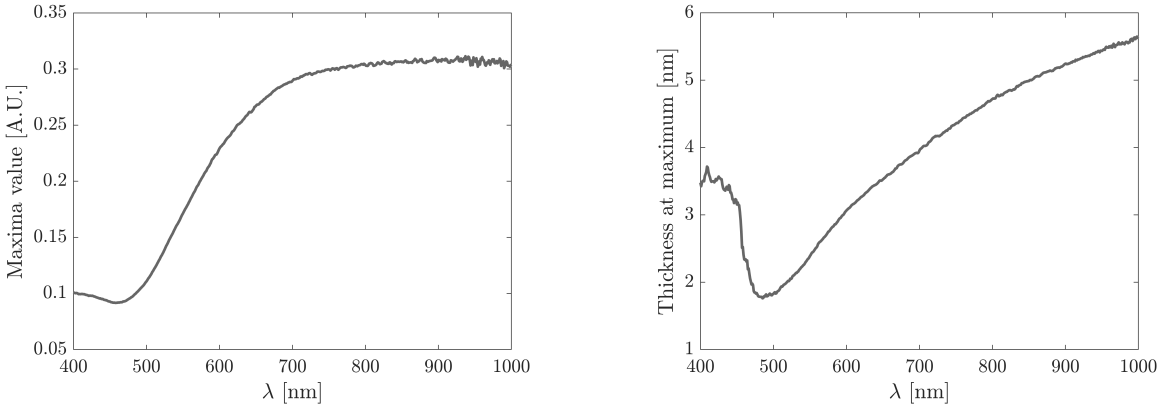

(a) Amplitude of the peak. (b) Corresponding thickness of the peak.

Figure 5.17 Extraction of the time derivative *s*-polarization reflectance peak characteristics for the 100°C film: (a) amplitude and (b) corresponding effective thicknesses when it occurs.

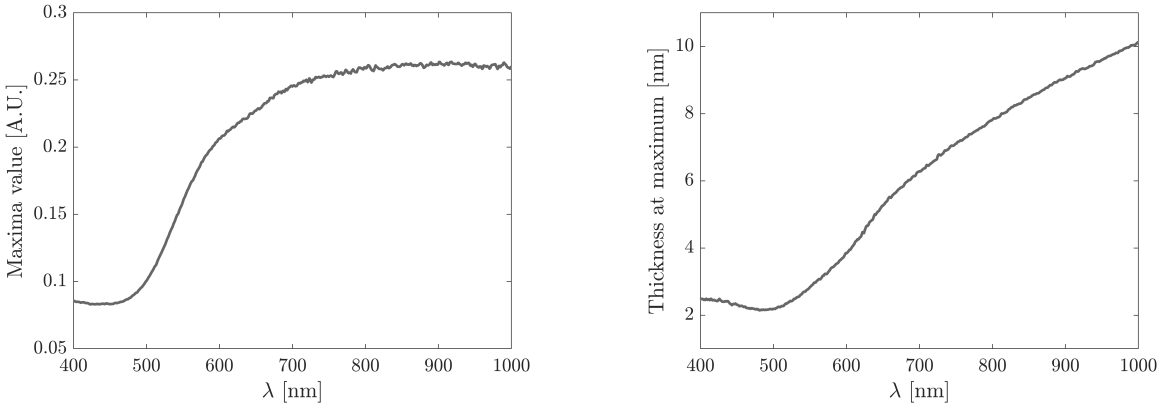

(a) Amplitude of the peak. (b) Corresponding thickness of the peak.

Figure 5.18 Extraction of the time derivative *s*-polarization reflectance peak characteristics for the 200°C film: (a) amplitude and (b) corresponding effective thicknesses when it occurs.

It was determined from TEM images that a transition from the growth stage II and III happened between 2 and 2.9 nm. For the 100°C film, it means that the 6.4 nm film has transitioned into a branched structure which is corroborated with the TEM imaging (see Fig. 5.12).

In summary, studying the time derivative of *in situ* reflectivity measurements of a growing gold film was associated with characteristic optical behavior. The redshifting selective reflectivity peak during the partial coalescence growth stage corresponded to a rapid increase of the signal intensity at an increasingly longer wavelength and thicker effective thickness. This stage ends at the onset of the formation of a branched structure which is known for its high absorption in the NIR. This effect results in a decrease in the reflectivity rate of change for the *s*-polarization. After the film percolates, a sharp gain in reflectivity for the longer wavelengths is observed. This behavior could not be attributed to the 200°C deposition condition. The hypothesis to explain the disparity with the lower temperature deposition is the lack of a branched domain structure, the islands grow and percolate when the film becomes continuous.

5.5 Modeling

Using the MG and BM models, it was not possible to extract parameters that correspond to the expected values. Moreover, using the coverage obtained from TEM observation, the models did not output physically coherent results which can be attributed to the fact that the islands are hemispherical. Four gold films are presented in Fig. 5.19 to reflect this finding. The films were selected because they exhibited in the first case (red) isolated islands with a well defined absorption peak and the second (blue) a film at the percolation growth stage.

For the MG model (dash-dot), the low and high effective thicknesses of the fitted depolarization factor are 0.33 and 0 respectively. The 0.33 value corresponds to a spherical inclusion whereas the 0 is of a thin film. In both cases, the model is very far from the experimental data. The BM model fares better with a peak nearly identical for the lower effective thickness films and transmission spectra relatively close to that of the experimental ones. However, the model effective film thickness output is a value that is difficult to interpret. The depolarization factor is higher for the thicker films and corresponds to elongated particles. A characterization technique such as XRR could provide information on the effective electron density to corroborate with the BG model [88].

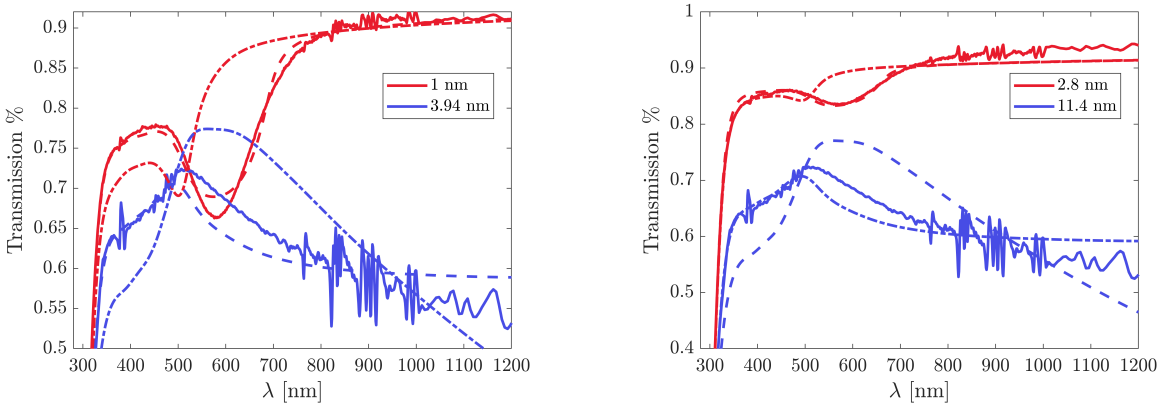

(a) Room temperature (b) 100°C

Figure 5.19 The experimental data (solid) fit for gold films with the MG (dashed-dot) and BM (dashed) models with filling factor provided from TEM imaging. BM fitting thicknesses/depolarization factor for the a) room temperature 3.31 nm / 0.627 and 6.37 nm / 0.698 for 1 and 3.94 nm respectively and the b) 100° films (2.8 and 11.4 nm in order) 7.57 nm / 0.737 and 14.07 nm / 0.865.

5.6 General considerations

One major issue with the time derivative method shown here is that the correlation of changes in the reflectivity evolution is only done via *ex situ* measurements and using the rich literature offering a broad theoretical background surrounding the growth of metal-island films. It is particularly problematic for heated substrates as they require multiple-hours long cool-down before they can be safely handled. To prevent morphology of the films to change, argon flow is introduced in the system to speed up the cooling but it is obvious that some Ostwald ripening occurs nonetheless. To avoid this problem, one could use conductivity measurements of the film inside of the chamber to associate optical changes of trend with the final growth stage transition (III to IV). Hafezian *et al.* have used *in situ* conductivity measurements to associate the extinction of *p*-polarization intensity with the percolation threshold using *in situ* ellipsometry [142]. The same principle could be applied here.

The time derivative is very sensible to the signal noise. The high acquisition rate mitigates to some extent this problem. However, the peaks' amplitude are attenuated and sudden changes in the reflectivity (when the deposition start for example) become less pronounced after the smoothing process. Furthermore, the time derivative data becomes especially noisy at the end of the deposition when the film is continuous. The origin of the noise contribution has not been investigated exhaustively. Vibrations were attenuated as much as possible but

the presence of loud and vibrating vacuum pumps in proximity contributed to low-frequency noise. The emission from the plasma can also pollute the signal but it is expected to be high-frequency noise and easily filtrated.

Additionally, access to modeling tools to extract quantitative structural information from the optical properties of the gold-island film is of great interest. A simple EMA model, like the BM one for example, must be complemented with a characterization technique such as XPS or XRR to obtain physical meaning of the effective thickness as previously discussed. However, these models don't take into account the size distribution necessary to realistically characterize the nanostructure.

Starting from the Clausius-Mossotti relation:

$$\frac{\varepsilon_{eff} - \varepsilon_m}{\varepsilon_{eff} + 2\varepsilon_m} = \frac{f}{\bar{R}^3}\alpha(\bar{R}) \tag{5.1}$$

one can express the size distribution by scaling the polarizability associated with varying island size [143]:

$$\frac{\varepsilon_{eff} - \varepsilon_m}{\varepsilon_{eff} + 2\varepsilon_m} = \frac{f}{\bar{R}^3}\int_{R_{min}}^{R_{max}} P(R)\alpha(R)dR \tag{5.2}$$

where R_{min} and R_{max} are the lower and upper bounds of the size distribution $P(R)$ of the nanoparticles. In Battie *et al.*'s work, the polarizability is that of a spherical particle. The model can be further improved by adding a shape distribution, *i.e.* extending to the case of an ellipsoidal particle with varying a/b ratio with a and b being the two radii of the ellipsoid axes [144].

In general, sputtered gold islands on a surface have the shape of truncated islands at the low effective thickness and the used EMA models cannot account for that. The BM model fit is good but no physical parameter could be extracted since the fit parameters are not related to the NPs size and shape contrarily to the MG model. Lazzari *et al.* were able to integrate Bedeaux's work [145] into a software called *GranFilm* [146] and obtained good agreement with experimental data regarding the size and particle inter-distance. However, the polarizability of hemispheroids is much more complex to compute due to the loss of symmetry for which the analytical solution is tedious to obtain.

In summary, future work should focus on integrating the size distribution into the model of Bedeaux and coworkers using the Eq. 5.2 which would improve its accuracy.

CHAPTER 6 GENERAL DISCUSSION, CONCLUSIONS AND PERSPECTIVE

6.1 Foreword

The general objective of this master's thesis was to contribute to the advancement of plasmonic-based absorbing filters manufacturing via PVD methods. In this chapter, a discussion summarizing the results and what can be concluded from the accomplished work regarding the initial objectives for the project are exposed. Then, short recommendations follow concerning further development of plasmonic coatings at the FCSEL for ophthalmic lens applications.

6.2 General discussion and conclusions

The work done in this study of selectively absorbing metal-island films was principally motivated to explore the available color space of gold deposited with different seed and capping layers. The mechanical integrity of the island film was found to be greater for a lower filling factor of the gold on the substrate. Furthermore, it was concluded that a maximal performance in coloration could also be obtained from a small coverage gold-island film, *i.e.* low effective thickness. Indeed, it was found that the best strategy is to start from a selective absorbing peak at the highest frequency possible and, with the addition of a capping layer, for example, tinker the peak position. Moreover, past about 2.5 nm, the gold film at room temperature only exhibits a broad absorption peak which leaves little room for adjustment.

Additionally, investigation of the impact of ion-bombardment on island films was done. This approach has shown a promising alternative to the substrate heating in order to improve the color parameters of a plasmonic composite. Additionally, *in situ* transmittance allowed to obtain the complete color space associated with the growth of a sputtered gold film. Colors were associated with microstructures and the positive impact of ion bombardment on coloration assessed. The optical monitoring method presented here allows one to optimize an absorbing filter. Furthermore, it can accelerate the development of new coating since a single experiment is necessary to explore the accessible color space for a given configuration.

In conjunction with the work done on the color properties of gold-island films, it was demonstrated that *in situ* monitoring can provide important information on the growth dynamics throughout the deposition. Here, a simple analysis of the time derivative surface reflectance was enough to reveal the transitions of growth regime which are not apparent otherwise. The method applicability was confirmed by depositing the thin gold film at higher temperatures.

A similar behavior was observed for deposition at 100° C, albeit the regime transitions were shifted toward greater effective thicknesses. However, increasing the deposition temperature to 200° C did not reveal the characteristic signature associated with a transition from an isolated island to a continuous film which would require more resources to investigate properly. A comparison of the experimental data with EMA models has highlighted the limited applicability of these models for sputtered gold-island films. From this study, understanding the growth kinetics from just reflectance measurement is possible with readily available equipment. Finally, the limitations and potential improvement to better the optical monitoring method were discussed.

In conclusion, a monitoring method was successfully developed and paved the way in our understanding of the background physics involved in the optical response of complex nanostructures. Characteristic changes of trend in the reflectivity was associated with resonating structure found at specific growth stages. To provide more robustness to the analysis, a better optical model needs to be employed to extract valid morphological parameters such as the size and coverage of the islands to support the observations. Experiments on various surfaces, at different deposition rates and with other plasmonic material can be conducted in the same fashion. These choices of material will have an impact on the color parameters and further extend our knowledge on the wealth of possible colors using plasmonic composites.

6.3 Perspectives and outlook

The idea of using silver instead of gold has been discussed throughout this work. An expertise has been developed to protect silver layers from oxidization in the FCSEL [147] and could be applied to the development of colored filters for ophthalmic lenses. Furthermore, the low refractive index of metal-island film allows one to realize ideal AR filters which are thinner than conventional quarter-wave design due to the absorption inducing light dephasing [148, 149]. The combination of absorber with plasmonic layer is of great interest for plasmonic-based color generation. Moreover, it was found that the properties of a broadband absorber could be greatly enhanced with the use of metal-island films [2, 150]. Lastly, the color generation quality of plasmonic material could be integrated in security devices for anti-counterfeiting [151].

REFERENCES

[1] Anders Kristensen, Joel KW Yang, Sergey I Bozhevolnyi, Stephan Link, Peter Nordlander, Naomi J Halas, and N Asger Mortensen. Plasmonic colour generation. *Nature Reviews Materials*, 2(1):16088, 2017.

[2] Mady Elbahri, Moheb Abdelaziz, Shahin Homaeigohar, Abdou Elsharawy, Mehdi Keshavarz Hedayati, Christian Röder, Mamdouh El Haj Assad, and Ramzy Abdelaziz. Plasmonic metaparticles on a blackbody create vivid reflective colors for naked-eye environmental and clinical biodetection. *Advanced Materials*, 30(4):1704442, 2018.

[3] Pulickel M Ajayan, Linda S Schadler, and Paul V Braun. *Nanocomposite science and technology*. John Wiley & Sons, 2006.

[4] T. Pradell, J. Molera, A. D. Smith, and M. S. Tite. Early Islamic lustre from Egypt, Syria and Iran (10th to 13th century AD). *J. Archaeolog. Sci.*, 35(9):2649–2662, 2008.

[5] Gustav Mie. Beitrage zur optik truber medien, speziell kolloidaler metallosungen. *Annalen der physik*, 330(3):377–445, 1908.

[6] S. Kinoshita, S. Yoshioka, and J. Miyazaki. Physics of structural colors. *Rep. Prog. Phys.*, 71(7):076401, 2008.

[7] Claire Dupas, Philippe Houdy, and Marcel Lahmani. *Nanoscience*. Springer, 2007.

[8] U. Kreibig, G. Bour, A. Hilger, and M. Gartz. Optical Properties of Cluster–Matter: Influences of Interfaces. *Phys. Status solidi A*, 175(1):351–366, 1999.

[9] Lukas Novotny and Bert Hecht. *Principles of nano-optics*. Cambridge university press, 2012.

[10] Luciano De Sio. *Active plasmonic nanomaterials*. CRC Press, 2015.

[11] Palash Bharadwaj, Bradley Deutsch, and Lukas Novotny. Optical Antennas. *Adv. Opt. Photonics*, 1(3):438–483, 2009.

[12] Paul L. Stiles, Jon A. Dieringer, Nilam C. Shah, and Richard P. Van Duyne. Surface-Enhanced Raman Spectroscopy. *Annu. Rev. Anal. Chem.*, 1(1):601–626, 2008.

[13] Hongxing Xu, Erik J Bjerneld, Mikael Käll, and Lars Börjesson. Spectroscopy of single hemoglobin molecules by surface enhanced raman scattering. *Physical review letters*, 83(21):4357, 1999.

[14] Alexandre Dmitriev. *Nanoplasmonic Sensors*. Springer, New York, NY, 2012.

[15] S Sajed, F Arefi, M Kolahdouz, and MA Sadeghi. Improving sensitivity of mercury detection using learning based smartphone colorimetry. *Sensors and Actuators B: Chemical*, page 126942, 2019.

[16] RM Tripathi, Sun Hee Park, Gahyeon Kim, Do-Hwi Kim, Dohee Ahn, Yeong Mok Kim, Se Jeong Kwon, Sun-Young Yoon, Hyo Jin Kang, and Sang J Chung. Metal-induced redshift of optical spectra of gold nanoparticles: An instant, sensitive, and selective visual detection of lead ions. *International Biodeterioration & Biodegradation*, 144:104740, 2019.

[17] S Pillai, KR Catchpole, T Trupke, and MA Green. Surface plasmon enhanced silicon solar cells. *Journal of applied physics*, 101(9):093105, 2007.

[18] Daijiro Tsukamoto, Yasuhiro Shiraishi, Yoshitsune Sugano, Satoshi Ichikawa, Shunsuke Tanaka, and Takayuki Hirai. Gold nanoparticles located at the interface of anatase/rutile tio2 particles as active plasmonic photocatalysts for aerobic oxidation. *Journal of the American Chemical Society*, 134(14):6309–6315, 2012.

[19] Matthew B. Boucher, Simone Goergen, Nan Yi, and Maria Flytzani-Stephanopoulos. 'Shape effects' in metal oxide supported nanoscale gold catalysts. *PCCP*, 13(7):2517–2527, 2011.

[20] Andrea Marin-Lopez, Ana Sousa-Castillo, Enrique Carbo-Argibay, Francisco Otero-Espinar, Ramon A. Alvarez-Puebla, Moises Perez-Lorenzo, and Miguel A. Correa-Duarte. Laser-protective soft contact lenses: Keeping an eye on the eye through plasmonics. *Appl. Mater. Today*, 15:1–5, 2019.

[21] Dominique Meslin. *Materials & Treatment*. Essilor Academy Europe, 2010.

[22] Materials, 1997.

[23] AW Birley. *Handbook of Plastics and Elastomers*. British Polymer Journal, 1976.

[24] Carl V. Thompson. Solid-State Dewetting of Thin Films. *Annu. Rev. Mater. Res.*, 42(1):399–434, 2012.

[25] N. Venugopal and Anirban Mitra. Influence of temperature dependent morphology on localized surface plasmon resonance in ultra-thin silver island films. *Applied Surface Science*, 285:357–372, 2013.

[26] Marcel Di Vece, Neil P. Young, Ziyou Li, Yu Chen, and Richard E. Palmer. Co-deposition of Atomic Clusters of Different Size and Composition. *Small*, 2(11):1270–1272, 2006.

[27] Massimo F. Bertino, Zhong-Ming Sun, Rui Zhang, and Lai-Sheng Wang. Facile Syntheses of Monodisperse Ultrasmall Au Clusters. *J. Phys. Chem. B*, 110(43):21416–21418, 2006.

[28] Rajesh Sardar, Alison M. Funston, Paul Mulvaney, and Royce W. Murray. Gold Nanoparticles: Past, Present, and Future. *Langmuir*, 25(24):13840–13851, 2009.

[29] Jorg Polte, Martin Herder, Robert Erler, Simone Rolf, Anna Fischer, Christian Wurth, Andreas F. Thunemann, Ralph Kraehnert, and Franziska Emmerling. Mechanistic insights into seeded growth processes of gold nanoparticles. *Nanoscale*, 2(11):2463–2469, 2010.

[30] Zhongyang Li, Serkan Butun, and Koray Aydin. Touching Gold Nanoparticle Chain Based Plasmonic Antenna Arrays and Optical Metamaterials. *ACS Photonics*, 1(3):228–234, 2014.

[31] Franz Faupel, Vladimir Zaporojtchenko, Thomas Strunskus, and Mady Elbahri. Metal-Polymer Nanocomposites for Functional Applications. *Adv. Eng. Mater.*, 12(12):1177–1190, 2010.

[32] Matthias Schwartzkopf, Adeline Buffet, Volker Körstgens, Ezzeldin Metwalli, Kai Schlage, Gunthard Benecke, Jan Perlich, Monika Rawolle, André Rothkirch, Berit Heidmann, Gerd Herzog, Peter Müller-Buschbaum, Ralf Röhlsberger, Rainer Gehrke, Norbert Stribeck, and Stephan V. Roth. From atoms to layers: in situ gold cluster growth kinetics during sputter deposition. *Nanoscale*, 5(11):5053, 2013.

[33] C. Kratz, T. W. H. Oates, and K. Hinrichs. Optimization and quantification of surface enhanced infrared absorption using gradient gold island films. *Thin Solid Films*, 617:33–37, 2016.

[34] Harry I. Zeltzer and Harry I. Zeltzer. Method of improving color discrimination, Nov 1971.

[35] Barry AJ Clark. Color in sunglass lenses. *Optometry and Vision Science*, 46(11):825–840, 1969.

[36] Michael Faraday. The bakerian lecture: Experimental relations of gold (and other metals) to light. *The Royal Society Publishing*, 147:147–181, 1857.

[37] W. R. Grove. Vii. on the electro-chemical polarity of gases. *Philosophical Transactions of the Royal Society of London*, 142:87–101, 1852.

[38] Milton Ohring. *The Materials Science of Thin Films*. Academic Press, 1991.

[39] John L Vossen, Werner Kern, and Walter Kern. *Thin film processes II*, volume 2. Academic Press, 1991.

[40] Kasturi Lal Chopra. Growth of sputtered vs evaporated metal films. *Journal of Applied Physics*, 37(9):3405–3410, 1966.

[41] S. S. Lau, R. H. Mills, and D. G. Muth. Temperature rise during film deposition by rf and dc sputtering. *Journal of Vacuum Science and Technology*, 9(4):1196–1202, 1972.

[42] J.T. Mayer, R.F. Lin, and E. Garfunkel. Surface and bulk diffusion of adsorbed nickel on ultrathin thermally grown silicon dioxide. *Surface Science*, 265:102–110, 1992.

[43] K. Oura, V. G. Lifshits, Alexander Saranin, A. V. Zotov, and M. Katayama. *Surface Science: An Introduction*. Springer-Verlag Berlin Heidelberg, 2003.

[44] Campbell Charles T. Ultrathin metal films and particles on oxide surfaces: structural, electronic and chemisorptive properties. *Surface Science Reports*, 27:1–111, 1997.

[45] E. Bauer and Jan H. van der Merwe. Structure and growth of crystalline superlattices: From monolayer to super lattice. *Physical Review B*, 33(6):3657–3671, 1986.

[46] JA Venables and GDT Spiller. Nucleation and growth of thin films. In *Surface Mobilities on Solid Materials*, pages 341–404. Springer, 1983.

[47] JA Venables. Rate equation approaches to thin film nucleation kinetics. *Philosophical Magazine*, 27(3):697–738, 1973.

[48] K Reichelt. Nucleation and growth of thin films. *Vacuum*, 38(12):1083 – 1099, 1988.

[49] K Reichelt. The determination of the integrated condensation coefficient of gold on nacl cleavage faces by rutherford ion backscattering. *Surface Science*, 93(1):159 – 174, 1980.

[50] Charles T. Campbell and A. Ludviksson. Model for the growth and reactivity of metal films on oxide surfaces: Cu on zno(0001)-o. *Journal of Vacuum Science & Technology A*, 12(12):1825–1831, 1994.

[51] S.C. Parker, A.W. Grant, V.A. Bondzie, and C.T. Campbell. Island growth kinetics during the vapor deposition of gold onto tio2(110). *Surface Science*, 441(1):10–20, 1999.

[52] K. H. Ernst, A. Ludviksson, R. Zhang, J. Yoshihara, and C. T. Campbell. Growth model for metal films on oxide surfaces: Cu on ZnO(0001)-O. *Phys. Rev. B*, 47(20):13782–13796, 1993.

[53] Karina Morgenstern, Erik Laegsgaard, and Flemming Besenbacher. Brownian Motion of 2D Vacancy Islands by Adatom Terrace Diffusion. *Phys. Rev. Lett.*, 86(25):5739–5742, 2001.

[54] King C. Lai, Yong Han, Peter Spurgeon, Wenyu Huang, Patricia A. Thiel, Da-Jiang Liu, and James W. Evans. Reshaping, Intermixing, and Coarsening for Metallic Nanocrystals: Nonequilibrium Statistical Mechanical and Coarse-Grained Modeling. *Chem. Rev.*, 119(11):6670–6768, 2019.

[55] Hans Lüth. *Solid surfaces, interfaces and thin films*, volume 4. Springer, 2001.

[56] P. M Duxbury, M Dubson, X Yu, and G Jeffers. Substrate inhomogeneity and the growth morphology of thin films. *Europhysics Letters (EPL)*, 26(8):601–606, 1994.

[57] G. Jeffers, M. A. Dubson, and P. M. Duxbury. Island-to-percolation transition during growth of metal films. *Journal of Applied Physics*, 75(10):5016–5020, 1994.

[58] H Sato, S Shinozaki, and LJ Cicotte. Direct observation of epitaxy on mgo. *Journal of Vacuum Science and Technology*, 6(1):62–64, 1969.

[59] X Yu, PM Duxbury, G Jeffers, and MA Dubson. Coalescence and percolation in thin metal films. *Physical Review B*, 44(23):13163, 1991.

[60] Jong Min Yuk, Myoungho Jeong, Sang Yun Kim, Hyeon Kook Seo, Jihyun Kim, and Jeong Yong Lee. In situ atomic imaging of coalescence of Au nanoparticles on graphene: rotation and grain boundary migration. *Chem. Commun.*, 49(98):11479–11481, 2013.

[61] Fereydoon Family and Paul Meakin. Scaling of the droplet-size distribution in vapor-deposited thin films. *Physical review letters*, 61(4):428, 1988.

[62] M Jose-Yacaman, C Gutierrez-Wing, M Miki, D-Q Yang, KN Piyakis, and E Sacher. Surface diffusion and coalescence of mobile metal nanoparticles. *The Journal of Physical Chemistry B*, 109(19):9703–9711, 2005.

[63] Kari EJ Lehtinen and Michael R Zachariah. Energy accumulation in nanoparticle collision and coalescence processes. *Journal of Aerosol Science*, 33(2):357–368, 2002.

[64] D-Q Yang and E Sacher. Ar+-induced surface defects on hopg and their effect on the nucleation, coalescence and growth of evaporated copper. *Surface science*, 516(1-2):43–55, 2002.

[65] Md. Mijanur Rahman, Nampei Hattori, Yuta Nakagawa, Xu Lin, Shiki Yagai, Masatoshi Sakai, Kazuhiro Kudo, and Kazunuki Yamamoto. Preparation and characterization of silver nanoparticles on localized surface plasmon-enhanced optical absorption. *Jpn. J. Appl. Phys.*, 53(11S):11RE01, 2014.

[66] Hongtao Sun, Mingpeng Yu, Gongkai Wang, Xiang Sun, and Jie Lian. Temperature-dependent morphology evolution and surface plasmon absorption of ultrathin gold island films. *The Journal of Physical Chemistry C*, 116(16):9000–9008, 2012.

[67] Xilian Sun, Ruijin Hong, Haihong Hou, Zhengxiu Fan, and Jianda Shao. Thickness dependence of structure and optical properties of silver films deposited by magnetron sputtering. *Thin Solid Films*, 515(17):6962–6966, 2007.

[68] M. Asoro, J. Damiano, and PJ Ferreira. Size Effects on the Melting Temperature of Silver Nanoparticles: In-Situ TEM Observations. *Microsc. Microanal.*, 15(S2):706–707, 2009.

[69] A. P. Chernyshev. Effect of nanoparticle size on the onset temperature of surface melting. *Mater. Lett.*, 63(17):1525–1527, Jul 2009.

[70] Martin Loncaric, Jordi Sancho-Parramon, M. Pavlovic, H. Zorc, P. Dubček, A. Turkovic, S. Bernstorff, G. Jakopic, and A. Haase. Optical and structural characterization of silver islands films on glass substrates. *Vacuum*, 84(1):188–192, 2009.

[71] Martin Loncaric, Jordi Sancho-Parramon, and Hrvoje Zorc. Optical properties of gold island films—a spectroscopic ellipsometry study. *Thin Solid Films*, 519(9):2946–2950, 2011.

[72] Matthias Schwartzkopf, Gonzalo Santoro, Calvin J. Brett, André Rothkirch, Oleksandr Polonskyi, Alexander Hinz, Ezzeldin Metwalli, Yuan Yao, Thomas Strunskus, Franz

Faupel, Peter Müller-Buschbaum, and Stephan V. Roth. Real-time monitoring of morphology and optical properties during sputter deposition for tailoring metal–polymer interfaces. *ACS Applied Materials & Interfaces*, 7(24):13547–13556, 2015.

[73] Matthias Schwartzkopf, Alexander Hinz, Oleksandr Polonskyi, Thomas Strunskus, Franziska C. Löhrer, Volker Körstgens, Peter Müller-Buschbaum, Franz Faupel, and Stephan V. Roth. Role of sputter deposition rate in tailoring nanogranular gold structures on polymer surfaces. *Applied Materials & Interfaces*, 9(6):5629–5636, 2017.

[74] S. J. Henley, J. D. Carey, and S. R. P. Silva. Pulsed-laser-induced nanoscale island formation in thin metal-on-oxide films. *Phys. Rev. B*, 72:195408, 2005.

[75] James S. Im, Paul C. Van Der Wilt, and Ui-Jin Chung. Flash light annealing for thin films, 2009.

[76] Z. Paszti, G. Peto, Z. E. Horvath, O. Geszti, A. Karacs, and L. Guczi. Nanoparticle formation induced by low-energy ion bombardment of island thin films. *Appl. Phys. A*, 76(4):577–587, 2003.

[77] P. J. Martin. Ion-based methods for optical thin film deposition. *Journal of Materials Science*, 21(1):1–25, 1986.

[78] Maxim A. Makeev and Albert-László Barabási. Ion-induced effective surface diffusion in ion sputtering. *Applied Physics Letters*, 71(19):2800–2802, 1997.

[79] SM Rossnagel and JJ Cuomo. Ion beam bombardment effects during films deposition. *Vacuum*, 38(2):73 – 81, 1988.

[80] Miko Marinov. Effect of ion bombardment on the initial stages of thin film growth. *Thin Solid Films*, 46(3):267–274, 1977.

[81] Zs. Baji, A. Szanyo, Gy. Molnár, A. L. Toth, G. Pető, K. Frey, E. Kotai, and G. Kaptay. Formation of nanoparticles by ion beam irradiation of thin films. *Journal of Nanoscience and Nanotechnology*, 12(6):5009–5015, 2012.

[82] H. G. Scott. Sputtering of gold by low energy inert gas ions. *Journal of Applied Physics*, 33, 2011, 1962.

[83] R.P. Netterfield and P.J. Martin. Nucleation and growth studies of gold films prepared by evaporation and ion-assisted deposition. *Applied Surface Science*, 25(3):265 – 278, 1986.

[84] Bahaa E. A. Saleh and Malvin Carl Teich. *Fundamentals of Photonics*. Wiley, 2007.

[85] I. F. Almog, M. S. Bradley, and V. Bulovic. The Lorentz Oscillator and its Applications, 2011.

[86] J. P. Marton and J. R. Lemon. Optical properties of aggregated metal systems. i. theory. *Phys. Rev. B*, 4:271–280, 1971.

[87] Schneider John B. Understanding the finite-difference time-domain method, 2010.

[88] Anna Kossoy, Virginia Merk, Denis Simakov, Kristjan Leosson, Stephane Kena-Cohen, and Stefan A. Maier. Optical and Structural Properties of Ultra-thin Gold Films. *Adv. Opt. Mater.*, 3(1):71–77, 2015.

[89] J. C. Maxwell-Garnett and Larmor Joseph. XII. Colours in metal glasses and in metallic films. *Philosophical Transactions of the Royal Society of London. Series A*, 203(359-371):385–420, 1904.

[90] Scott B Jones and Shmulik P Friedman. Particle shape effects on the effective permittivity of anisotropic or isotropic media consisting of aligned or randomly oriented ellipsoidal particles. *Water Resources Research*, 36(10):2821–2833, 2000.

[91] D. A. G. Bruggeman. Berechnung verschiedener physikalischer konstanten von heterogenen substanzen. i. dielektrizitätskonstanten und leitfähigkeiten der mischkörper aus isotropen substanzen. *Annalen der Physik*, 416(7):636–664, 1935.

[92] C. G. Granqvist and O. Hunderi. Optical properties of ultrafine gold particles. *Phys. Rev. B*, 16:3513–3534, Oct 1977.

[93] G. Xu, M. Tazawa, P. Jin, S. Nakao, and K. Yoshimura. Wavelength tuning of surface plasmon resonance using dielectric layers on silver island films. *Applied Physics Letters*, 82(22):3811–3813, 2003.

[94] G. Xu, M. Tazawa, P. Jin, and S. Nakao. Surface plasmon resonance of sputtered ag films: substrate and mass thickness dependence. *Applied Physics A*, 80(7):1535–1540, 2005.

[95] SK Mandal, RK Roy, and AK Pal. Effect of particle shape distribution on the surface plasmon resonance of ag–sio2 nanocomposite thin films. *Journal of Physics D: Applied Physics*, 36(3):261, 2003.

[96] J. Vieaud, O. Merchiers, M. Rajaoarivelo, M. Warenghem, Y. Borensztein, V. Ponsinet, and A. Aradian. Effective medium description of plasmonic couplings in disordered polymer and gold nanoparticle composites. *Thin Solid Films*, 603:452–464, 2016.

[97] Rufus H Ritchie. Plasma losses by fast electrons in thin films. *Physical review*, 106(5):874, 1957.

[98] Stefan Alexander Maier. *Plasmonics: fundamentals and applications*. Springer Science & Business Media, 2007.

[99] S. Enoch and N. Bonod. *Plasmonics: From Basics to Advanced Topics*. Springer Series in Optical Sciences. Springer Berlin Heidelberg, 2012.

[100] Palash Bharadwaj, Bradley Deutsch, and Lukas Novotny. Optical antennas. *Adv. Opt. Photon.*, 1(3):438–483, 2009.

[101] Bohren Craig F. and Huffman Donald R. *Absorption and Scattering of Light by Small Particles*. John Wiley & Sons, 1998.

[102] Jean-Michel Lamarre. *Propriétés optiques linéaires et non-linéaires de nanocomposites métal-diélectrique anisotropes*. PhD thesis, Polytechnique Montréal, 2008.

[103] RK Roy, SK Mandal, and AK Pal. Effect of interfacial alloying on the surface plasmon resonance of nanocrystalline au-ag multilayer thin films. *The European Physical Journal B-Condensed Matter and Complex Systems*, 33(1):109–114, 2003.

[104] P.R. West, S. Ishii, G.V. Naik, N.K. Emani, V.M. Shalaev, and A. Boltasseva. Searching for better plasmonic materials. *Laser & Photonics Reviews*, 4(6):795–808, 2010.

[105] Panos Patsalas, Nikolaos Kalfagiannis, and Spyros Kassavetis. Optical Properties and Plasmonic Performance of Titanium Nitride. *Materials*, 8(6):3128–3154, 2015.

[106] A Reinholdt, R Pecenka, A Pinchuk, S Runte, AL Stepanov, Th E Weirich, and U Kreibig. Structural, compositional, optical and colorimetric characterization of tin-nanoparticles. *The European Physical Journal D-Atomic, Molecular, Optical and Plasma Physics*, 31(1):69–76, 2004.

[107] P. R. West, S. Ishii, G. V. Naik, N. K. Emani, V. M. Shalaev, and A. Boltasseva. Searching for better plasmonic materials. *Laser Photonics Rev.*, 4(6):795–808, 2010.

[108] Li Wei and Valentine Jason G. Harvesting the loss: surface plasmon-based hot electron photodetection. *Nanophotonics*, 6:177–191, 2017.

[109] OL Muskens, N Del Fatti, F Vallée, JR Huntzinger, P Billaud, and M Broyer. Single metal nanoparticle absorption spectroscopy and optical characterization. *Applied Physics Letters*, 88(6):063109, 2006.

[110] Vincent Juvé, M Fernanda Cardinal, Anna Lombardi, Aurelien Crut, Paolo Maioli, Jorge Perez-Juste, Luis M Liz-Marzan, Natalia Del Fatti, and Fabrice Vallee. Size-dependent surface plasmon resonance broadening in nonspherical nanoparticles: single gold nanorods. *Nano letters*, 13(5):2234–2240, 2013.

[111] Pavel Ginzburg, Nikolai Berkovitch, Amir Nevet, Itay Shor, and Meir Orenstein. Resonances On-Demand for Plasmonic Nano-Particles. *Nano Lett.*, 11(6):2329–2333, 2011.

[112] Steven J. Barrow, Alison M. Funston, Daniel E. Gómez, Tim J. Davis, and Paul Mulvaney. Surface Plasmon Resonances in Strongly Coupled Gold Nanosphere Chains from Monomer to Hexamer. *Nano Lett.*, 11(10):4180–4187, 2011.

[113] Tolga Atay, Jung-Hoon Song, and Arto V. Nurmikko. Strongly Interacting Plasmon Nanoparticle Pairs: From Dipole-Dipole Interaction to Conductively Coupled Regime. *Nano Lett.*, 4(9):1627–1631, 2004.

[114] G. Sun and J. B. Khurgin. Comparative study of field enhancement between isolated and coupled metal nanoparticles: An analytical approach. *Appl. Phys. Lett.*, 97(26):263110, 2010.

[115] H Baida, Pierre Billaud, Marhaba, et al. Quantitative determination of the size dependence of surface plasmon resonance damping in single ag-sio2 nanoparticles. *Nano letters*, 9(10):3463–3469, 2009.

[116] Adam D McFarland and Richard P Van Duyne. Single silver nanoparticles as real-time optical sensors with zeptomole sensitivity. *Nano letters*, 3(8):1057–1062, 2003.

[117] Uwe Kreibig, M. Quinten, and D. Schoenauer. Optical Properties of Many-Particle Systems. *Phys. Scr.*, T13(T13):84–92, 1986.

[118] G. B. Smith and A. A. Earp. Metal-in-metal localized surface plasmon resonance. *Nanotechnology*, 21(1):015203, 2009.

[119] Martin Hovel, Bruno Gompf, and Martin Dressel. Dielectric properties of ultrathin metal films around the percolation threshold. *Phys. Rev. B*, 81(3):035402, 2010.

[120] Roberto Sangiorgi, Maria L Muolo, Dominique Chatain, and Nicolas Eustathopoulos. Wettability and work of adhesion of nonreactive liquid metals on silica. *Journal of the American Ceramic Society*, 71(9):742–748, 1988.

[121] A. Achour, M. Islam, S. Solaymani, S. Vizireanu, Khalid Saeed, and G. Dinescu. Influence of plasma functionalization treatment and gold nanoparticles on surface chemistry and wettability of reactive-sputtered TiO2 thin films. *Appl. Surf. Sci.*, 458:678–685, Nov 2018.

[122] D Chatain, I Rivollet, and N Eustathopoulos. Adhésion thermodynamique dans les systèmes non-réactifs métal liquide-alumine. *Journal de chimie physique*, 83:561–567, 1986.

[123] Hiroyuki Fujiwara. *Spectroscopic Ellipsometry: Principles and Applications*. 2007.

[124] Roy S. Berns. *Billmeyer and Saltzman's Principles of Color Technology*. John Wiley & Sons Inc., 4 edition, 2019.

[125] Bruce Lindbloom. Useful color equations, 2001.

[126] J.D.E. McIntyre and D.E. Aspnes. Differential reflection spectroscopy of very thin surface films. *Surface Science*, 24(2):417–434, 1971.

[127] Florin Abelès. Recherches sur la propagation des ondes électromagnétiques sinusoïdales dans les milieux stratifiés-application aux couches minces. In *Annales de physique*, volume 12, pages 596–640. EDP Sciences, 1950.

[128] Stéphane Larouche and Ludvik Martinu. Openfilters: open-source software for the design, optimization, and synthesis of optical filters. *Applied Optics*, 47(13):C219, 2008.

[129] Peter J Goodhew and John Humphreys. *Electron microscopy and analysis*. CRC Press, 2000.

[130] R. F. Herzog, J. S. Greeneich, T. E. Everhart, and T. Van Duzer. Computer-controlled resist exposure in the scanning electron microscope. *IEEE Trans. Electron Devices*, 19(5):635–641, 1972.

[131] G. Bradski. The OpenCV Library. *Dr. Dobb's Journal of Software Tools*, 2000.

[132] G. Xu, M. Tazawa, P. Jin, and S. Nakao. Surface plasmon resonance of sputtered Ag films: substrate and mass thickness dependence. *Appl. Phys. A*, 80(7):1535–1540, 2005.

[133] Dave Snow. Sputtering Yield Rates. [Online; accessed 26. Oct. 2019].

[134] Remi Boidin, Tomas Halenkovic, Virginie Nazabal, Ludvik Benes, and Petr Nemec. Pulsed laser deposited alumina thin films. *Ceram. Int.*, 42(1, Part B):1177–1182, 2016.

[135] L. Cattin, S. Tougaard, N. Stephant, S. Morsli, and J. C. Bernède. On the ultrathin gold film used as buffer layer at the transparent conductive anode/organic electron donor interface. *Gold Bull.*, 44(4):199–205, 2011.

[136] Stephan Link and Mostafa A. El-Sayed. Size and temperature dependence of the plasmon absorption of colloidal gold nanoparticles. *The Journal of Physical Chemistry B*, 103(21):4212–4217, 1999.

[137] B. Gompf, J. Beister, T. Brandt, J. Pflaum, and M. Dressel. Nanometer-thick Au-films as antireflection coating for infrared light. *Opt. Lett.*, 32(11):1578–1580, Jun 2007.

[138] John A. Thornton. Structure-Zone Models Of Thin Films. *Modeling of Optical Thin Films*, 0821:95–105, Feb 1988.

[139] V. Tvarožek, O. Szabó, I. Novotný, S. Kováčová, J. Škriniarová, and P. Šutta. Plasmonic behaviour of sputtered au nanoisland arrays. *Applied Surface Science*, 395:241–247, 2017.

[140] G. Gupta, D. Tanaka, Y. Ito, D. Shibata, M. Shimojo, K. Furuya, K. Mitsui, and K. Kajikawa. Absorption spectroscopy of gold nanoisland films: optical and structural characterization. *Nanotechnology*, 20(2):025703, 2008.

[141] G. Sun, J. B. Khurgin, and C. C. Yang. Impact of high-order surface plasmon modes of metal nanoparticles on enhancement of optical emission. *Appl. Phys. Lett.*, 95(17):171103, 2009.

[142] Soroush Hafezian, Bill Baloukas, and Ludvik Martinu. Percolation threshold determination of sputtered silver films using stokes parameters and in situ conductance measurements. *Applied Optics*, 53(24):5367, 2014.

[143] Y Battie, A Resano-Garcia, N Chaoui, Y Zhang, and A En Naciri. Extended maxwell-garnett-mie formulation applied to size dispersion of metallic nanoparticles embedded in host liquid matrix. *The Journal of chemical physics*, 140(4):044705, 2014.

[144] Gao L and Gu J. Z. Effective dielectric constant of a two-component material with shape distribution. *Journal of Physics D: Applied Physics*, 35(267), 2002.

[145] Dick Bedeaux and Jan Vlieger. Optical properties of surfaces. page 446.

[146] Remi Lazzari and Ingve Simonsen. Granfilm: a software for calculating thin-layer dielectric properties and fresnel coefficients. *Thin Solid Films*, 419(1-2):124–136, 2002.

[147] Hafezian Soroush. *Growth Control and Study of Ultrathin Silver Films for Energy-Saving Coatings*. PhD thesis, Polytechnique Montréal, 2019.

[148] M. Keshavarz Hedayati, S. Fahr, C. Etrich, F. Faupel, C. Rockstuhl, and M. Elbahri. The hybrid concept for realization of an ultra-thin plasmonic metamaterial antireflection coating and plasmonic rainbow. *Nanoscale*, 6(11):6037–6045, 2014.

[149] M. Keshavarz Hedayati, M. Abdelaziz, C. Etrich, S. Homaeigohar, C. Rockstuhl, and M. Elbahri. Broadband Anti-Reflective Coating Based on Plasmonic Nanocomposite. *Materials*, 9(8):636, Aug 2016.

[150] M. Keshavarz Hedayati, M. Javaheri, A. Zillohu, H. El-Khozondar, M. Bawa'aneh, A. Lavrinenko, F. Faupel, and M. Elbahri. Photo-driven super absorber as an active metamaterial with a tunable molecular-plasmonic coupling. *Advanced Optical Materials*, 2(8):705–710, 2014.

[151] Bill Baloukas. Thin film-based optically variable security devices: From passive to active. chapter 3, pages 30–50. 2019.

ANNEXE A A

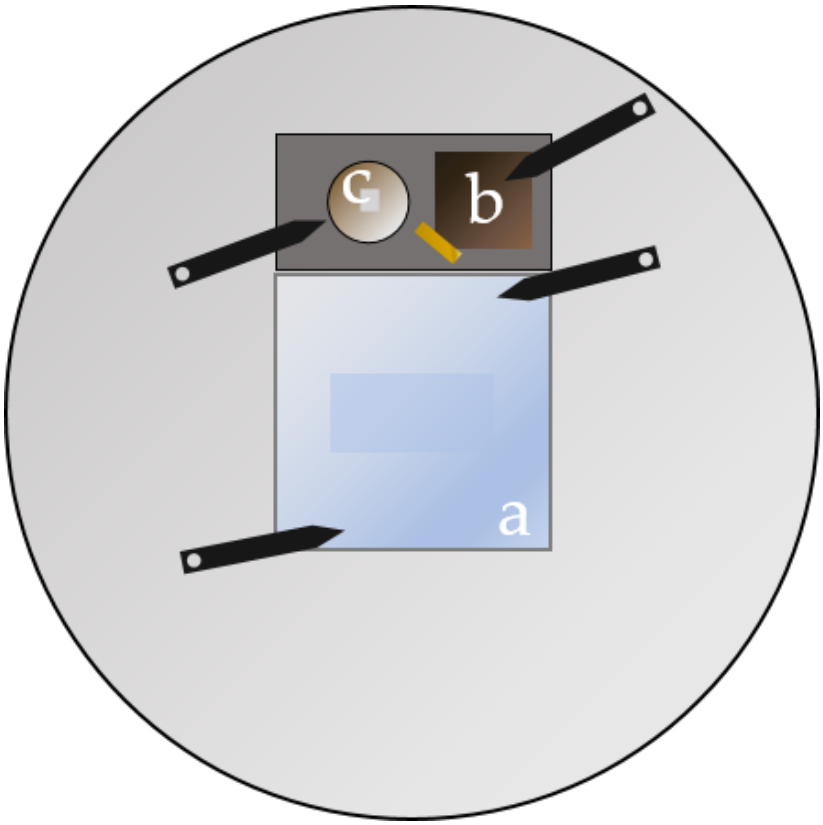

Figure A.1 Schematic showing the experimental arrangement of the different samples used for the experiments: a) B7K glass with a sand blasted back zone on the back to prevent reflection from that side, b) small piece of silicon, and c) TEM membrane. Two arms are used to hold the components and a small piece of teflon tape vacuum compatible is used on one side of the silicon piece so that it sits flush on the small metal piece used to maintain the membrane in place. The membrane is held by a metal piece with a flange and the silicon piece is taped on that piece.